Studies of Atmospheric Fluxes at the prototype iron calorimeter detector

By

Pethuraj S

PHYS01201404022

Bhabha Atomic Research Centre, Mumbai

A Thesis submitted to the
Board of Studies in Physical Sciences
in partial fulfillment of the requirements
for the Degree of

DOCTOR OF PHILOSOPHY

of

Homi Bhabha National Institute

MARCH, 2021

Homi Bhabha National Institute

Recommendations of the Viva Voce Committee

As members of the Viva Voce Board, we certify that we have read the dissertation prepared by Pethuraj S entitled "Studies of Atmospheric Fluxes at the prototype iron calorimeter detector" and recommend that it may be accepted as fulfilling the thesis requirement for the award of the Degree of Doctor of philosophy.

Chair – Prof. Nita Sinha	Nita Sinha	**26.03.2021**
Guide/Convener – Prof. D Indumathi	D. Indumathi	**26.03.2021**
Examiner – Prof. Bipul Bhuyan	Bipul Bhuyan	**26.03.2021**
Member 1 – Prof. G. Majumder	Gobinda Majumder	**26.03.2021**
Member 2 – Prof. Jim Libby		**26.03.2021**
Member 3 – Dr. B. Satyanarayana		**26.03.2021**
Member 4 – Dr. L M Pant		**26.03.2021**

Final approval and acceptance of this thesis is contingent upon the candidate's submission of the final copies of the thesis to HBNI.

I hereby certify that I have read this thesis prepared under my direction and recommend that it may be accepted as fulfilling the thesis requirement.

Date: 26.03.2021

Place: Chennai

D. Indumathi

Prof D Indumathi (Guide)

STATEMENT BY AUTHOR

This dissertation has been submitted in partial fulfillment of requirements for an advanced degree at Homi Bhabha National Institute (HBNI) and is deposited in the Library to be made available to borrowers under rules of the HBNI.

Brief quotations from this dissertation are allowable without special permission, provided that accurate acknowledgement of source is made. Requests for permission for extended quotation from or reproduction of this manuscript in whole or in part may be granted by the Competent Authority of HBNI when in his or her judgement the proposed use of the material is in the interests of scholarship. In all other instances, however, permission must be obtained from the author.

Date: April 11, 2021

Place: Madurai

Pethuraj S

(Enrolment Number PHYS01201404022)

DECLARATION

I, hereby declare that the investigation presented in the thesis has been carried out by me. The work is original and has not been submitted earlier as a whole or in part for a degree/diploma at this or any other Institution/University.

Date: April 11, 2021

Place: Madurai

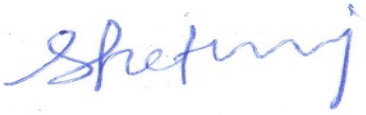

Pethuraj S

(Enrolment Number PHYS01201404022)

List of Publications arising from the thesis

Publications in Refereed Journals

Published

1. Measurement of cosmic muon angular distribution and vertical integrated flux by 2 m × 2 m RPC stack at IICHEP-Madurai. **S. Pethuraj**, V.M. Datar, G. Majumder, N.K. Mondal, K.C. Ravindran, B. Satyanarayana. JCAP09(2017)021, DOI = 10.1088/1475-7516/2017/09/021

2. Measurement of azimuthal dependent muon flux by 2 m × 2 m RPC stack at IICHEP-Madurai. **S. Pethuraj**, V.M. Datar, G. Majumder, N.K. Mondal, K.C. Ravindran, B. Satyanarayana. Experimental Astronomy (2020), https://doi.org/10.1007/s10686-020-09655-y.

Conference Proceedings

Published

1. Measurement of Angular Distribution and Integrated Flux of Cosmic Ray Muons Using 2 m × 2 m RPC Stack at IICHEP Madurai. **S. Pethuraj**, V. M. Datar, S. D. Kalmani, G. Majumder, N. K. Mondal, S. Mondal, P. Nagaraj, Pathaleswar, K. C. Ravindran, M. N. Saraf, B. Satya- narayana, R. R. Shinde, Dipankar Sil, S. H. Thoker, S. S. Upadhya, P. Verma, E. Yuvaraj. XXII DAE High Energy Physics Symposium-Proceedings, Springer Proceedings in Physics, vol 203, pages 845-846.

2. Design and construction of, and physics results from an INO RPC detector stack. Gobinda Majumder, **S. Pethuraj**, B. Satyanarayana, V. Datar,

K.C. Ravindran, Suryanaraya Mondal. PoS ICHEP2018 (2019) 357. DOI: 10.22323/1.340.0357.

Communicated

1. Azimuthal dependence of cosmic muon flux by $2\,\mathrm{m} \times 2\,\mathrm{m}$ RPC Stack at IICHEP-Madurai and comparison with CORSIKA and HONDA flux. **S. Pethuraj**, V. M. Datar, S. D. Kalmani, G. Majumder, N. K. Mondal, S. Mondal, P. Nagaraj, Pathaleswar, K. C. Ravindran, M. N. Saraf, B. Satyanarayana, R. R. Shinde, Dipankar Sil, S. S. Upadhya, P. Verma, E. Yuvaraj. XXIII DAE High Energy Physics Symposium.

Other Publications (Not a part of thesis)

1. Study of particle multiplicity of cosmic ray events using $2\,\mathrm{m} \times 2\,\mathrm{m}$ resistive plate chamber stack at IICHEP-Madurai. S. Mondal, V.M. Datar, G.Majumder, N.K. Mondal, **S. Pethuraj**, B. Satyanarayana. Exp Astron (2020). https://doi.org/10.1007/s10686-020-09685-6.

2. Study of γ-ray background from cosmic muon induced neutrons. H. Krishnamoorthy, G. Gupta, A. Garai, A. Mazumdar, A. Reza, **S. Pethuraj**, V. Nanal*, A. Shrivastava and R.G. Pillay. Eur. Phys. J. A (2019) 55: 136

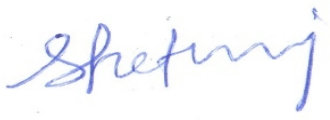

Pethuraj S

(Enrolment Number PHYS01201404022)

Dedicated to,

Prof. G. Rajasekaran

&

Prof. M. V. N. Murthy

ACKNOWLEDGEMENTS

First and foremost, I would like to express my deep and sincere gratitude to my research supervisor Prof. D. Indumathi for the continuous support of my PhD and research, motivation and enthusiasm. Her guidance helped me in all the time of research and writing of this thesis. I could not have imagined having a better advisor and mentor for my PhD study. I especially like to thank Prof. Gobinda Majumder for his role as a mentor and constant guidance during my PhD study and further research work.

I express my gratitude to Prof. N. K. Mondal and Prof. V. M. Datar, the former and present project director of INO, for their constant support and motivation. I am thankful to all the members of INO collaboration and the INO Graduate training program for giving excellent opportunity to work on experimental physics.

I am highly thankful to my doctoral committee members Prof. Nita Sinha, Prof. Jim Libby, Dr B. Satyanarayana and Prof. L. M. Pant for their encouragement, insightful comments and invaluable suggestions.

I thank all colleagues at TIFR, Suresh Kalmani, Piyush Verma, Sharad R Joshi, P Nagraj, Pavan Kumar, Ganesh Ghodke, V V Asgolkar, Ravindra R Shindhe, Mandar N Saraf, Yuvaraj E, Dipankar Sil, H Pathaleswar, Puneet Kaur, Darshana Gonji, Upendra Gokhale and Thoi Thoi for supporting me during my stay at TIFR.

I owe my finest gratitude to my colleagues at Madurai, K C Ravindran, Viswanathan, N Sivaramakrishnan, Rajkumar Bharathi, Umesh, Rajeshwaran, who were helping to get the good quality data for my research. I must thank my friends, Surya, Apoorva, Jim, Hariharan, Dhruv, Harisree, Mamta, Honey and Neha, who shared my joys and sorrows during my PhD.

Finally, I am indebted to my parents for their love, support and encouragement, without their support I could not be in the place where I am now.

Contents

Summary

The proposed 50 kton INO-ICAL experiment is an upcoming underground high energy physics experiment planned to be commissioned at Bodi hills near Theni, India ($9^{\circ}57'N$, $77^{\circ}16'E$) to study various properties of neutrino oscillations using atmospheric neutrinos produced by extensive air shower phenomenon. The resistive plate chamber has been chosen as the active detector element for the proposed INO-ICAL. To study the neutrino oscillation from atmospheric neutrinos, precise knowledge about the neutrino flux at the experimental site is essential. The calculation of neutrino flux is predominantly affected by the uncertainties in the hadronic interaction models. The systematics on neutrino flux calculation due to interaction models can be improved using the measured muon flux near the proposed site. The measured muon flux will be useful in tuning the hadronic models to get a precise neutrino flux at the INO-site. To measure the muon flux near the experimental site, an experimental setup consisting a stack of 12 layers of glass resistive plate chambers each with a size of $\sim$2 m$\times$2 m has been built at IICHEP, Madurai to study the performance and long-term stability of the resistive plate chambers(RPCs) commercially produced in large quantities by the Indian industries as well as its electronics for the front-end and subsequent signal processing. The experiment was performed in two phases, where the readout electronics at both of them are different. In the first phase of the experiment, the electronics chain contains an HMC pre-amplifier, discrete IC-based Analog-Front End board, CPLD based Digital Front-End board, and VME based Back-End system. The phase-2

of the setup contains the ASIC based NINO/ANUSPARSH front-end boards (amplifier and discriminator), FPGA based digital front-end called RPCDAQ, where HPTDC is integrated with the board. The muon data recorded from both the phases are used to study the long-term performance of the RPC detectors. The muon data recorded from the phase-1 is used to study the zenith angle distribution and vertical flux of muons at Madurai (9°56'N, 78°00'E and at an altitude of 160 m above mean sea level). The observed results are compared with measurements from different geomagnetic locations and the comparison is presented in this thesis. Using the phase-2 data, the azimuthal dependence of muon flux at various zenith angles at the experimental site has been presented along with the comparison of Monte Carlo from CORSIKA and HONDA predictions. The east-west asymmetry of the cosmic muons at different zenith angle also estimated and the comparison of these observed values with phenomenological models are discussed in this thesis.

List of Figures

List of Tables

Chapter 1

Introduction

1.1 Neutrino Physics

Recent developments in science and technology have allowed the study of physics which is most exotic and rare in Nature. In the past 100 years, the researches and discoveries in particle physics and nuclear physics became the most vital topics in the field of physics. Many questions about Nature have been unraveled using advanced experiments. But there are many quests about our universe are yet to be answered. Neutrino physics is one of the most interesting fields in physics for the last five decades, which helps to study the energy production mechanism in the sun and other stars. Especially, the non-zero masses of the neutrinos and their oscillation opened up an enormous window in physics beyond the Standard Model of particle physics. Many current and future planned experiments around the world are studying the nature of neutrinos from various sources.

Currently, we know that there are three active neutrino flavours (ν_e, ν_μ and ν_τ) connected to the three neutrino mass states (ν_1, ν_2 and ν_3) via a unitary mixing matrix. The parameters involved in the mixing matrix are three mixing angles (θ_{12}, θ_{23} and θ_{13}) and the CP-violating phase δ_{CP}. The mass squared differences between any two neutrino states are measured from neutrino oscillation experiments. But

still there are few other information about neutrinos that are unknown, especially the sign of $\Delta m^2_{32} = m^2_3 - m^2_2$, the value of δ_{CP} and the correct octant of the θ_{23}-mixing angle.

The proposed magnetised iron calorimeter (ICAL) detector at the India-based Neutrino Observatory (INO) is an underground high energy physics experiment, whose main goal is to determine the sign of Δm^2_{32} using naturally occurring atmospheric neutrinos. These neutrinos are produced when cosmic rays (primarily protons) from outer space interacts with the molecules in the earth's atmosphere, producing pions and kaons, which further decay to muons and muon-type neutrinos. Subsequently, these muons also decay, producing both muon- and electron-type neutrinos.

Hence the measurement or precise knowledge of the cosmic ray spectrum is an important input to determine the atmospheric neutrino fluxes that will be used to study neutrino oscillation parameters at INO-ICAL. This thesis reports on some studies of cosmic ray fluxes in a prototype stack located in Madurai, about 100 km east of the proposed site of INO.

1.1.1 History of Neutrino Physics

The existence of neutrinos in nature was first postulated by W. Pauli to explain the continuous energy spectrum of the β-decay [1, 2]. Assuming β-decay to be a two-body decay, the neutron decays to proton and electron (β particle). Since the recoil energy of the parent nucleus is very small, the maximum energy of the reaction (Q-value) is carried by the electron, which is then expected to be observed as a sharp peak in the energy spectrum of the detected electron. But the observation from β-decay spectrum (shown in Fig. 1.1) from different nuclei, suggests that the detected electrons are not having the Q-value or end-point energy. The spectrum appears to be continuous in nature.

From the spectrum, it can be inferred that to account for the energy-momentum

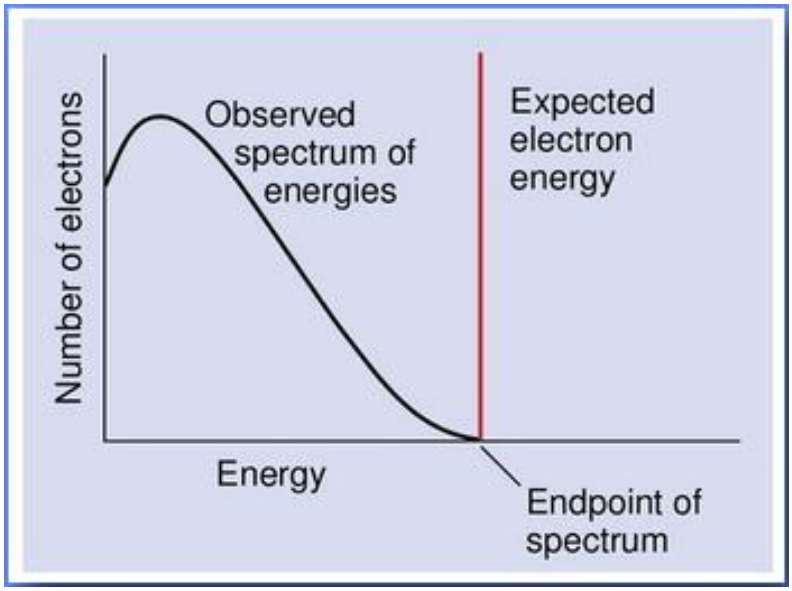

Figure 1.1: Schematic of the observed beta decay spectrum and expected spectrum.

conservation and spin statistics, the two body assumption of β-decay is no more valid. In order to explain this anomaly, the third particle called neutrino was introduced to compensate for the missing energy. Neutrinos are neutral in charge, with a very tiny mass (originally postulated to be massless) and interact via only the weak interaction and that makes it hard to detect them.

The theoretical formalism of the β-decay by considering the existence of neutrino was derived by Enrico Fermi and the formalism matches with experimental data [3–5]. The first experimental detection of the neutrino was done in nuclear reactions (the emission of electron type anti-neutrino from the nuclear decay) using the inverse β-decay process (shown in Eq. 1.1) by Cowan and Reines in 1956 [6, 7]:

$$\overline{\nu}_e + p \rightarrow e^+ + n \ . \tag{1.1}$$

After the discovery of electron type neutrinos, in 1962 another type of neutrino called muon neutrino was detected in the accelerator-based experiment in Brookhaven National Accelerator Laboratory [8]. The ν_μ detected in the experiment is produced from the decay of charged pions to muons and muon type neutrinos. Thirty-six

years later, third generation of neutrino called ν_τ (tau type neutrino) was detected by the Donut collaboration [9]. After the discovery of the ν_τ, the entries in the lepton family of the standard model are now complete.

1.1.2 Neutrinos and the Standard Model of particle physics

The Standard Model (SM) of particle physics was formulated in 1967 by S. Weinberg and A. Salam [10, 11]. SM is currently the most accepted theory in particle physics to describe the elementary particles and the fundamental forces in nature except the gravitational force. The SM corresponds to a direct product of three groups, $\mathrm{SU}(3) \otimes \mathrm{SU}(2) \otimes \mathrm{SU}(1)$, where the group SU(3) represents the colour charge of Quantum Chromodynamics, SU(2) denotes the weak isospin and SU(1) group represents the hypercharge. The $\mathrm{SU}(2) \otimes \mathrm{SU}(1)$, electroweak section in the SM called Glashow-Weinberg-Salam (GWS) model [10–12] or quantum flavour dynamics (QFD). The concept of weak isospin is similar to isospin in strong interactions.

The electroweak section of the standard model predicted the existence of weak neutral currents and the Z-boson [12]. The discovery of neutral current neutrino interaction by the Gargamelle experiment at CERN [13–15] and subsequent confirmation at Fermilab [16] indicated the validity of the Standard Model. As per SM the fundamental building blocks of matter is made up of 12 spin 1/2 fermions (leptons and quarks) as well as their anti-particles. These fermions interact among each other by exchanging spin-1 gauge bosons which are the mediators of the various interactions.

In the SM, the fermions and W/Z bosons acquire mass due to interaction with the Higgs field through the spontaneous symmetry breaking mechanism. The particle associated with Higgs field is called the Higgs boson. The existence of these elementary particles are confirmed by many experiments around the world. The most recent discovery among all others is the discovery of the Higgs boson at the LHC experiment at CERN [17, 18].

Neutrinos are one of the least known particles in the standard model. There are three known types of active flavours of neutrinos and this number is experimentally constrained by the accurate measurement of the invisible decay width of the Z-boson by the LEP at CERN [19–22]. There are two different modes in which neutrinos can interact with matter, (*i*) charged current, where it interacts by exchange of W-boson and (*ii*) neutral current, where Z-boson is the force carrier. Within the Standard Model, all neutrino flavours are massless, the neutrinos (anti-neutrinos) are left-handed (right-handed) particles, and parity and charge-conjugation invariance are maximally violated in the interactions.

1.1.3 Neutrino Sources

The detailed discussion about the various sources of neutrinos and neutrino oscillation is given in Ref. [23]. Currently, we know that there are three types of flavour states and three mass states of neutrinos[1]. The energy of neutrinos from different sources shows a large range of spectrum that varies from 10^{-6} eV to 10^{20} eV. The energy spectrum of the neutrinos from different sources is shown in Fig. 1.2.

1.1.4 Cosmological Sources

Similar to the cosmic microwave background, there is also a cosmological neutrino background. The temperature of these neutrinos is estimated to be 1.95 K. The energy of these neutrinos is extremely low, which makes it hard to detect them with the present day detector technology. Till now, there is no neutrino detector that has such a very low threshold to sense these neutrinos. The number density of cosmological neutrinos is estimated to be $\sim 330/\text{cm}^3$.

[1]The LEP experiment has a strong bound on the number of light (mass less than half the Z boson mass) active neutrino flavours to be three.

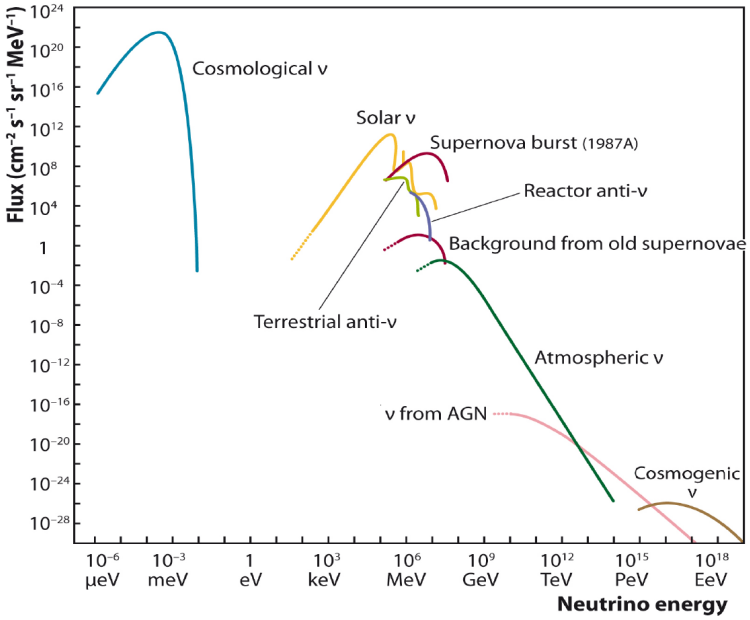

Figure 1.2: Neutrino fluxes from different sources[24].

1.1.5 Solar neutrinos

Other than cosmological, there are many other sources, where the neutrinos are detected successfully using the present-day neutrino detector technology because of the energy range of these neutrinos. The neutrinos produced inside the sun are the major source at the earth. According to the present understanding, the sun and other stars produce energy by nuclear fusion reactions. The major reaction in the sun which is responsible for 98.4 % of the solar energy is from the *pp* chain. The remaining 1.6 % of the solar energy is produced [25] from the CNO cycle. The *pp*-chain and CNO cycle are shown in Figs. 1.3 and 1.4. These solar neutrinos have been detected in Davis's chlorine experiment [26], Super-Kamioka experiment [27–29], SNO [30] and many others.

1.1.6 Atmospheric Neutrinos

The atmospheric neutrinos are created as a product of the decay of the secondaries produced in the interaction of cosmic rays with the atmosphere. The main part of

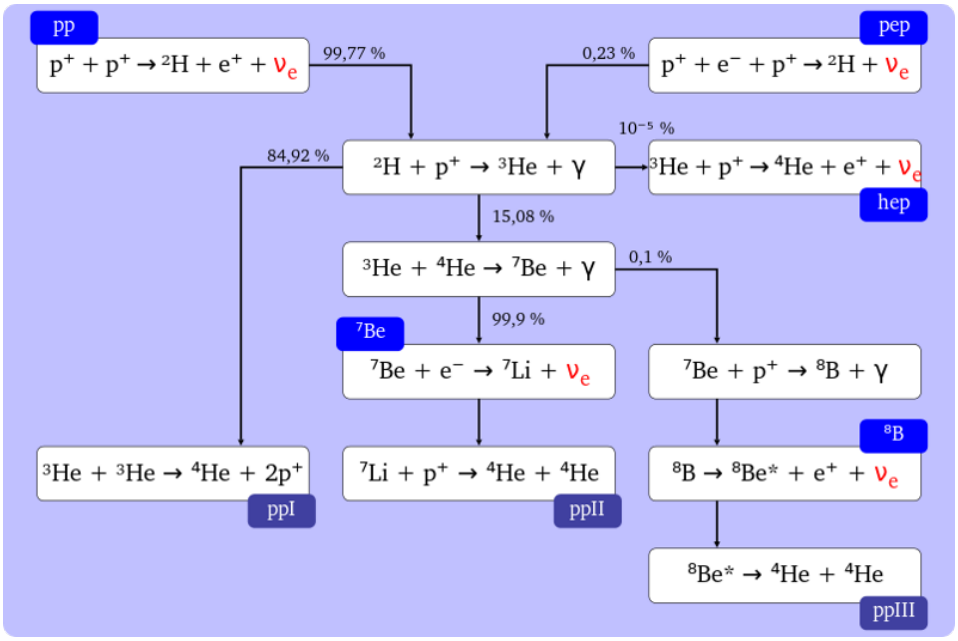

Figure 1.3: The *pp*-chain in the sun [31].

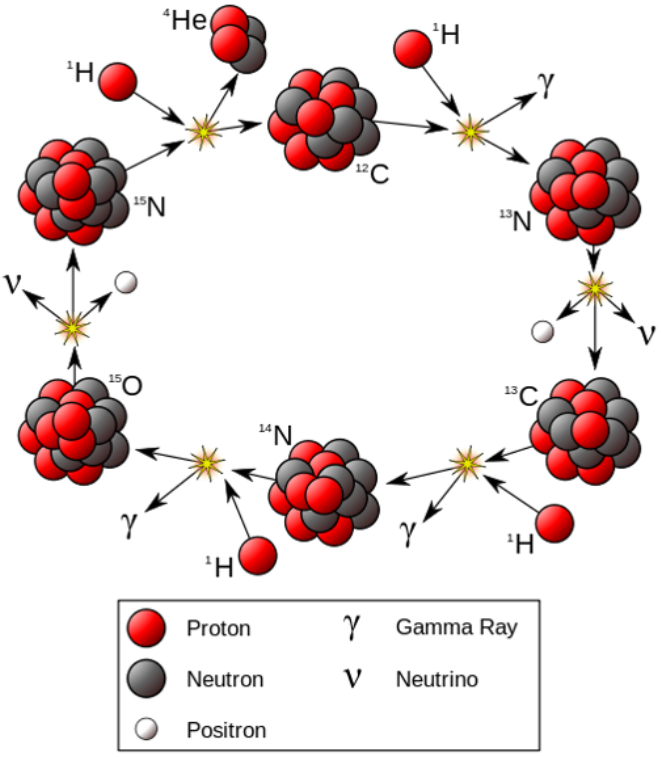

Figure 1.4: The CNO cycle in the sun [32].

the neutrino production chains is given by,

$$\pi^+ \to \mu^+ \nu_\mu \quad \text{and} \quad \mu^+ \to e^+ \nu_e \overline{\nu}_\mu \ ;$$
$$\pi^- \to \mu^- \overline{\nu}_\mu \quad \text{and} \quad \mu^- \to e^- \overline{\nu}_e \nu_\mu \ .$$

The additional contribution of neutrinos comes from kaon decays:

$$K^\pm \to \mu^\pm \nu_\mu(\overline{\nu}_\mu) \ , \ K_L \to \pi^\mp e^\pm \nu_e(\overline{\nu}_e) \ \text{and} \ K_L \to \pi^\mp \mu^\pm \nu_\mu(\overline{\nu}_\mu) \tag{1.2}$$

The atmospheric neutrinos have been detected by the Super-Kamioka collaboration [33].

1.1.7 Geo-neutrinos

The third major natural source of neutrinos on the earth is from the interior of the earth's core. The radioisotopes like ^{238}U, ^{232}Th, ^{40}K inside the earth emit the electron type anti-neutrinos with energies of a few MeV. These neutrinos are the probes to study the inner heating mechanism of the earth's interior. The KamLAND [34] and Borexino [35] experiments have detected the geo-neutrinos.

1.1.8 Reactor Neutrinos

Nuclear reactors are a major source of the electron type anti-neutrinos. In the nuclear reactors, the radioisotopes like ^{238}Th, ^{235}U, ^{241}Pu and ^{239}Pu are used as a fissile material. All these isotopes will undergo fission process; consequently, they emit neutrinos in the few MeV energy range. These have been detected by KamLAND [36, 37], CHOOZ [38, 39], Daya Bay [40], RENO [41] etc.

1.1.9 Accelerator Neutrinos

Another artificial source of neutrinos are particle accelerators. In the accelerator, protons are accelerated to attain the high energy and collide with a fixed target made of graphite sheet, where secondary hadrons will be produced. The pions from the interaction point are focused using magnetic horns and allowed to decay to muons and neutrinos. The muons are stopped using the heavy materials in the path, so that only neutrinos will travel towards the detector. The accelerator-based neutrinos are used to achieve the high flux of neutrinos with desired energy and direction. For example, T2K [42], NOvA [43] experiments have studied these accelerator neutrinos.

1.1.10 Supernova Neutrinos

The explosion of a massive star results in a supernova and they are the source of extremely luminous neutrinos. The number of neutrinos emitted from a supernovae within $\sim 10\,\mathrm{s}$ is equal to the number of neutrinos emitted by the sun for its lifetime. Neutrinos produced in these processes have energies in the range of few 10s of MeV. The neutrinos observed from the supernovae explosion happens in two different stages, (i) the de-leptonization burst as the outgoing shock passes the neutrinosphere, which results in the emission of ν_e and (ii) the second part is from the Kelvin-Helmholtz cooling phase of the protoneutron star, which results in the emission of all type of neutrinos (ν_e, $\overline{\nu}_e$, ν_μ, $\overline{\nu}_\mu$, ν_τ, $\overline{\nu}_\tau$).

Neutrinos emitted from supernovae carry about $99\,\%$ of the energy released in the explosion. Neutrinos from one such supernova was observed in 1987 (called SN1987A) [44, 45]. This was the brightest supernova explosion to occur since after Kepler's supernovae in 1604. The detection of neutrinos from 1987A opened up a new field called neutrino astrophysics.

As discussed, the neutrinos produced in the stars and supernovae have energy

in the range of few to 10s of MeV. There are other astrophysical sources like active galactic nuclei and cosmogenic neutrinos with energy ranges from TeV to EeV. The flux of these neutrinos is extremely small. ICECUBE neutrino observatory reported the detection of these types of neutrinos [46–48].

1.2 Neutrino Oscillation

Recent experimental evidence from solar, atmospheric, reactor and accelerator neutrinos show that neutrinos can undergo flavour transformation during propagation, which requires the non-zero masses (actually non-zero mass-squared differences) of neutrinos. The non-zero masses of neutrinos and neutrino oscillation cannot be explained within the Standard Model. Thus, the mechanism of neutrino oscillation leads to the first evidence of new physics beyond the Standard Model. This is the primary motivation for the proposal for INO, as of many more neutrino detectors around the world. A short summary of neutrino oscillations is given below.

A non-vanishing mass of neutrinos leads to the possibility of having mixing among the neutrino flavours. Hence the neutrino flavour states (ν_e, ν_μ and ν_τ) are not eigenstates of the mass but are linear combinations of three mass eigenstates (ν_1, ν_2 and ν_3). This allows the phenomenon called neutrino oscillations, which is a kind of flavour oscillation and is already established in the quark sector.

Let us assume n number of orthonormal eigenstates. The n flavour eigenstates are connected to n mass eigenstates via a unitary mixing matrix U called PMNS matrix:

$$|\nu_\alpha\rangle = \sum_i U_{\alpha i} |\nu_i\rangle \ ; \text{ and } \ |\nu_i\rangle = \sum_\alpha (U^\dagger)_{i\alpha} |\nu_\alpha\rangle \ , \tag{1.3}$$

with the conditions, $U^\dagger U = 1$, $\sum_i U_{\alpha i} U^*_{\beta i} = \delta_{\alpha\beta}$ and $\sum_\alpha U_{\alpha i} U^*_{\alpha j} = \delta_{ij}$.

In the case of anti-neutrinos, $U_{\alpha i}$ in Eq. 1.3 is replaced by $\mathrm{U}^*_{\alpha i}$. The connection

between the mass eigen states and flavour eigen states for antineutrinos is therefore,

$$|\overline{\nu}_\alpha\rangle = \sum_i U^*_{\alpha i} \, |\overline{\nu_i}\rangle \ . \tag{1.4}$$

In the case of three flavour neutrino oscillations, the unitary mixing matrix (U_{PMNS}) is defined as,

$$U_{PMNS} = \begin{pmatrix} 1 & 0 & 0 \\ 0 & c_{23} & s_{23} \\ 0 & -s_{23} & c_{23} \end{pmatrix} \begin{pmatrix} c_{13} & 0 & s_{13}e^{-i\delta_{CP}} \\ 0 & 1 & 0 \\ -s_{13}e^{i\delta_{CP}} & 0 & c_{13} \end{pmatrix} \begin{pmatrix} c_{12} & s_{12} & 0 \\ -s_{12} & c_{12} & 0 \\ 0 & 0 & 1 \end{pmatrix} \begin{pmatrix} e^{i\alpha_1/2} & 0 & 0 \\ 0 & e^{i\alpha_2/2} & 0 \\ 0 & 0 & 1 \end{pmatrix}$$

where, $c_{ij} = \cos\theta_{ij}$, $s_{ij} = \sin\theta_{ij}$, δ_{CP} is the CP-violating phase and α_1 and α_2 are the Majorana phases which are not observable in neutrino oscillation physics.

The transition probability for a neutrino with flavour ν_α to oscillate into a given flavour ν_β over a time t or path length L is given as,

$$\begin{aligned} P(\nu_\alpha \to \nu_\beta) =& \delta_{\alpha\beta} - 4 \sum_{i>j} \mathrm{Re}\left(K_{\alpha\beta\,,ij}\right) \sin^2\left(\frac{\Delta m^2_{ij} L}{4E}\right) \\ &+ 2 \sum_{i>j} \mathrm{Im}\left(K_{\alpha\beta\,,ij}\right) \sin\left(\frac{\Delta m^2_{ij} L}{2E}\right) \ , \end{aligned} \tag{1.5}$$

where $K_{\alpha\beta\,,ij} = U_{\beta i} U^*_{\alpha i} U^*_{\beta j} U_{\alpha j}$ and $\Delta m^2_{ij} = m^2_i - m^2_j$, and E is the energy of the neutrino. If we consider 2-flavour mixing, the equation simplifies to,

$$P(\nu_\alpha \to \nu_\beta) = \sin^2 2\theta \, \sin^2\left(\frac{\Delta m^2 L}{4E}\right) \ , \tag{1.6}$$

where E and L are the energy and path length of the neutrinos.

The transition probability discussed above is for neutrino oscillation in a vacuum. The oscillation probability of the neutrinos as it passes through matter is different due to coherent forward scattering with electrons, protons and neutrons in the matter. This phenomenon is known as matter effect. As we know, all type of neutrinos interacts with matter via neutral current interactions, but electron-type

neutrinos can interact with electrons via charged current interactions:

$$\begin{aligned} \nu_x + e^-/p/n &\rightarrow \nu_x + e^-/p/n \text{ (NC)} ; \\ \nu_e + e^- &\rightarrow \nu_e + e^- \qquad \text{(CC)} . \end{aligned}$$

The Hamiltonian of the system is rewritten to incorporate the matter potential; the modified Hamiltonian is,

$$H_m = H_0 + V_f \ , \tag{1.7}$$

where H_0 corresponds to the free particle Hamiltonian and V_f is the matter potential. In the case of two flavour mixing, the V_f is,

$$V_f = \begin{pmatrix} V_{CC} + V_{NC} & 0 \\ 0 & V_{NC} \end{pmatrix} \ , \tag{1.8}$$

where $V_{CC} = \pm\sqrt{2}G_F n_e$ (+ sign for neutrinos and − sign for anti-neutrinos) and $V_{NC} = -G_F n_n/\sqrt{2}$, where G_F, n_e and n_n are the Fermi coupling constant, number density of electrons and number density of neutrons respectively. Neutrinos do not only NC scatter on electrons, but also on protons and neutrons. In an electrically neutral medium, the electron and proton contributions to V_{NC} will cancel, leaving only the neutron contribution. The transition probability for the oscillation in matter can then be expressed in terms of a matter-dependent mass-squared difference and the mixing angle, viz.,

$$P(\nu_\alpha \rightarrow \nu_\beta) = \sin^2 2\theta_m \, \sin^2\left(\frac{\Delta m^2_m L}{4E}\right) \ , \tag{1.9}$$

where Δm^2_m and θ_m are the mass squared difference and mixing angle in matter.

The relation between mass squared difference in vacuum and matter is given as,

$$\begin{aligned} \Delta m^2_m &= C\Delta m^2 \ ; \\ \sin 2\theta_m &= \sin 2\theta / C \ ; \\ C &= \sqrt{(\cos 2\theta - A)^2 + \sin^2 2\theta} \ ; \\ A &= \pm \frac{2\sqrt{2} G_F n_e E}{\Delta m^2} \ . \end{aligned} \tag{1.10}$$

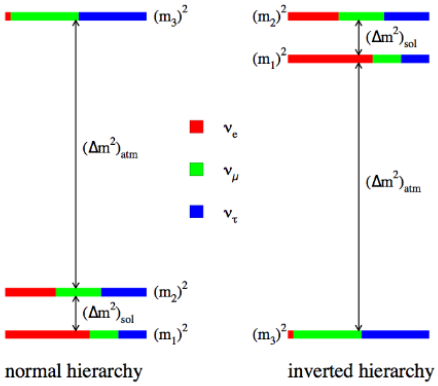

Figure 1.5: Normal and inverted ordering of neutrino masses. The color band represents the contribution of the flavour states in the mass eigen states [49].

Parameter	Normal hierarchy		Inverted hierarchy ($\Delta\chi^2$=7.1)	
	Bfv $\pm$ 1 σ	3 σ range	Bfv $\pm$ 1 σ	3 σ range
$\Delta m^2_{21} (10^{-5}\, eV^2)$	$7.42^{+0.21}_{-0.20}$	6.82 $\rightarrow$ 8.04	$7.42^{+0.21}_{-0.20}$	6.82 $\rightarrow$ 8.04
$\Delta m^2_{3l} (10^{-3}\, eV^2)$	$+2.517^{+0.026}_{-0.028}$	2.435 $\rightarrow$ 2.598	$-2.498^{+0.028}_{-0.028}$	-2.581 $\rightarrow$ -2.414
$\theta_{12}(^\circ)$	$33.44^{+0.77}_{-0.74}$	31.27 $\rightarrow$ 35.86	$33.45^{+0.78}_{-0.75}$	31.27 $\rightarrow$ 35.87
$\theta_{23}(^\circ)$	$49.2^{+0.9}_{-1.2}$	40.1 $\rightarrow$ 51.7	$49.3^{+0.9}_{-1.1}$	40.3 $\rightarrow$ 51.8
$\theta_{13}(^\circ)$	$8.57^{+0.12}_{-0.12}$	8.20 $\rightarrow$ 8.93	$8.60^{+0.12}_{-0.12}$	8.24 $\rightarrow$ 8.96
$\delta_{CP}(^\circ)$	197^{+27}_{-24}	120 $\rightarrow$ 369	282^{+26}_{-30}	193 $\rightarrow$ 352

Table 1.1: The tabulated values of neutrino oscillation parameter from the global analysis [50, 51]. Δm^2_{3l}=Δm^2_{31} >0 for NO and Δm^2_{3l}=Δm^2_{32} <0 for IO.

At resonance the parameter $A = \cos 2\theta$. Even if the mixing angle in vacuum is small, due to interaction with matter, the mixing angle can become $\theta_m = \pi/4$ which is maximum. This maximum mixing angle causes an enhancement in the transition probability from one flavour to another. This effect is known as the Mikheyev-Smirnov-Wolfenstein (MSW) effect [52, 53].

At the same time, the transition probability of the neutrinos and anti-neutrinos differs in the presence of matter effect due to the differing sign of A (as well as the effect of the CP phase). The resonance occurs only if $A > 0$, which depends on the sign of Δm^2. This dependence of the sign of Δm^2 helps to determine the neutrino mass hierarchy.

Many experiments in the world are designed to study these mixing angles and mass squared differences. The present status of the neutrino parameters from the global analysis [50, 51] is given in Table 1.1. The value and sign of Δm^2_{21} ($\sim \Delta m^2_{sol}$) and mixing angle θ_{12} ($\sim \theta_{sol}$) are well determined from the solar and reactor neutrinos. The absolute value of Δm^2_{32} is determined by atmospheric and accelerator neutrino experiments, but the sign of this term is yet to be determined. The unknown knowledge about the sign of Δm^2_{32} causes ambiguity in the neutrino mass ordering. If the neutrino mass states are ordered according to $m_3 > m_2 > m_1$, it is called normal hierarchy. If the ordering follows $m_2 > m_1 > m_3$, it is called inverted ordering (shown in Fig. 1.5). The planned ICAL detector at INO will use the magnetic field to distinguish the sign of the muons produced in charged-current muon neutrino interactions (from the atmosphere) and hence enable a separation of neutrino and anti-neutrino events at the same time to determine the neutrino mass ordering. The detailed physics studies about INO-ICAL can be found from Ref. [54]. Brief discussion on the mass hierarchy analysis is discussed further. Fig 1.6 shows the mass hierarchy sensitivity of ICAL with muon alone and inclusion of hadron enrgy information for normal and inverted ordering. The mass hierarchy identification usign only muon information yields $\Delta\chi^2_{ICAL-MH} \approx 6.5$ with 10 year exposure of 50 kt ICAL (Fig 1.6 (black dashed curve)). If hadron energy information is used, the exposure time allows to identify with a significance of $\Delta\chi^2_{ICAL-MH} \approx 9.5$ (Fig 1.6 (red solid curve)). Fig. 1.7 shows the comparison of the $\sin^2\theta_{23}$-Δm^2_{32} plane of 50 kt ICAL in 10-year reach with other experiments. The precision of Δm^2_{32} using ICAL would be much better measurement than any other

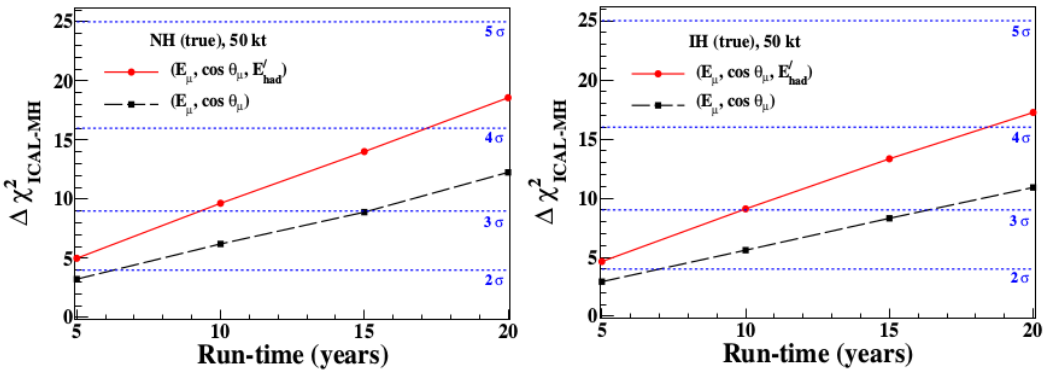

Figure 1.6: The hierarchy sensitivity of ICAL with input normal (left) and inverted (right) hierarchy including correlated hadron energy information [54].

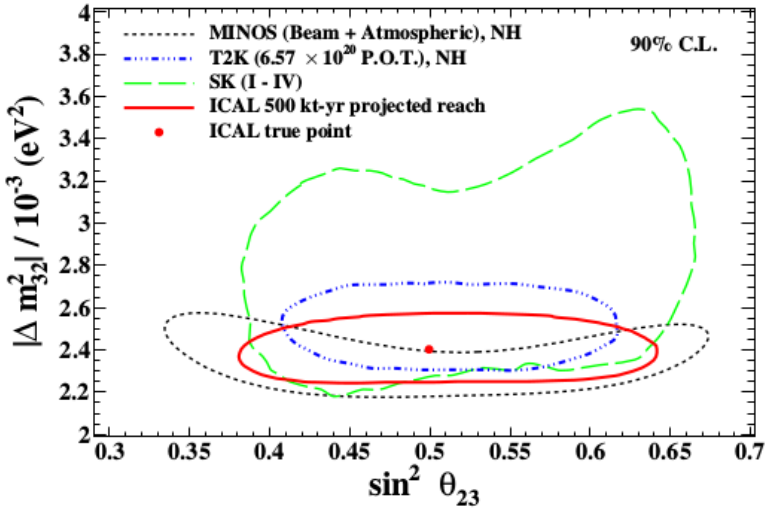

Figure 1.7: The precision reach of ICAL in the $\sin^2\theta_{23}$-Δm^2_{32} plane, in comparison with other current and planned experiments [54].

atmospheric neutrino experiment uses water cherenkov detector becaue of its better energy measurement capability. At the same time, INO can not compete with beam experiment because of its more data accumulation. Hence the global role of ICAL for the measuring the neutrino oscillation parameters are not competetive with beam experiments but it can be complementary. It is expected that, ICAL will reach $2\,\sigma$ in 5-years and $3\,\sigma$ in 10-years [55]. But DUNE experiment will reach its $3\,\sigma$ in 3-years and $5\,\sigma$ in 7-years [56].

1.3 Cosmic rays

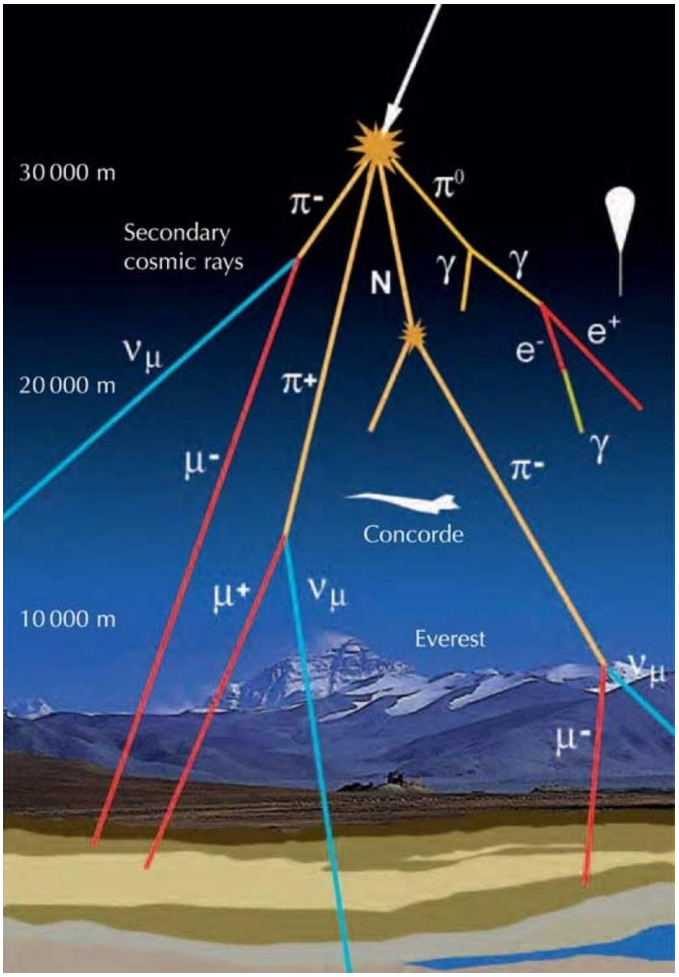

Figure 1.8: The interaction of primaries in the earth atmosphere [57].

Details about the cosmic radiation are explained in [58]. Cosmic rays mainly originate from outside of the solar system. The primary sources of these are cosmic rays from a supernova explosion, extra-galactic nuclei, etc. The cosmic rays consist of a proton (∼90 %), helium nuclei(∼9 %) and the remaining are high atomic number nuclei like carbon, nitrogen, oxygen and γ-rays etc. The cosmic rays are influenced by interplanetary magnetic fields, intergalactic magnetic fields, the magnetosphere and geomagnetic field while approaching the earth. The electrically charged secondary cosmic rays produced in the earth's atmosphere are also influenced by geomagnetic effects. Other than the above-specified reasons, there is also

an effect due to the 11 year and 22-year solar cycle activity due to the flip in the polarity of the Sun's dipole. The modulation is larger for the primaries having smaller energies; the effect will decrease with increasing cosmic ray energy. The cosmic rays entering the earth atmosphere undergo interactions with electrons and nuclei of atoms and molecules in the air. The incident hadrons undergo strong interactions when they collide with atmospheric nuclei such as nitrogen and oxygen. The collision of energetic particles with atmospheric nuclei creates a shower of particles. The most abundant secondary particles are pions, due to their small mass, resulting in larger phase space. Kaons, hyperons, charmed particles and nucleon-anti-nucleon pairs are also produced. A typical example of the primary cosmic ray interaction with atmosphere shown in figure 1.8. The energetic primary protons undergo an average of 12 interactions along a vertical trajectory through the atmosphere down to sea level, with the corresponding mean free path of about $80\,\mathrm{g/cm^2}$.

Most of the primaries with higher atomic numbers are fragmented in the first interaction that occurs at a higher altitude than for protons due to their larger interaction cross-section, $\sigma_i\,[\mathrm{cm^2}]$, and corresponding shorter mean free path, λ_i. The Eq. 1.11 shows the relation between the cross-section and mean free path:

$$\frac{1}{\rho\lambda} = \frac{N_A}{A}\sigma_i \ , \tag{1.11}$$

where N_A is the Avogadro number, A the mass number of the target and σ_i the cross section for the particle interaction with matter. The secondaries produced in the interaction of the primary particle with air nuclei continue to propagate through the atmosphere and contribute to the hadron flux in the atmosphere. The energetic secondary hadrons will initiate new hadronic interactions and produce further hadron cascades. Other than hadronic interactions, the unstable hadrons are also prone to decay. The mean lifetime, the energy of the particle and the

density of the medium which the particle traverses, decide whether the particle decays or it will interact with the medium. The secondary particle has a momentum or energy spectrum similar to the primary spectrum. If the differential energy spectrum of the primaries above few GeV follow the power-law $aE^{-\gamma_p}$, the secondaries will follow a similar power-law $bE^{-\gamma_s}$. The muon flux measured by different experimental group is given in Fig. 1.9 (The figure is adapted from [59]).

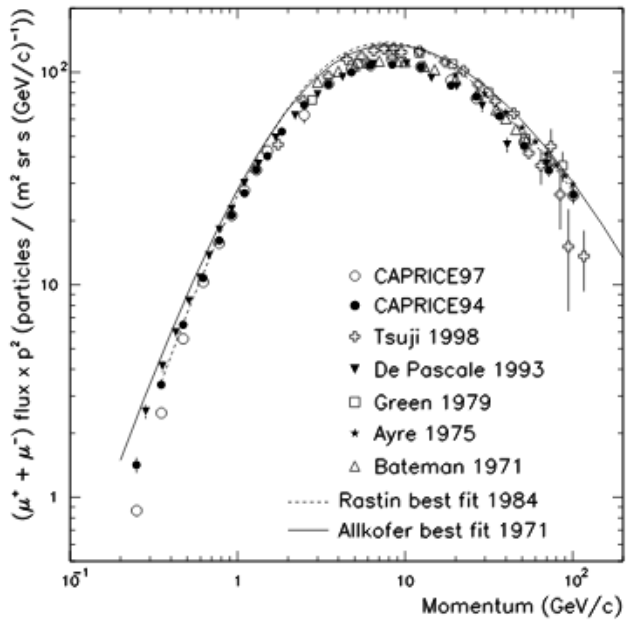

Figure 1.9: The momentum spectrum of the muons from different site [59].

The lifetime of the charged pions at rest is 2.6×10^{-8} s and interaction mean free path is $\sim$120 g/cm^2 in air. The charged pions mostly decay weakly, via $\pi^+ \rightarrow \mu^+ + \nu_\mu$ and $\pi^- \rightarrow \mu^- + \overline{\nu}_\mu$. The mean lifetime of muons is τ_0=2.2 μs, which is enhanced due to time dilation, so that most of the muons reach sea level. Muons are the most abundant charged particle at the sea level. The muons again can decay via weak interaction to produce electrons and and neutrinos, the decay channel for μ^+ and μ^- are $\mu^+ \rightarrow e^+ + \nu_e + \overline{\nu}_\mu$ and $\mu^- \rightarrow e^- + \overline{\nu}_e + \nu_\mu$ respectively. The neutral pions have a mean lifetime of 8.4×10^{-17} s and mainly decay to 2γ via electromagnetic interaction. Later the γ produce electron-positron pairs, which will create electromagnetic cascade in the extensive air shower. The decay probability

of the unstable particle, after traversing a thickness of X g/cm^2 in the vertical direction, with rest mass m_0, mean lifetime (τ_0), momentum (p) and the given medium density (ρ) is given as,

$$W \approx \frac{m_0 X}{\rho \tau_0 p} \ , \tag{1.12}$$

The particle traversing in an inclined direction will have an enhancement due to the zenith angle dependence,

$$W \approx \frac{m_0 X}{\rho \tau_0 p} \, sec(\theta) \ , \tag{1.13}$$

The survival probability of muons reaching the sea level is given as,

$$S_\mu = 1 - W_\mu \ , \tag{1.14}$$

The decay probability of the pions and kaons at depth of 100 g/cm^2 is given in [58] and the survival probability of the muons produced at the atmosphere depth of 100 g/cm^2 to reach sea level is also shown in [58]. The attenuation of various secondary particle fluxes in the atmosphere is different due to specific interaction mechanism. The survival probability of relativistic particles to reach the earth depends on the point of production, charge, energy, zenith angle and the lifetime. The energetic protons and neutrons mostly interact via strong interaction; heavy nuclei are fragmented in collision with nuclei in air molecules. The electrons and photons lose energy via electromagnetic interaction. All the charged particles in addition have energy loss by ionization. Particles with mean lifetime shorter than 10^{-12}s have very less probability to reach the sea level from the higher production point. Muons with a mean lifetime of 2.2 μs will have more probability to reach the sea level, which increases with momentum of the muons. The flux of particles at atmosphere and sea level will be influenced by many factors such as latitude,

longitude, altitude and the atmosphere density etc. The measurement of different secondaries fluxes at sea level is given in [58].

1.3.1 Dependence of cosmic muon flux on the detector location

As mentioned earlier, a major source of neutrinos on the earth is from the cosmic ray interaction with the earth's atmosphere. The energy range of these neutrinos is very broad. It starts from few MeV and extends up to PeV. The neutrinos produced in these interactions are called atmospheric neutrinos. The sources affects the muon or neutrino flux estimation are listed below,

- *Primary Cosmic Ray:* The CR spectrum measurements acquired from the recent experiments help to improve the systematic on the atmospheric muon and neutrino flux calculation. The momentum spectrum, spectral index and chemical composition of primary cosmic rays are well measured from the experiments such as AMS-II [60, 61], PAMELA [62], BESS-polar [63] and etc. The precise measurement of the proton flux between rigidity (momentum/charge) of 1 GV to 1.8 TV and the Helium flux between the rigidity of 1.9 GV to 3 TV are performed by Alpha Magnetic Spectrometer (AMS) placed on the International Space Station (ISS). The measurement from AMS-02 [60, 61] shows that the primary spectrum deviates from a single power law, and also the spectral index progressively hardens after above 100 GV. The magnitude of the spectral index for proton is larger in comparison with helium but the shape of the rigidity dependence is similar for proton and helium. Thus, the systematics related to primary flux upon the estimation of the muon flux and neutrino flux in the energy range up to few 10 GeV (where INO is interested) is minimal.

- *Solar Modulation:* The primary cosmic ray with energy below 20 GeV is modulated by the solar activity. As the Solar activity varies with a pseudo periodicity of 11 or 22 years, the low energy cosmic ray spectrum is modulated and varies with the same periodicity, for $E < 20\,\text{GeV}$. This phenomenon is called the Solar modulation of cosmic ray. This modulation is caused by the solar wind which pushes back the galactic cosmic ray. Then when the Solar activity is high, the cosmic ray spectrum is low, and when Solar activity is low, the cosmic ray spectrum is high. The detailed discussion on the time-dependent solar modulation of cosmic rays and its recent measurements are summarised in Ref. [64]. The accelerated CR particles from sources are injected and propagated in the Galactic interstellar medium. The intensities of CRs entering the heliosphere is significantly affected by many effects, such as the CRs interactions with the outward solar wind. The CR spectra observed is modulated with the solar activity cycle, and are different from those outside the heliosphere, namely the Local Interstellar Spectra (LIS). The study of solar modulation is vital to understand the flux at low energies ($E \leq 30\,\text{GeV}$) and also helps in understanding the physics in the CR-heliosphere interaction. The Voyager 1 (crossed the boundary of heliosphere since August 2012) gives direct measurements of LIS from a few 100s of MeV/nucleon. The systematic measurement of CR proton spectrum in a wide energy range of 80 MeV to 50 GeV in the period of 2006-2014 from the late declining phase of 23rd solar cycle to the maximum of the 24th cycle. Besides, the ACE and BESS experiments and Voyager-1 measures the low energy LIS of CR nuclei. The CRs with energy above a few 10s of GeV is not getting affected by this solar modulation. However, the rigidity cutoff at the present experimental site and INO site is around 17 GV, thus this effect is not seen in muon flux there.

- *Geomagnetic field:* Other than the solar activity, the primaries entering inside the earth's magnetosphere is influenced by the geomagnetic field. The

presence of the geomagnetic field prevents low energy cosmic rays entering inside the earth's atmosphere. Liouville's theorem ensures the uniformity of cosmic ray at the place where cosmic ray can arrive. However, if anything obstructs the cosmic ray, the uniformity is lost. Similarly to the magnetic shield of a charged particle, the low rigidity cosmic rays are obstructed by the geomagnetic field, and this phenomenon is called the rigidity cutoff. The East-West effect is explained by the combination of the obstructions by the geomagnetic field and by the surface of the Earth. The muons produced in the atmosphere also bend in the earth magnetic field and causes the enhance in the asymmetry in the μ^+ but in the case of μ^- the asymmetry reduces. In the case of the dipole geomagnetic field model, often Stormer's analytic formula shown in Eqn. 1.15 [65] is used to estimate the rigidity cutoff.

$$R_s^{\pm}(r, \lambda_M, \theta, \phi) = \frac{M}{r^2} \frac{cos^4 \lambda_M}{(1 + (1 \mp cos^3 \lambda_M \, sin\theta \, sin\phi)^{1/2})^2} \tag{1.15}$$

where r and λ_M are the distance from the center of the earth, geomagnetic latitude, and θ and ϕ are the arrival direction of the cosmic rays, and the value of $M = 8.1 \times 10^{25}\,\mathrm{G\,cm^3}$ is the magnetic dipole moment of the earth. However, the actual geomagnetic field is more complicated and it is not as simple as dipole approximation. It is generally expressed as a multipole expansion. The back tracing method using computer simulation is used generally to estimate the rigidity cutoff. The cut off rigidity depends on the location on the earth's surface and the direction of the incident particle. The geomagnetic field produces two prominent effects on cosmic rays, (i) the latitude effect and (ii) the east-west effect.

- *The Earth Atmosphere Model:* The atmosphere is another important element for the estimation of atmospheric neutrino and muon fluxes. In the calculation of atmospheric neutrino and muon fluxes, the US-starndard'76 [66]

model has been used for a long time. However, only height dependence of composition, density, and temperature are described in the model, and there is no position dependence or the seasonal variation. In newer atmosphere model, the position dependence and the seasonal variation are added, but they are almost the same with US-standard'76 in one year average in the region with $|\text{latitude}| \leq 50^\circ$, and seasonal variation is seen little in near equatorial region. Since the present experiment and INO site are located in 10°N, the US-standard'76 is enough for the prediction of atmospheric neutrino and muon fluxes.

- *Hadronic interaction model:* Thus, the necessary knowledge of geophysical elements is almost understood enough. The remaining large uncertainty in the calculation of atmospheric neutrino and muon fluxes is in the hadronic interaction. However, the uncertainty of hadronic interaction necessary for the calculation of atmospheric neutrino could be calibrated by the atmospheric muon flux. The production process of the atmospheric neutrino is similar to that of the atmospheric muon, just the difference is the muon can create the neutrino when it decays. The recent work from Ref. [67] discusses the reduction of the uncertainties in the neutrino flux calculation below 1 GeV with an input of accurately measured muon flux, and also the calculated muon flux at various observation site such as near Kamioka at sea level, same but 2770 m a.s.l, Hanle India (4500 m a.s.l), and at Balloon altitude (32 km) are also described.

Uncertainties in the knowledge of the interaction models will severely impact the calculations of the atmospheric neutrinos which are produced from the decays of secondary cosmic ray particles. Hence, before performing neutrino experiments using atmospheric neutrinos, it is important to measure accurately the cosmic muon flux. In particular, this is an important input for the India-based Neutrino

Observatory (INO) experiment that is proposed to be located a short distance away from the site of the present study. This is the main focus of this thesis.

1.4 INO-experiment

In the early 1960s, the existence of atmospheric neutrinos was first reported from the experiment done in Kolar Gold Field, Karnataka, India [68, 69]. This was the earliest effort of India in the field of experimental neutrino physics. The India-based Neutrino Observatory (INO) [54] is a proposed multi-institutional collaboration project funded by the Indian government to unravel the mystery of the neutrinos. The proposed INO is to be constructed in Bodi West hills, Tamilnadu, the southern part of India. The facility will have an underground lab with a rock coverage of $\sim 1\,\text{km}$ in all directions to suppress the muon background from cosmic rays.

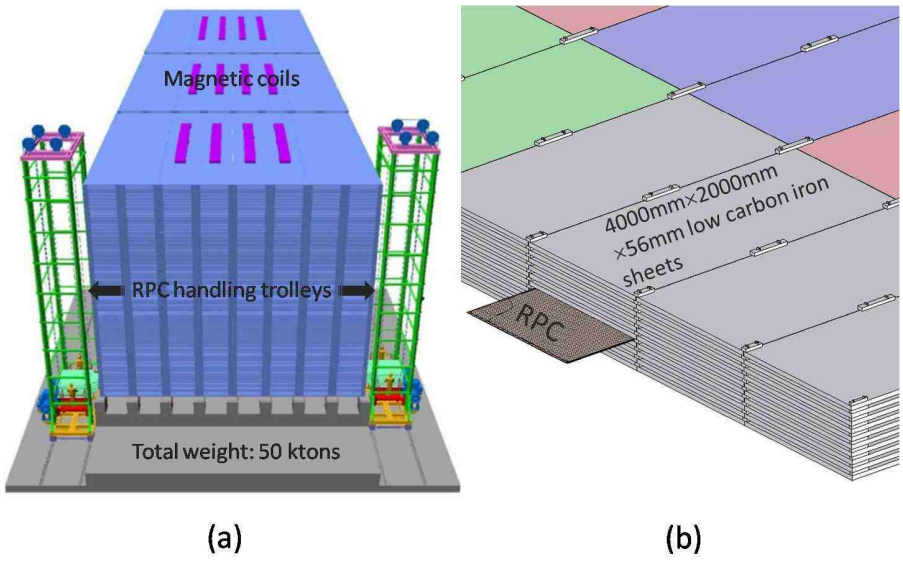

Figure 1.10: Schematic of (a) the three ICAL detector modules and (b) Insertion of RPCs between iron plates [70].

The main goals of the proposed magnetised Iron Calorimeter Detector at India-based Neutrino Observatory are to make precise measurements of neutrino oscillation parameters including the sign of Δm^2_{32} through the earth matter effects, and the study of non-standard interactions of neutrinos.

No. of Modules	3
Modular dimension	$16\,\text{m} \times 16\,\text{m} \times 14.5\,\text{m}$
Total dimension	$48\,\text{m} \times 16\,\text{m} \times 14.5\,\text{m}$
No. of iron layers	151
Thickness of Iron plate	5.6 cm
Gap for RPC assembly	4 cm
Magnetic field	1.5 T
RPC unit dimension	$174\,\text{cm} \times 183.5 \times 1.8\,\text{cm}$
Width of readout strip	2.8 cm
Total RPC units	28,800
No. of electronic channels	$\sim 3.7 \times 10^6$

Table 1.2: Specification of ICAL detector.

The oscillation probability of neutrinos and anti-neutrinos differ in the presence of matter. To determine the mass ordering through the matter effect, the oscillation probability of neutrinos and anti-neutrinos has to be studied independently. In order to achieve this, ICAL is designed to measure the precise energy, direction and sign of the charge of the muons produced in the charged current interaction of the muon neutrinos in the target. ICAL will have excellent charge identification capability to discriminate μ^+ and μ^- because it will be the world's largest man-made electromagnet. Hence it can achieve a good separation of ν_μ and $\overline{\nu}_\mu$ events.

To achieve good momentum and direction reconstruction of muons in the ICAL, it is desired to have good tracking detectors with a reasonable position resolution and timing resolution. The ICAL detector will be made of alternating layers of iron plates and active detectors. The dimension of the ICAL is $48\,\text{m} \times 16\,\text{m} \times 14.5\,\text{m}$ in three modules of 17 kTons each. In total, 151 layers of iron plates will be used, each plate having a thickness of 5.6 cm. In between the iron plates, the active detectors will be inserted. The Resistive Plate Chambers (RPCs) have been chosen as the active detector in ICAL. Each RPC in ICAL will have area of $\sim 2\,\text{m} \times 2\,\text{m}$. The total number of RPCs to be used in ICAL is $\sim$28000 RPC detectors. The graphical view of the ICAL detector is shown in Fig. 1.10 (figure from Ref. [70]). The important ICAL detector specifications are listed in Table 1.2.

1.4.1 Scope of this thesis

1.4.1.1 Measurement of the cosmic muon flux at Madurai

The physics results presented in this thesis is from the RPC Only Stack. The present experimental stack made of only RPCs was used to study the flux of cosmic ray muons at the experimental site. The experimental site is located 100 km east from the INO-site. The site is located close to the geomagnetic equator. This location is so unique since there is no other neutrino experiments constructed near the equator. The goals are the following.

- In order to study neutrino oscillation parameters using atmospheric neutrinos, it is vital to understand details about the atmospheric neutrino fluxes such as the flux ratio $(\nu_\mu + \overline{\nu}_\mu)/(\nu_e + \overline{\nu}_e)$ and the angular dependence of the neutrino flux at the experimental site. The various sources, starting from the hadronic interaction of the primaries in the atmosphere to the muon flux at the surface, are the main contributors to the uncertainty in the neutrino flux calculation. The pion decay is the main source of neutrinos below 1 TeV energies. The experimentally recorded muon flux at various locations on the earth have been used to tune the hadronic interaction models to reduce the uncertainty in the production of pions in the primary interaction. The calibration procedure for the interaction models and the detailed calculation of the neutrino flux has been done by Honda et al. [67, 71] based on the known cosmic muon fluxes at different locations, extrapolated to the present location and may thus include large theoretical uncertainties. This is the motivation for measuring the muon flux at the experimental site.

- As a first part of the muon flux measurement, the zenith angle spectrum and integral intensity of cosmic ray muons are measured using the data collected in the first phase of the experiment. As we know, the zenith angle spectrum of the cosmic muons follows $I(\theta) = I_0 \cos^n \theta$ (where I_0 is the integral intensity

of vertical muons and n is the zenith angle-dependent exponent). The value of n and I_0 were estimated using the data are presented in Chapter 5.

- The muon data collected from the phase-II study with up-graded electronics was used to calculate the muon flux in different θ-ϕ bins. The azimuthal dependence of the cosmic muons at different zenith angular bins were studied. The variation in the azimuthal spectrum due to systematics related to the detector, input momentum spectrum and material descriptions were also measured and are discussed in Chapter 5).

Chapter 2

Experimental Setup

Two main configurations have been used to study the cosmic muon flux at IICHEP, Madurai. In this chapter, we describe the details of the experimental configurations. In the next chapter, we will present details of the experimental observations, including the precise location, etc., that were used to collect the data for the present analysis.

2.1 RPC-Only Stack

In the configuration that was eventually used for the analyses presented in this thesis, a stack of active detector elements, the RPCs, was used. Twelve RPCs of dimension 2 m $\times$ 2 m were stacked vertically, about 17 cm apart, as shown in Fig. 2.1. Since only air filled the spaces between the RPCs, there was very little energy loss of the cosmic muons while passing through the stack. The RPCs were mounted on an aluminium support structure. The detailed discussion about the design and characterisation of INO-RPCs is given in Ref. [72]. The graphical view of the detector stack is shown in Fig. 2.1. Some details on the construction and operation of RPCs are given below for completeness.

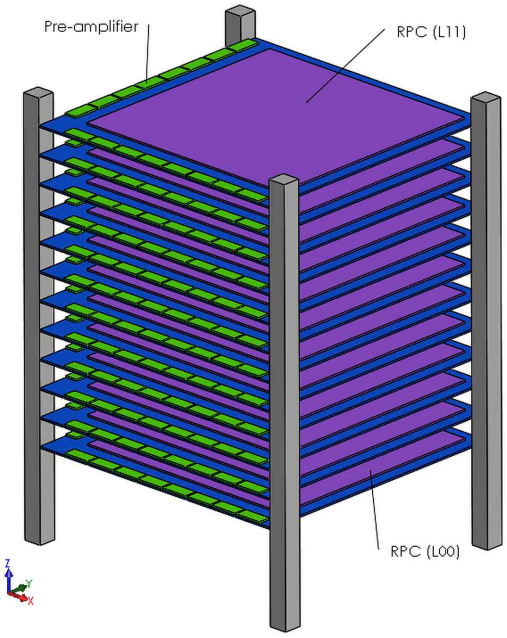

Figure 2.1: The graphical view of the RPC Stack.

2.2 Mini-ICAL

A scaled version of the actual ICAL detector, the mini-Iron CALorimeter (mini-ICAL), has recently been commissioned in IICHEP-Madurai. The size of the detector is $1/200^{th}$ of one 17 kton module of the proposed ICAL. The mini-ICAL detector is made of 11 layers of 4 m×4 m size iron plates and 10 layers of 2 m×2 m size RPCs which are inserted between the iron plates. The fully assembled mini-ICAL detector is shown in Fig. 2.2 and also some important parameters are given in Tab. 2.1. Such an exact scale replica of the proposed ICAL has been constructed for the first time. The detailed discussion about the commissioning of mini-ICAL stack is given in Ref. [73].

The goals of mini-ICAL are many-fold. The main focus is of course the magnetic field variation, and compare the magnitude and direction of the measured field in the iron layers to results that have been obtained from MAGNET [74] simulation software. It is also a part of a feasibility study to test the cosmic muon veto for

Figure 2.2: Fully assembled mini-ICAL stack.

Parameters	Value (Mini-ICAL magnet)
Magnet size	$4\,\mathrm{m} \times 4\,\mathrm{m} \times 1.06\,\mathrm{m}$
Magnet weight	84 ton
Magnetic field uniformity	>1 T for 90 % area
No. of layers	11
Gap between two plates	45 mm
No. of copper coil/No. of turns in each coil	02/18
Induction (AT rating)	24,000 (nominal)
Conductor cross section (mm)	$30\times30\times$ ϕ 17 bore
Conductor material	Oxygen free copper
Coil cooling	Low conductivity DM water

Table 2.1: mini-ICAL magnet details.

shallow depths ICAL [75]. Once this is established, it will be possible to analyse the cosmic ray flux including this new feature. The associated electronics in the prototype stack enabled a determination of the direction of cosmic muon flux (both in zenith and azimuthal angles) but it had no sensitivity on momentum and only the integrated cosmic muon flux could be measured. Due to the presence of the magnetic field, it will now be possible to measure the momentum spectrum of the muon fluxes as well. The studies described in Chapters 4 and 5 for the RPC-only stack were also performed with the mini-ICAL set-up, in order to characterise the detector eficiciency, etc. Similar results and performance were observed here as well. Since the set-up was new, a great deal of trouble-shooting was required to understand and validate the electronics, etc. Some of these are listed in Appendix A.

However, no physics studies were performed with this data[1] and hence this is not discussed further in this thesis.

2.3 RPCs and their operation

The Resistive Plate Chamber (RPC) [76] is a parallel plate chamber like a spark chamber. Unlike spark chamber, the RPCs are made of very high resistive electrodes like glass or bakelite. The advantages of choosing the RPC as an active detector are, very good detection efficiency, good position resolution, fast response, large area coverage and very low cost. The RPC detector is made of two thin glass electrodes of thickness 3 mm separated by a gap of 2 mm between the glass electrodes. To maintain the uniformity of the gap between the glass plates 2 mm thick poly-carbonate buttons in the 8×8 matrix form are placed in between the glass plates. The regions where buttons spacers are placed is not efficient to detect the charged particle passes through the button. Those regions are dead regions in

[1] This was the subject matter of another thesis.

the RPC. The glass electrodes are sealed properly by the side spacers to make the RPC leak-proof. The outer side of the chamber is coated by a thin film of graphite to establish the differential high voltage ($\pm 5\,\mathrm{kV}$).

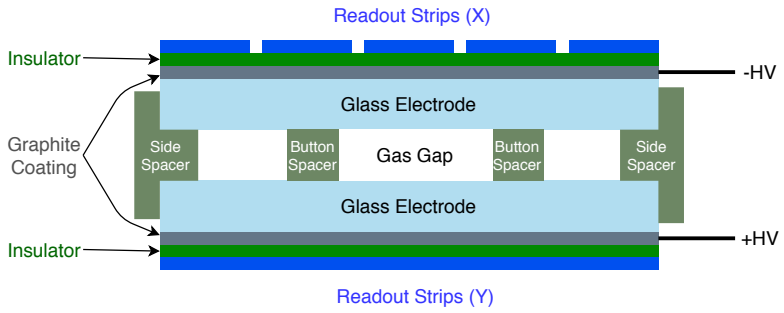

Figure 2.3: The graphical view of an RPC detector.

The suitable gas mixture for the RPC operation is circulated in a open loop system for the RPCs in RPC Only stack (in contrast to the closed loop system used for the mini-ICAL) through the gaps via gas inlet and outlet of the chambers. The main functions of the gas system are to mix the suitable gas with proper fraction, deliver the gas to the RPCs, receive the output gas from the RPCs. The indigenous developed gas recirculation system is used for the purpose. The individual gases from the cylinders are fed to the input of Mass Flow Controller (MFC), which are calibrated regularly. The output of three different MFCs are mixed in the storage cylinder and the output of the storage cylinder is allowed to pass through the gas manifold for the different RPCs in the stack. The total flow of the gas through all 12 RPCs is 60 cubic centimeters per minute (SCCM).

RPCs can be operated in avalanche mode or streamer mode. The streamer mode RPCs will give a larger signal where we don't need any preamplifiers. But the longevity of the RPCs was found to be very short in streamer mode operation. On the other hand, in avalanche mode operation, the signals produced in the RPCs are very small (order of mV), where we need low noise preamplifier before processing the signal. But the avalanche mode operation helps to run the RPCs for decades without a deterioration in the performance of RPCs. A suit-

able avalanche gas mixture consists of R134a:isobutane:SF_6 with a proportion of 95.2 %:4.5 %:0.3 % is chosen for RPC operation. The passage of muons through the gas gap ionises the gas mixture, and the free electrons produced in the primary ionisation are accelerated towards the anode, resulting in the production of avalanche multiplication.

The tiny signal is induced on the pickup panel due to the drift velocity of the electrons, which are produced in the avalanche process. The pickup panel is made of copper strips on one side of the panel with thin aluminium foil on the other side. The copper strips and aluminium sheet are placed on either side of the plastic honeycomb material. The pickup panels are placed both sides of the chamber. The panels are placed in such a way that the copper strips on both sides are orthogonal to each other. The orthogonal strips therefore give information of co-ordinates in two perpendicular direction of muon trajectory. The pickup panels used in the current study have 60 strips in the X-plane (bottom panel) and 63 strips in the Y-plane (top panel). The width of the copper strips is 2.8 cm and the interspace between strips is 0.2 cm. All assembled RPCs are placed in the stack made of aluminium support bars. The average distance between two consecutive RPCs in the stack is ~ 17 cm. The pickup panels are having the characteristic impedance of $\sim 50\,\Omega$. The subsequent electronics used to read a signal from these strips are also having input impedance almost equal to the characteristic impedance of the pickup panel. The graphical view of the RPC is shown in Fig. 2.3.

2.4 Electronics

The signals coming from the RPCs have to be further processed to store the information about the particle trajectory and its arrival time. The experiment was done in two phases. The electronics and data acquisition used for two phases are completely different. The first phase of the experiment was done using HMC pre-

amplifiers, Analog Front End (AFE), Digital Front End (DFE) board and VME-based Back End data acquisition. In Phase-II all the electronics used in the previous phase were replaced with sophisticated ASIC based NINO-charge sensitive Analog Front End board, FPGA based Digital Front End and network-based Back End. The electronics and DAQ used in phase-1 and phase-2 were developed by INO Collaboration. The further details of the Phase-1 and phase-2 electronics can be found from [73, 77, 78]. For the sake of completeness of this chapter, the electronics and DAQ used in phase-2 is briefly discussed here. This thesis discusses the physics results obtained from the phase-2. But, for the sake of completeness, the physics results from phase-1 will be summarised in one of the sub-sections in Chapter 5 (Results and discussion).

2.4.1 NINO Analog Front-End board

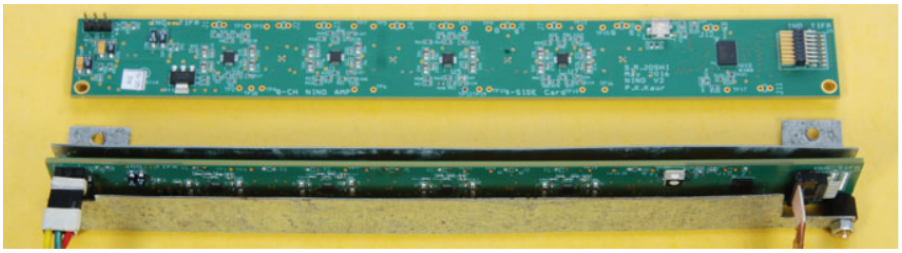

Figure 2.4: NINO board developed for RPC analog front-end.

As a part of the research program, the different front-end boards are developed to test the large area single gap RPCs. The major design constraints are, the preamplifier has to accept single-ended input signals, low power consumption, less noise, space consideration and suitable gain with a peaking time of 1 ns. NINO is an 8-channel front-end ASIC designed for time-of-flight detector in the ALICE experiment [79, 80]. NINO is an ultra-fast charge sensitive fast amplifier/discriminator with a peaking time of less than 1 ns. The NINO ASIC front-end board is shown in Fig. 2.4. The threshold of discriminator can be adjustable in the range of 10 fC to 100 fC. The width of the output signal depends on the charge of the input pulse.

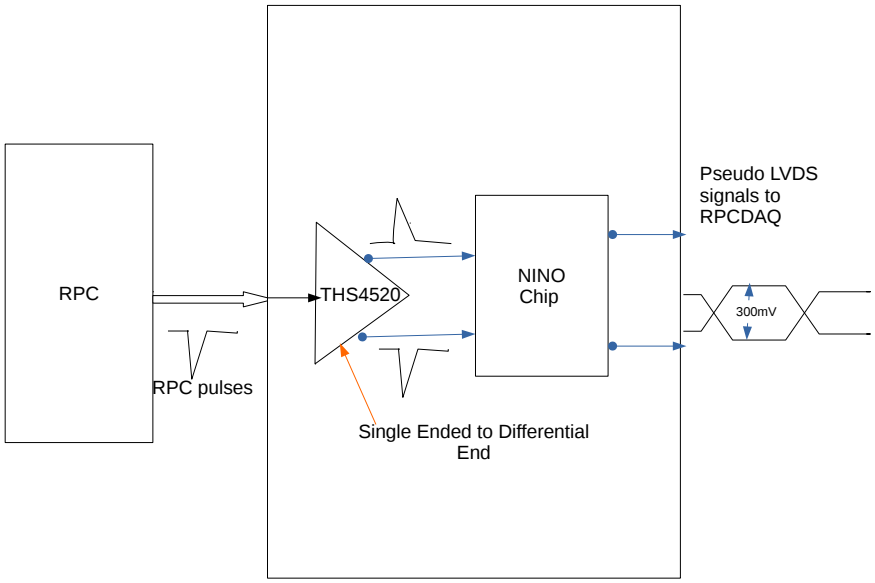

Figure 2.5: Shematic of NINO Front-End board.

The width of the output varies more in the lower range of input charge and variation is less for the higher range of input charge. NINO ASIC needs differential inputs. As shown in Fig. 2.5, the small analog pulses from RPCs are fed through the THS4520, which is a single-channel fully differential Op-Amps are used to make single-ended analog signals to differential analog signals. The differential analog signals are amplified and discriminated by NINO. The output of NINO is a pseudo-Low Voltage Diffirential Signal (LVDS) with a level difference of 300 mV. The power consumption of the designed board is ≈ 560 mW (excluding the loss in power supply regulator). NINO front-end boards are deployed in 11 layers out of 12 layers in the stack. The details about the NINO board development for INO are given in Ref. [81].

2.4.2 ANUSPARSH Analog Front-End board

ANUSPARSH front-end boards are developed indigenous by BARC (Bhabha Atomic Research Centre) electronics division [82]. It is ASIC based, 8-channel high speed, low noise voltage-sensitive amplifier/discriminator with a rise time of 1.2 ns, de-

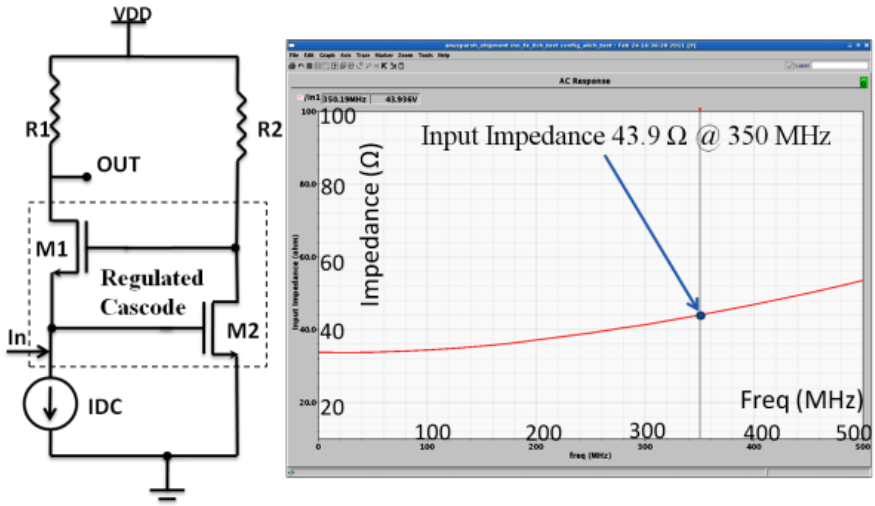

Figure 2.6: Simplified regulated cascode amplifier and simulated input impedance vs frequency (Figure is adapted from [82]).

signed for avalanche mode RPC detectors, which is one of the proposed front-ends in an INO-ICAL experiment. For the first time, Regulated cascode (RGC) trans-impedance pre-amplifier used as the frontend of RPC detector. The input impedance of the ANUSPARSH ASIC is matched with the input impedance of pickup strips. The shematic diagram of the simlified regulated cascode amplifier and its simulated response to the input frequency are shown in Fig. 2.6. The board is designed to take a small analog voltage signals from the RPCs and give an amplified pulse profile output to study the charge measurement as well as LVDS signals (The common mode range of 0.8 V to 1.6 V), which will go through the Digital front-end for further process. Power consumption per channel is around 45 mW at 3.3 V supply. The ANUSPARSH ASIC front-end board is shown in Fig. 2.7. To test the performance of ANUSPARSH boards, it was installed in the topmost layer in the RPC stack.

2.4.3 RPCDAQ Digital Front-End (DFE) board

The unshaped LVDS output from front-end boards is given as an input to the Digital Front-End board. RPC Data-AQuisition (RPCDAQ) board is a Field Pro-

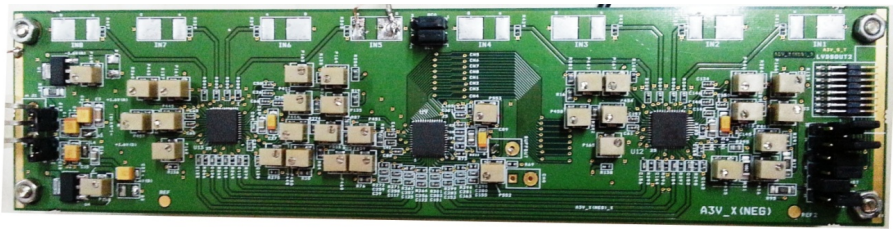

Figure 2.7: Anusparsh board developed for RPC analog front-end.

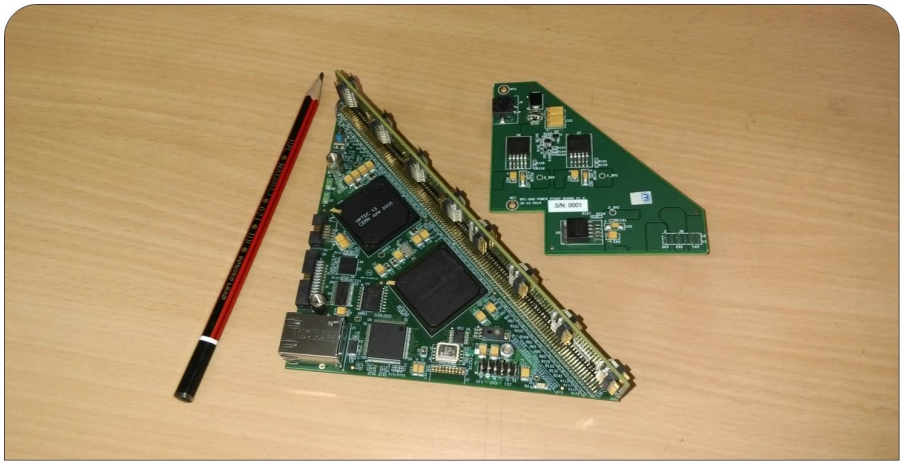

Figure 2.8: RPCDAQ board developed for RPC digital front-end.

grammable Gate Array (FPGA) based data acquisition system designed for INO-ICAL experiment [83] (shown in Fig 2.8). Each RPCDAQ board can take 128 input signals from front-end board, which are coming from 64 strips from X-plane and 64 strips from Y-plane. RPCDAQ board has many functional blocks such as rate monitor, pre-trigger generation, strip hit latch and Time to Digital Converter (TDC) to measure the relative arrival time of the muon in each layer with respect to the arrival of the trigger due to muon track. The RPCDAQ board is located at one corner of the RPC tray assembly. Most of the hardware are implemented inside the FPGA. A soft-core processor implemented in the FPGA is used to supervise the data acquisition, data collection and sending the data to the back-end servers through the network interface. The most important part of DFE is to measure the relative arrival time of muon in each layer with respect to the trigger. The current prototype of the DFE has HPTDC chip made by CERN with a resolution of 100 ps [84]. In future, the TDC module will be made by the INO collaboration and it will

be integrated into the DFE.

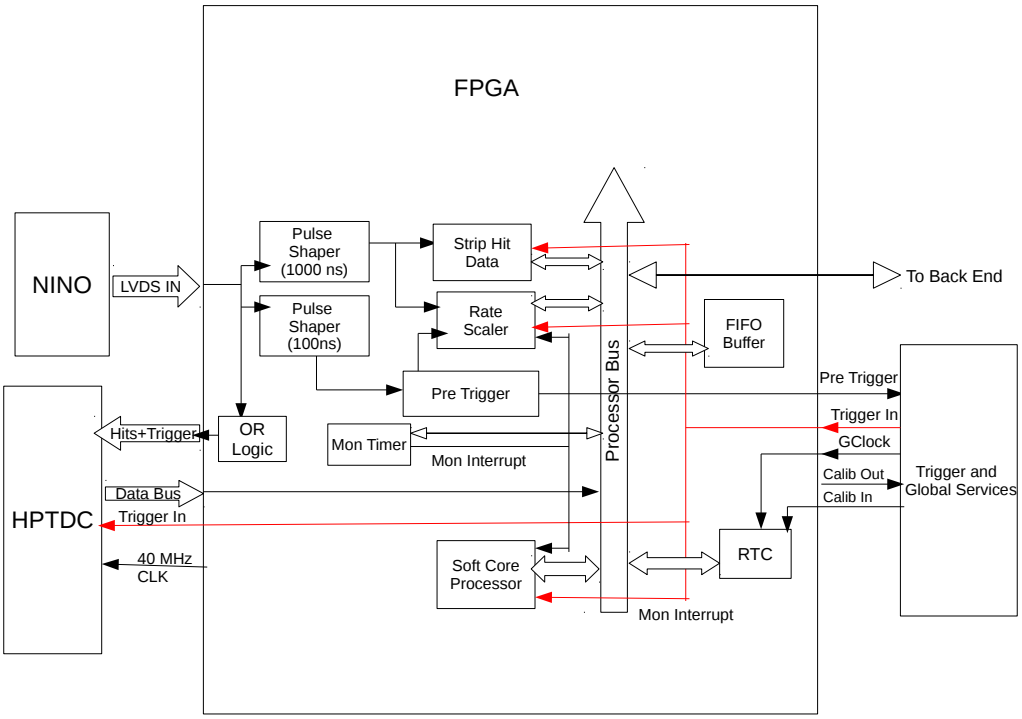

Figure 2.9: Block diagram of RPCDAQ digital front-end.

As shown in Fig. 2.9, the major functions of the DFE module are (a) latching the strip hit information (1 bit per strip), (b) monitoring the count rates of the RPC strips and (c) generation of trigger primitive signals. The induced pulses on the pickup strips due to the passage of muons in the RPC gap pass through the analog front-end. The DFE board receives unshaped LVDS signals from analog front-end. The DFE has two different pulse stretchers, one is for the strip hit latch and another is for trigger primitive signals. The global trigger will be generated by a global trigger module on the arrival of the trigger primitive signals from a different layer of DFEs. The global trigger is fanned out to the DFE from all layers. The strip hit information, event timestamp and muon arrival time in each layer are recorded and transferred to the backend server. A trigger veto is implemented in NIOS, which will be activated by the incoming trigger and blocks any further trigger from overwriting the latch before it is read out.

2.4.4 Trigger System

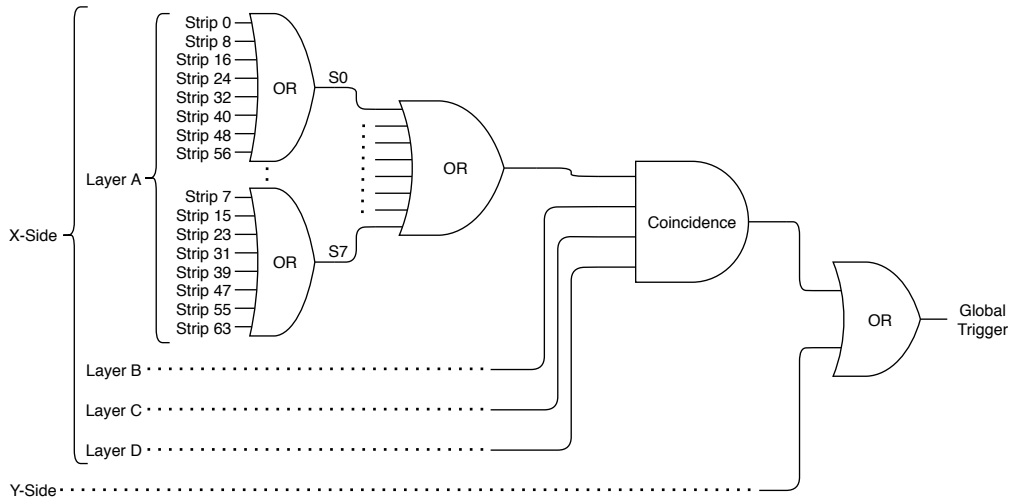

Figure 2.10: Shematics of Trigger generation for prototype ICAL [85].

The trigger system generates the global trigger based on event topology setting defined by the user. Trigger logic can be defined as m × p/n, where out of n consecutive layers there is a simultaneous signal in any p layers having signal in m channels [86]. The current trigger system has trigger options of 1F × 5/8, 2F × 4/8, 3F × 3/8, and 4F × 2/8 options as well as any fixed layer trigger (not more than five layers).

The individual signals from every 8^{th} strips (where the width of the discriminated signals are extended to 100 ns) are ORed to get pre-trigger signals[2] (S0 to S7). The four fold signals, namely the 1-fold[3], 2-fold[4], 3-fold[5] and 4-fold[6] are created by RPCDAQ which are passed to the Trigger system module in the back-end via Signal Router Board (Shown in Fig. 2.12). The pretrigger signals from the DFE will be transferred to the trigger system via Signal Router Board (SRB). The trigger system has multi-level trigger generation block (shown in Fig. 2.10). The

[2] S_i = CH_i + CH_{i+8} + CH_{i+16} + CH_{i+24} + CH_{i+32} + CH_{i+40} + CH_{i+48} + CH_{i+56} (CH_{i+j} represents the (i+j)th strip (i varies from 0 to 7) and "+" between two CH_{i+j} denotes logical "OR")

[3] 1F = S0+S1+S2+S3+S4+S5+S6+S7

[4] 2F = S0·S1+S1·S2+S2·S3+S3·S4+S4·S5+S5·S6+S6·S7

[5] 3F = S0·S1·S2+S1·S2·S3+S2·S3·S4+S3·S4·S5+S4·S5·S6+S5·S6·S7

[6] 4F = S0·S1·S2·S3+S1·S2·S3·S4+S2·S3·S4·S5+S3·S4·S5·S6+S4·S5·S6·S7 ("+" denotes logical "OR" and "·" denotes logical "AND")

pretrigger signals from the X-plane and Y-plane are fed to two trigger logic boards, TLBX and TLBY respectively. The coincidence of the trigger layers is done in both X- and Y- plane TLBs, then signals from TLB-X and TLB-Y are passed to Global Trigger Logic Module, where signals in TLBX and TLBY are ORed to form a final trigger. The entire control of the trigger system, monitoring of various signals rates

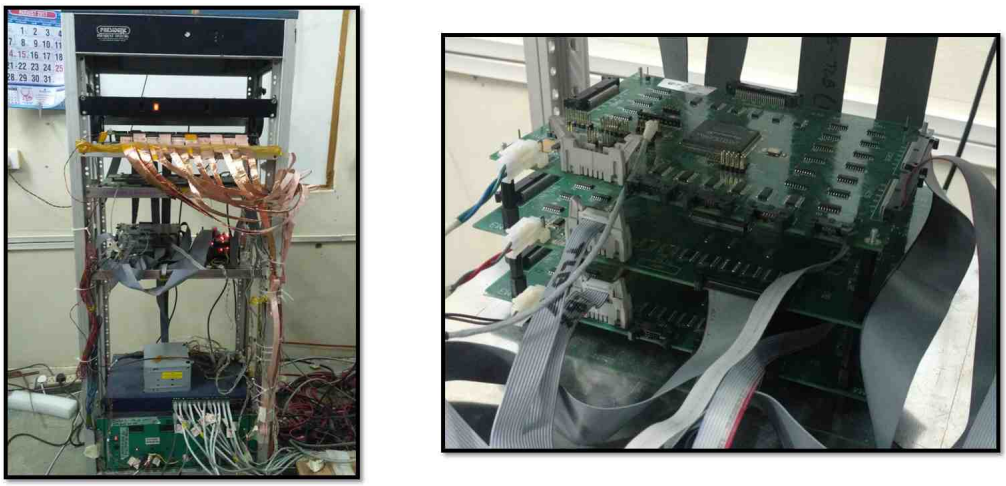

Figure 2.11: Trigger Logic Boards for prototype ICAL.

etc, are taken care of by Trigger Control and Monitor (TCAM) module. The interface between the trigger system and back-end data concentrator unit is handled by the Control and Monitor (CAM) module. The trigger generation boards are shown in Fig. 2.11.

2.4.5 Back-End Data Acquisition System

As is shown in Fig. 2.12, the back-end system has three major tasks, (*i*) Data concentrator, (*ii*) Event builder and (*iii*) Run control. Based on the arrival of the trigger signals in DFE, the event timestamp, the strip hit and timing data are packed in a packet and transferred into a buffer. The integral number of event data packets are sent to data concentrators at the back-end. The Real-Time Clocks (RTCs) of all the DFEs are pre-loaded with epoch time and synchronized up to a microsecond using Pulse-Per-Second (PPS) signal and global clock. The Data

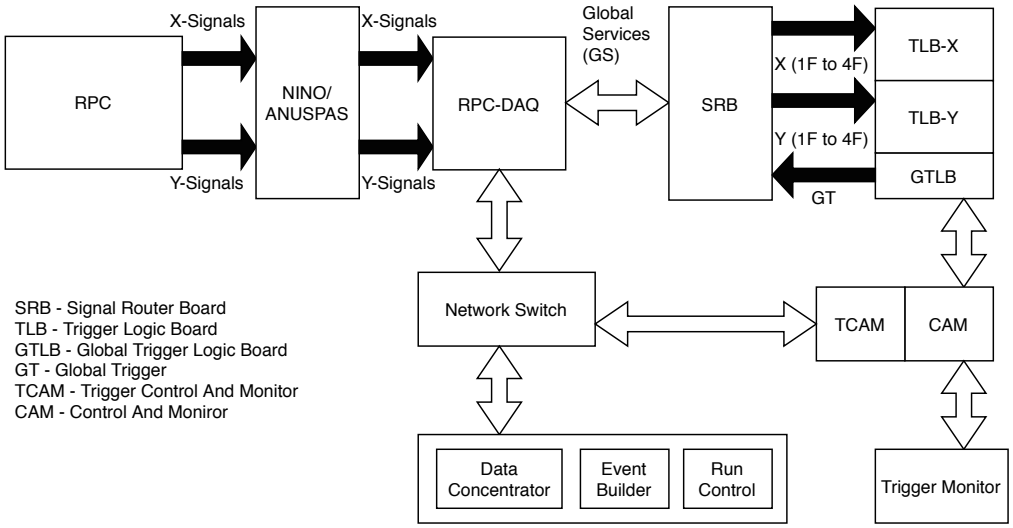

Figure 2.12: Signal flow from RPC to back-end in new electronics.

Concentrator in the back-end acts as a server and the DFEs acts as clients in terms of the network protocol. The Data Concentrator(s) gather the RPC data packets and attach an event number to each of the data packets belong to the event based on event timestamp comparison before transmitting the data to another server called Event-Builder. The events are built in the back-end using these RTC timestamps in the event builder.

Chapter 3

Experiment

3.1 Location of the Experimental site

The experiment commissioned to study the muon flux is located in IICHEP Transit Campus (9°56'N, 78°00'E and at an altitude of 160 m above mean sea level), Madurai, southern part of India. The location is unique in that it is located very close to geomagnetic equator (latitude is 1.44°N), where the effect of Earth's magnetic field plays dominant role in deciding the verticle rigidity for the primaries entering into the Earth's atmosphere. The horizontal intensity of the magnetic field component around the Earth is shown in Fig. 3.1. The muon flux varies with latitude, longitude and altitude on the Earth. The vertical rigidity of the present experimental site is ~ 17 GeV, which will cause reduction in the observed muon flux in comparison with high latitude observation. The vertical cut off rigidity at a particular geographic latitude varies with time due to the variation of the magnetospheric and geomagnetic field.

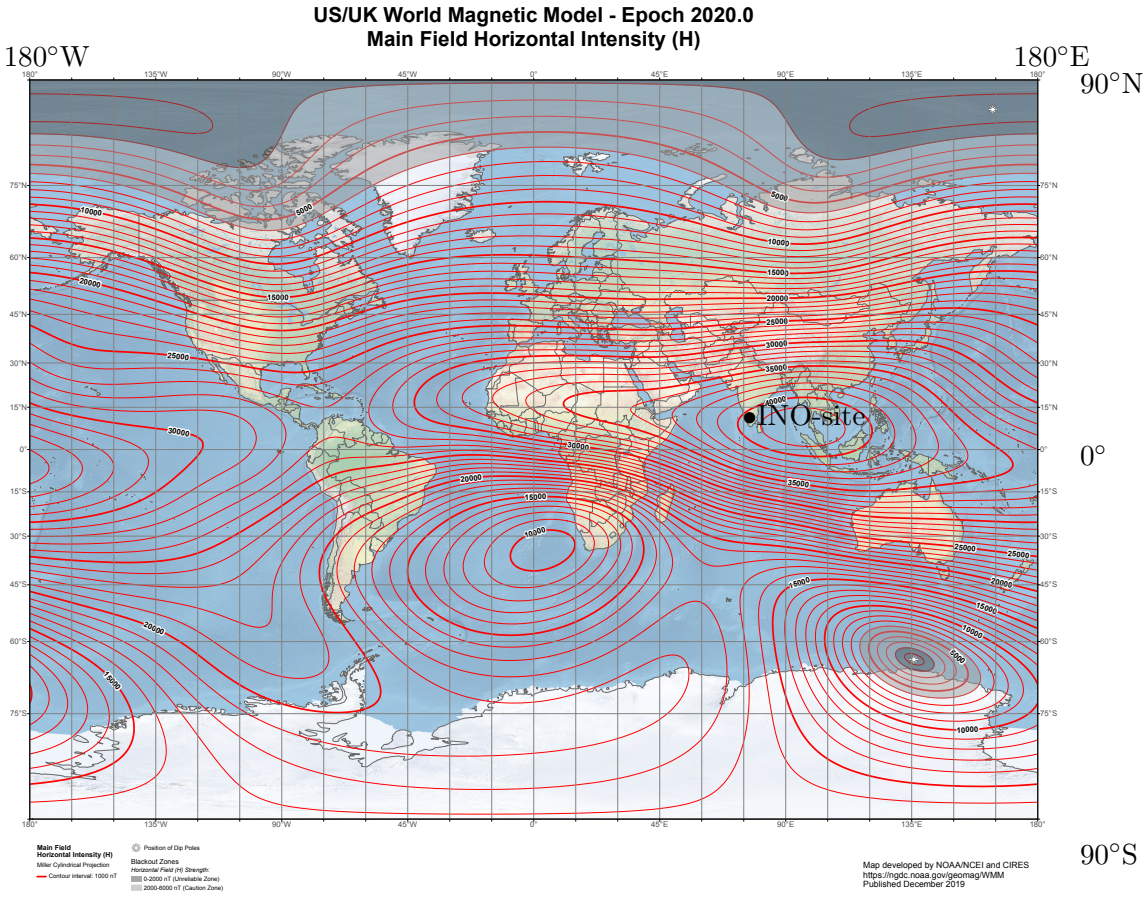

Figure 3.1: Horizontal component (in nT) of Earth's magnetic field around the globe [87].

3.2 Observation Period

The data taking was done in two phases with two different electronics and DAQ. The data collected from phase-1 was used to measure the shape of zenith angular distribution (n-exponent) and integral intensity of vertical muons (I_0). The details about these parameters(n and I_0) and the comparison of the observed results with different locations on the Earth are discussed breifly in Chapter 5. The second phase of the experiment was done using upgraded electronics, which are discussed in Chapter 2. The data collected from phase-2 was used to measure the azimuthal dependent muon flux in different zenith angle bins. The present thesis mainly discusses physics results obtained during the phase-2 of the experiment.

3.2.1 Period of Phase-1

First phase of the experiment was commissioned and data taking was started in August, 2015 and operated till April, 2017. At very beginning the detector stack was used to characterise the RPCs and electronics after trouble-shooting. The data recorded in a specific period with a perfect detector condition used to do physics analysis. The data chosen for the physics study is between 24 August, 2016 to 27 August, 2016. The hardware trigger layers used to record this data are layer 1,2,9 and 10 (only X-plane). The magnetospheric changes and solar modulation

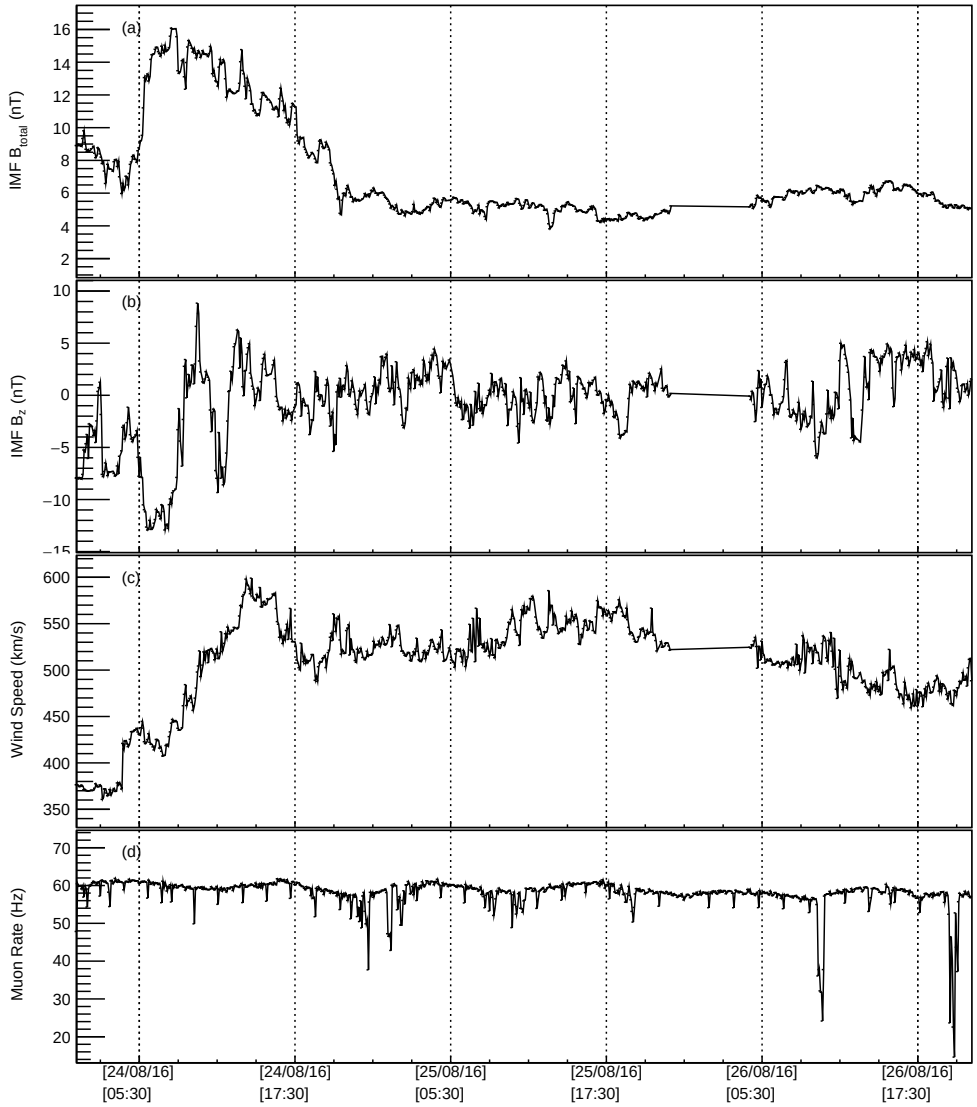

Figure 3.2: (a), (b) and (c)are scalar magnetic field, Z-component (B_z) and wind speed (km/s) IMF from Wind data respectively. (d) is the muon rate for the obervation period during phase-1

may affect the muon flux minimally for a given location on the Earth. The WIND data for changes in Inter-planetry Magnetic Field (IMF scalar as well as B_z) and solar wind velocity (km/s) for the data taking period taken from OMNIWeb [88] website (shown in Fig. 3.2(a), (b) and (c)). From scalar field and B_z values, it can be inferred that there is a minor fluctuations in the IMF field on 24^{th} August. The earth magnetosphere in the locations between mid-latitude to pole will get affected by minor storm. The present site will not have much effect due to this. The muon rate (Hz) from the observation period doesn't have effect during the minor IMF fluctuation (shown in 3.2(d)).

3.2.2 Period of Phase-2

Second phase of the experiment was operated between June, 2017 to March, 2018. Studies related to varios aspects were performed with this upgraded electronics. The good quality data recorded from 23 August 2017 to 28 August 2017. Within this period the detector conditions found to good with less noisy strips and stable electronics. The trigger condition used to record the data from phase-2 is from coincidence of 1 fold signals from layer 4, 5, 6 and 7 (X- or Y-plane). The OMNIWeb data for the data taking period shows there is no significant change in the IMF and solar wind speed (shown in Fig. 3.3(a), (b) and (c)). So it indicates less solar activity during this period. The muon rate for this observation period is shown in Fig. 3.3(d). This data would be good to study the muon flux.

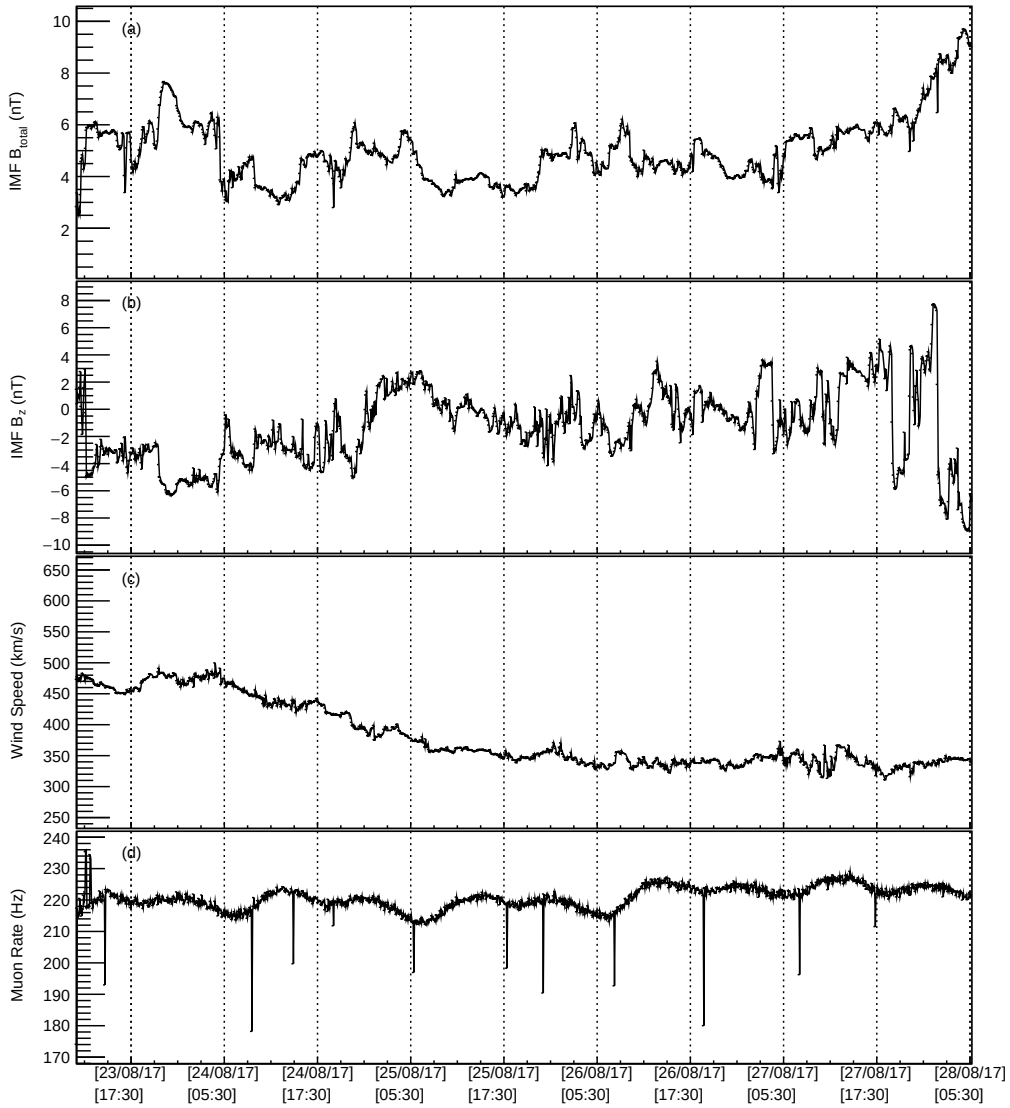

Figure 3.3: (a), (b) and (c)are scalar magnetic field, Z-component (B_z) and wind speed (km/s) IMF from Wind data respectively. (d) is the muon rate for the obervation period during phase-2

Chapter 4

Data Analysis and Monte-Carlo Study

4.1 Event Selection

The event data is recorded based on hardware trigger from four fixed trigger layers (namely, 4, 5, 6 and 7 (X- or Y-plane). The data obtained from the experiment is later analysed offline to study the performance of the RPC detectors. Event filtering is the first and foremost thing to do before reconstructing the track. The passage of charged particle through the RPC induces a signal on pick up strips. The avalanche size created inside the gap will cover the area of $0.1\,\mathrm{cm}^2$. The induced signals are mostly expected in one or two strips above the interaction point. The average strip multiplicity observed from data is around 1.3 strips. Out of total triggered events, on an average the fraction of events with one, two and three strip multiplicity are $40\,\%$, $30\,\%$, and $10\,\%$ respectively. In the remaining fraction, more than $18\,\%$ comes from inefficiency and less than $2\,\%$ is from the shower events, streamer and electronics noise. Due to the trigger acceptance, the outer layers are having more zero hit fraction than middle layers.

The strip multiplicity of more than three is observed in data mostly due to

hadronic shower, streamer, correlated electronics noise and random noise. The peak in large multiplicity are due to correlated electronics noise. The zero hit multiplicity is due to either the inefficiency of the detector or acceptance. The recorded events based on trigger may have muons, hadrons, the shower of particles and noise along with muon track. The noise due to the shower of particles, correlated electronic noise and large streamer will affect the reconstruction of clear tracks. The typical muon and hadron event are shown in Fig. 4.1.

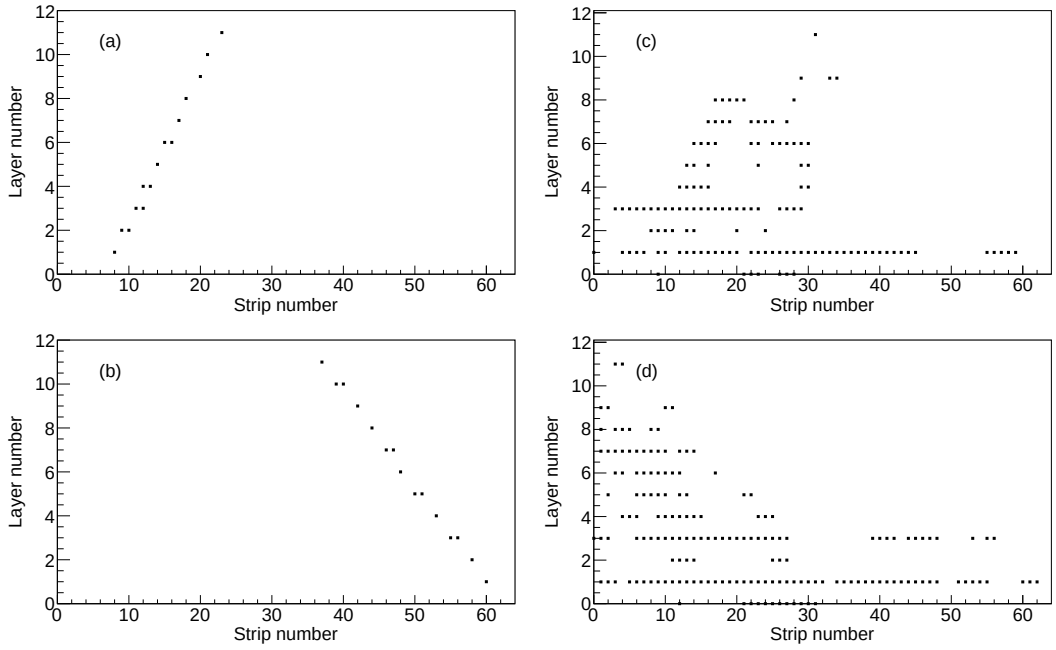

Figure 4.1: (a,b) Typical muon trajectory and (c,d) hadronic shower in RPC stack. (a,c) are XZ views and (b,d) are YZ views.

For the purpose of characterisation of RPCs and physics study, the events triggered by single muon events need to be isolated. The algorithm to filter the muon hits are explained as,

- The hit multiplicity due to passage of muon through the RPC is upto three strip.

- Multi-tracks, hadron shower and random noise gives a number of hits, which may not be consecutive.

- To select the single muon events for further analysis, the events with hadronic shower or a layer with larger strip multiplicity, due to streamer and noise hits are avoided by accepting only layers having at most hits in consecutive three strips.

4.2 Muon Track Reconstruction

The arithmetic mean position of the hits for the selected layers are calculated and the data is fitted using straight line in both XZ- and YZ-plane.

$$x(/y) = \alpha \times z + \beta \ , \tag{4.1}$$

where x or y is the hit position from the X- or Y-plane respectively for Z^{th} layer, α is the slope which is $\tan\theta\cos\phi$ ($\tan\theta\sin\phi$) for XZ (YZ) plane and β is the intercept. These four parameters are used to get a trajectory position of the muon in XZ and YZ view.

Least square method used to fit the straight line. The fitting procedure explained in this section are discussed from Ref. [89]. The data consist of n points (z_i, $x_i \pm \sigma_i$) in X-plane or (z_i, $y_i \pm \sigma_i$) in Y-plane. The error σ_i of x_i and y_i are calculated from RMS values of the position residual distribution.

$$\chi^2 = \sum_{i=1}^{n=12} \left(\frac{x_i - \alpha z_i - \beta}{\sigma_i^2} \right)^2 \ . \tag{4.2}$$

Differentiating the Eqn. 4.2 with respect to parameter α and β gives the Eqns. 4.3 and 4.4.

$$-\frac{1}{2}\frac{\partial\chi^2}{\partial\beta} = \sum \frac{x_i - \alpha z_i - \beta}{\sigma_i^2} = 0 \ ; \tag{4.3}$$

and

$$-\frac{1}{2}\frac{\partial\chi^2}{\partial\alpha} = \sum \frac{z_i(x_i - \alpha z_i - \beta)}{\sigma_i^2} = 0 \ . \tag{4.4}$$

Solving the above two simultaneous equations for our two unknowns, which yields Eqn. 4.5.

$$\alpha = \frac{[1][zx] - [z][x]}{[1][z^2] - [z][z]} \ , \tag{4.5}$$

where the quantities in square brackets are defined as,

$$[f] = \frac{1}{n} \sum \frac{f_i}{\sigma_i^2} \ . \tag{4.6}$$

Now the weighted means of the same quantities are given by

$$\langle \, f \, \rangle = [f]/[1] \ . \tag{4.7}$$

The parameter β can be determined by rewriting the Eqn. 4.1 as,

$$\langle \, x \, \rangle (or \langle \, y \, \rangle) = \alpha \langle \, z \, \rangle + \beta \ . \tag{4.8}$$

Thus far the parameters are estimated; next the error on these parameters can be obtained from $\partial^2 \chi^2 / \partial p_i \partial p_j$. The calculated inverse error matrix from 4.3 and 4.4 is given as,

$$n \begin{pmatrix} [1] & [z] \\ [z] & [z^2] \end{pmatrix} . \tag{4.9}$$

The error matrix after inversion is,

$$\frac{1}{nD} \begin{pmatrix} [z^2] & -[z] \\ -[z] & [1] \end{pmatrix} , \tag{4.10}$$

where D is the determinant,

$$D = [z^2][1] - [z][z] \ . \tag{4.11}$$

Hence the error matrix for the slope and intercept is obtained. The estimation

error on the x can be calculated from Eqn. 4.12.

$$\sigma_x^2 = z^2\sigma_\alpha^2 + 2z\,\mathrm{cov}(\beta,\alpha) + \sigma_\beta^2 \ . \tag{4.12}$$

The distribution of χ^2/ndf, number of layers and the probability distribution for the fitted trajectories are shown in Fig. 4.2.

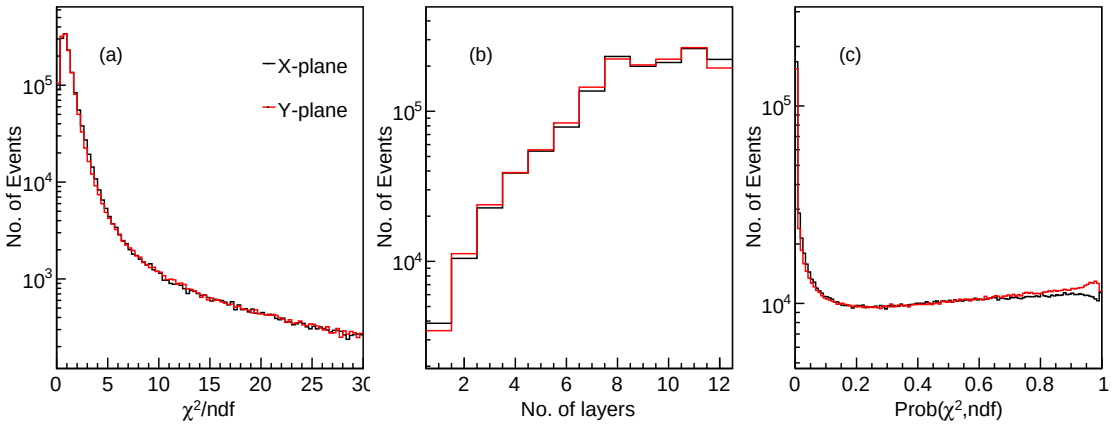

Figure 4.2: (a), (b) and (c) are the distribution of χ^2/ndf, number of layer hits and Prob(χ^2,ndf) for (black) X- and (red) Y-planes.

After doing a fit, if the position residue (difference in fit point and observed position) of a hit is more than 2 strip width from the fit point the fit is redone by removing that hit. Bias in the fit due to outliers are eliminated from this cut. If a fit has less than 3 data points, the fit parameters are not estimated for these events and will not be considered for further analysis.

4.3 Position residues and Strip multiplicity

4.3.1 Offline Alignment Correction

All the RPC layers are aligned manually, there may be a possibility of misalignment in the physical placement. The relative shift in the RPC detectors between different layers will cause improper estimate of fit parameters. In order to get the precise trajectory informations, the relative shift in the RPC layers are estimated using the

muon data offline using an iterative method. In the iterative method, a layer under study is removed from the fit and fit parameters are estimated using data from the other layers. The distribution of the observed hit position and extrapolated position using other layers are fitted by Gaussian function. Ideally, the mean of the fitted Gaussian is expected to be zero. But the improper physical alignment gives the non-zero mean, which is considered as position offset of that RPC layer. Similarly, position correction for all the RPCs are calculated using this method. The efficiency, inefficiency, position residues, time resolution, etc of each layer are calculated after incorporating the position corrections. After four to five iterations, the precision of the detector position is better than 0.2 mm. The distribution of position residues for layer-9 before and after position corrections, fitted mean and σ of the position residues at different layers with iteration are shown in the Figs. 4.3 and 4.4 respectively.

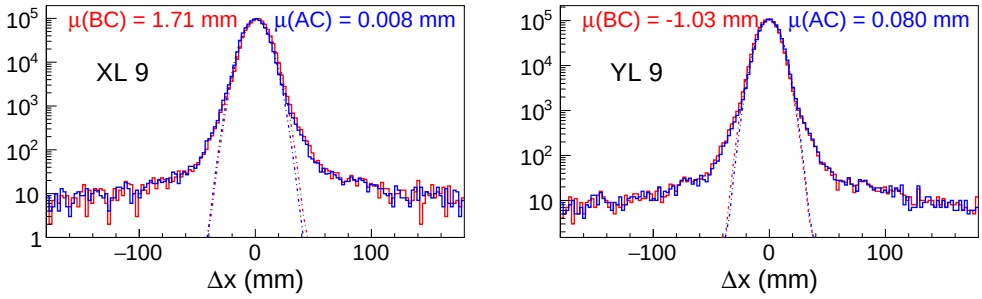

Figure 4.3: The position residues for X- (left) and Y- (right) planes of layer-9 before (red) and after correction (blue).

4.3.2 Position dependent strip multiplicity

Since the pitch of the pickup strips is 3 cm, wherever muon passes through the strip, the induced signal will be in the one, two or three strips around the position where the muon passes through. The probability of different strip multiplicity predominantly depends on the position of muon as it passes through in a strip. If muon passes through the middle of the strip, the probability of getting multiplicity

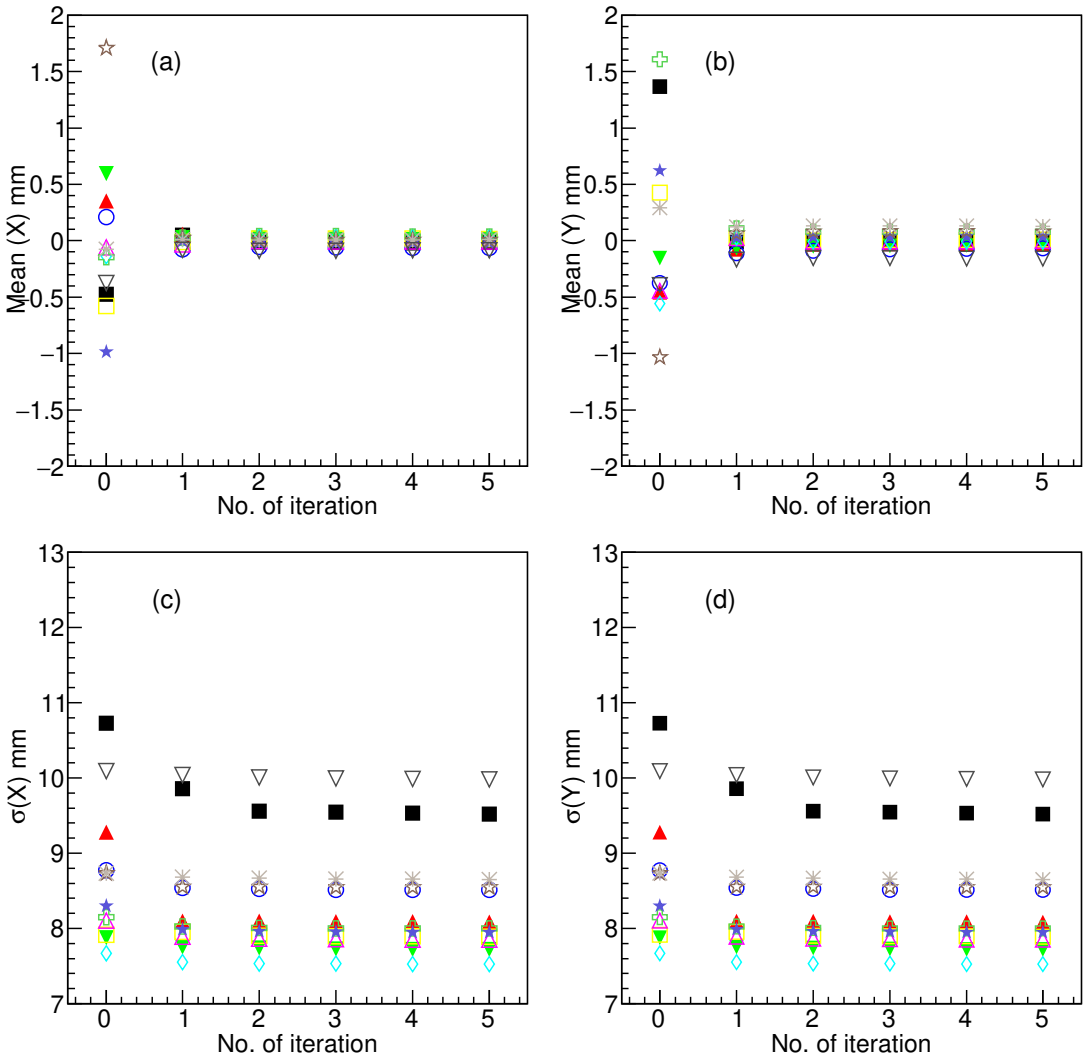

Figure 4.4: The variation in the fitted mean ((a) and (b) for X- and Y-plane respectively) and σ ((c), (d) for X- and Y-plane respectively) of the position residues for different iteration.

one is more than multiplicity two. The probability of having multiplicity two increases if the muon passes through the middle of two strips because of the sharing of the same signal induced by the avalanche. Strip multiplicity three has a Gaussian distribution with large spread centered at middle of the strip. The probability of having more than three strip hits are more are less uniform throughout the strip. The position-dependent multiplicity for X- and Y-plane for all RPCs are shown in Figs. 4.5 and 4.6 respectively. These distributions matched our naive expectation and also symmetry of the distributions confirm the alignment of those RPC layers.

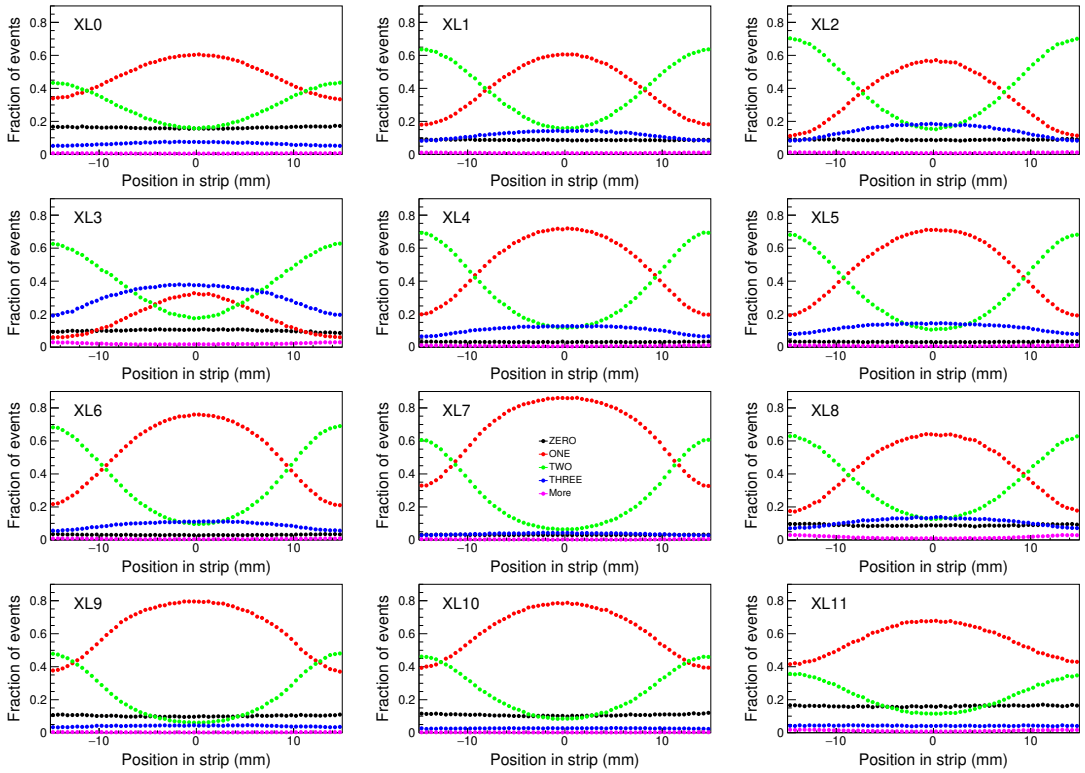

Figure 4.5: Position dependent strip multiplicity for all 12 layers in the X-plane.

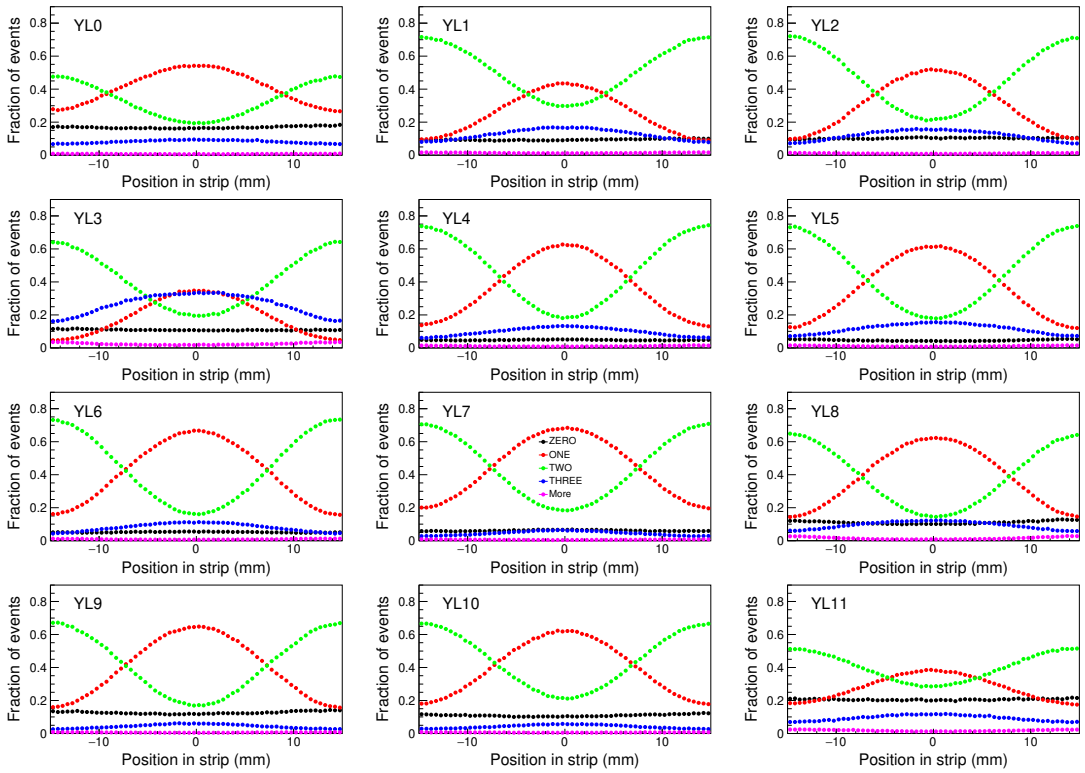

Figure 4.6: Position dependent strip multiplicity for all 12 layers in the Y-plane.

4.3.3 Multiplicity dependent position residues

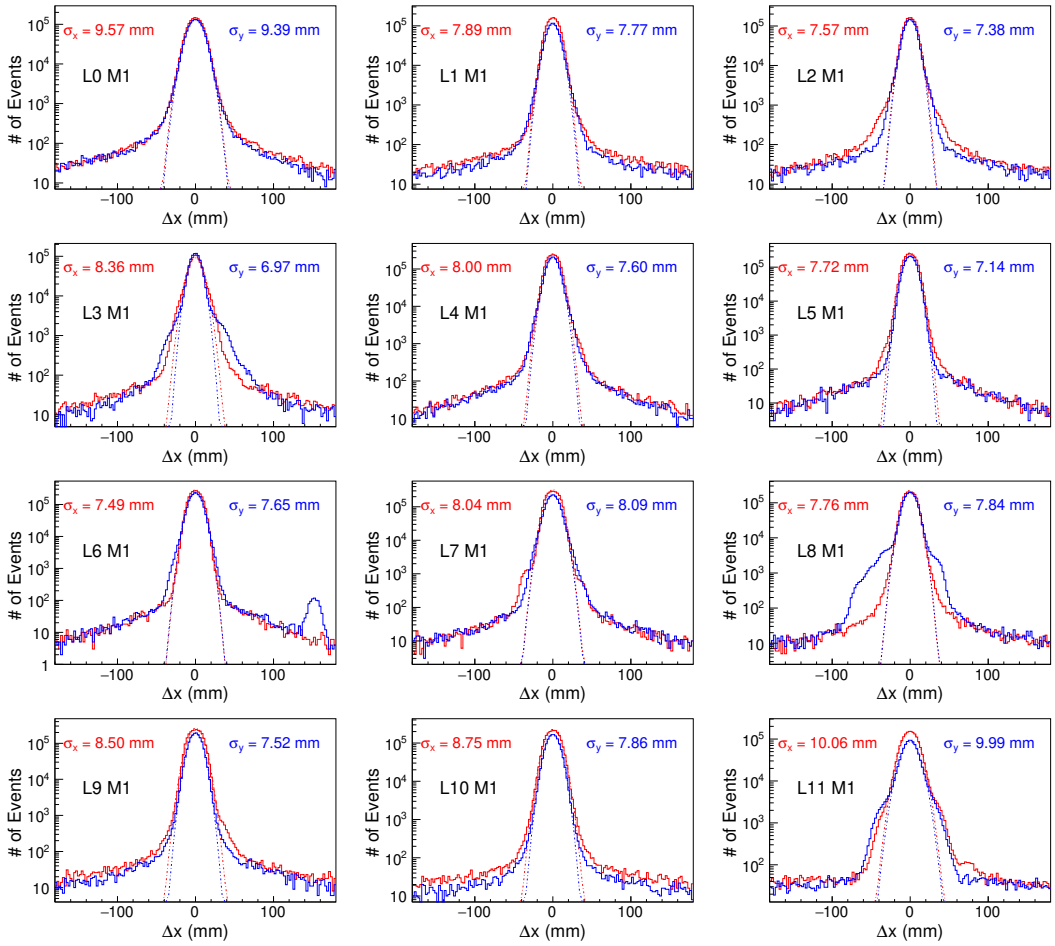

Figure 4.7: The position residues distribution for events having strip multiplicity one for all 12 layers for the (blue)X- and (red)Y- plane.

The observed position residues for strip multiplicities of one, two, three and four are shown in Figs. 4.7, 4.8, 4.9 and 4.10 respectively. The position residue distribution is fitted with Gaussian function and the fitted σ is taken as a position resolution. The position resolution of the RPC is found to be less than 10 mm for events with multiplicity one, two and three. The position resolution of the RPCs using the events with strip multiplicity four is order of the strip width due to poor localisation of the observed hit in the RPC. The observed position resolution is a combination of the true resolution of RPC and extrapolation error. The observed position resolution, extrapolation error and corrected position resolution

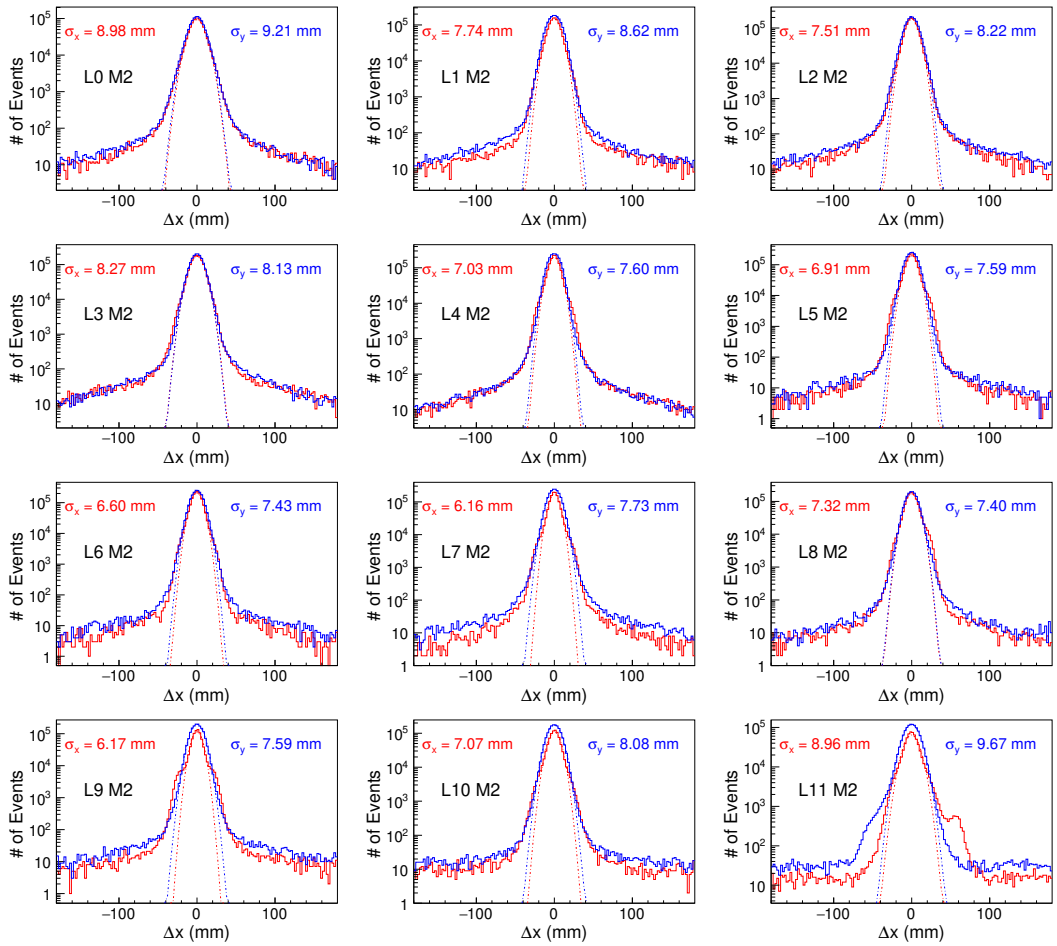

Figure 4.8: As in Fig. 4.7 for events with strip multiplicity two.

($\sigma_{true} = \sqrt{\sigma^2_{observed} - \sigma^2_{extrapolated}}$) are listed in Tables 4.1 and 4.2 for X- and Y-plane respectively. As expected the extrapolation error is larger for outer layers. The position resolution with strip multiplicity four shows larger value, which implies that most of those signals are due to streamer pulse and cause poor localization. Due to the poor localization, the analysis is performed based on the events having strip multiplicity of up to three.

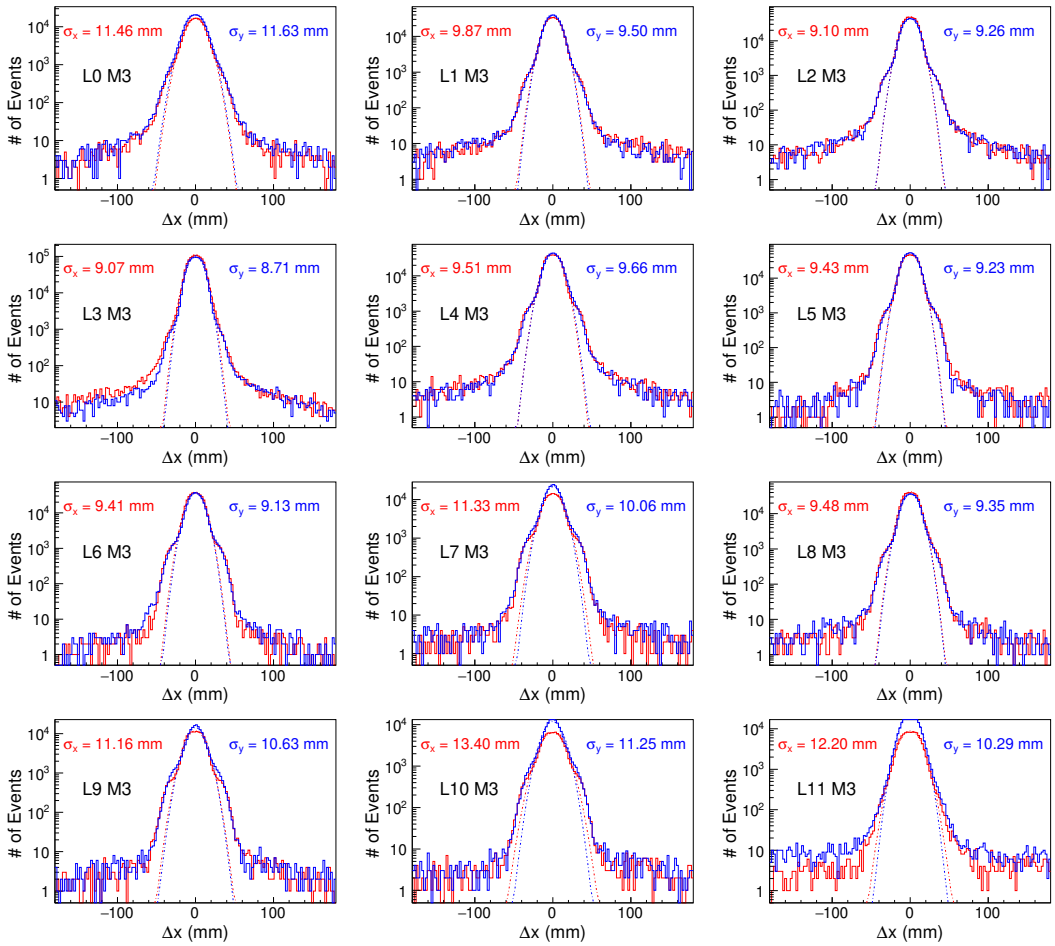

Figure 4.9: As in Fig. 4.7 for events with strip multiplicity three.

Layer No	$\sigma_{extrapolated}$ (mm)	$\sigma_{observed}$ (mm)				σ_{true} (mm)			
		M1	M2	M3	M4	M1	M2	M3	M4
0	5.06	9.57	8.98	11.5	23.4	8.12	7.41	10.3	22.9
1	4.41	7.89	7.74	9.87	23.4	6.54	6.36	8.83	23
2	3.84	7.57	7.51	9.1	23.1	6.52	6.45	8.25	22.8
3	3.31	8.36	8.27	9.07	19.6	7.68	7.58	8.44	19.3
4	3.23	8	7.03	9.51	24	7.32	6.24	8.94	23.8
5	2.8	7.72	6.91	9.43	22.9	7.19	6.31	9	22.7
6	2.79	7.49	6.6	9.41	23.4	6.95	5.98	8.99	23.2
7	3.15	8.04	6.16	11.3	24.8	7.4	5.29	10.9	24.6
8	3.37	7.76	7.32	9.48	18.3	6.98	6.5	8.86	18
9	3.8	8.5	6.17	11.2	25.5	7.61	4.87	10.5	25.2
10	4.52	8.75	7.07	13.4	27.1	7.49	5.43	12.6	26.8
11	4.96	10.1	8.96	12.2	21.5	8.76	7.46	11.2	21

Table 4.1: The position resolution for different strip multiplicity (X-plane) for all 12 layers before and after correction for extrapolated error.

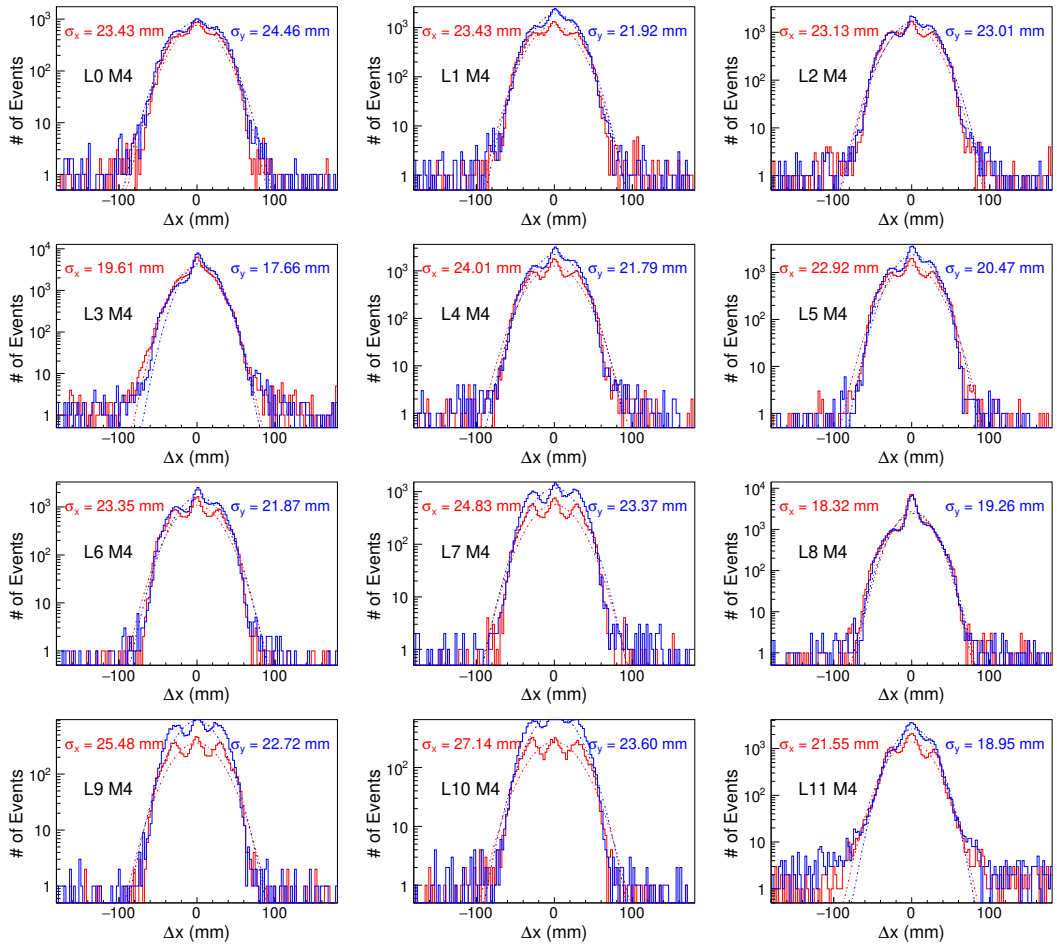

Figure 4.10: As in Fig. 4.7 for events with strip multiplicity four.

Layer No	$\sigma_{extrapolated}$ (mm)	$\sigma_{observed}$ (mm)				σ_{true} (mm)			
		M1	M2	M3	M4	M1	M2	M3	M4
0	5.21	9.39	9.21	11.6	24.5	7.81	7.59	10.4	23.9
1	4.44	7.77	8.62	9.5	21.9	6.37	7.39	8.4	21.5
2	3.84	7.38	8.22	9.26	23	6.31	7.27	8.42	22.7
3	3.4	6.97	8.13	8.71	17.7	6.09	7.38	8.02	17.3
4	3.23	7.6	7.6	9.66	21.8	6.88	6.88	9.1	21.6
5	2.85	7.14	7.59	9.23	20.5	6.54	7.03	8.77	20.3
6	2.82	7.65	7.43	9.13	21.9	7.11	6.87	8.68	21.7
7	3.16	8.09	7.73	10.1	23.4	7.45	7.05	9.55	23.2
8	3.38	7.84	7.4	9.35	19.3	7.07	6.58	8.72	19
9	3.83	7.52	7.59	10.6	22.7	6.47	6.55	9.92	22.4
10	4.55	7.86	8.08	11.2	23.6	6.41	6.68	10.3	23.2
11	4.94	9.99	9.67	10.3	19	8.68	8.31	9.03	18.3

Table 4.2: As in Table 4.1 for Y-plane.

4.4 Monitoring of the Detector Using Data

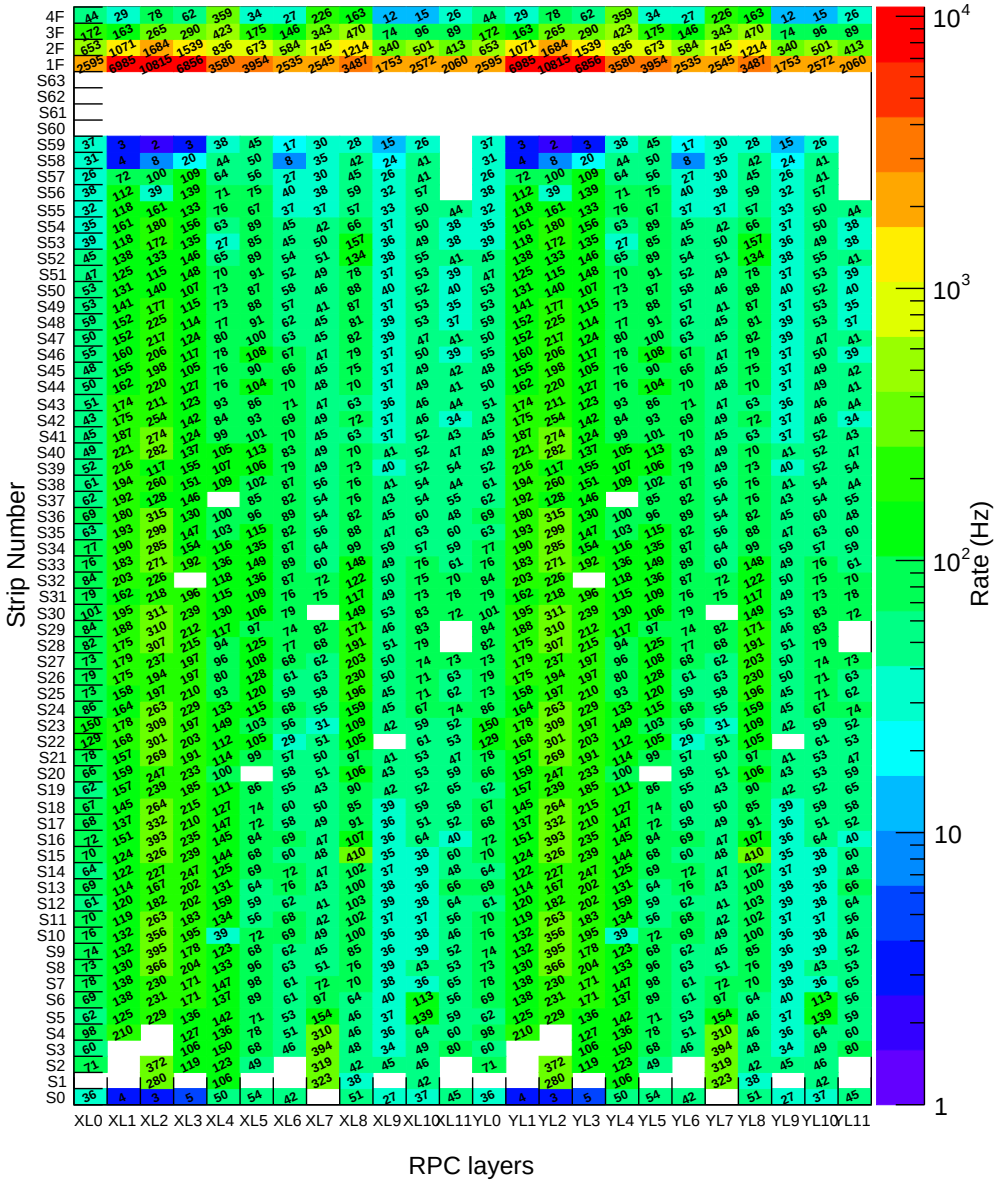

Figure 4.11: Average Noise rate for individual strips in RPC Stack.

The first and foremost thing is to observe the quality of the data collected by experiment. Noise rate of each strip is very crucial to study the health of that strip as well as an RPC. A typical Noise rate plot is shown in Fig. 4.11. Also, the variation in the noise rate, atmospheric pressure, temperature and relative humidity as a function of time is shown in Fig. 4.12. The strip occupancy and strip multiplicity can be used to study the behaviour of RPC detector. The occupancy

of each strip is calculated by taking the ratio of number of events in which the strip is fired to the total triggered events. The strip occupancies are used to identify the noisy strips, as well as dead strip and problematic strips. The percentage of strip occupancy for X- and Y-plane along with comparison of MC simulated events for all the layers are shown in Figs. 4.19 and 4.20 respectively. The shape of the strip occupancy shows the strips at the middle of the detector have more probability of getting fired by muon events due to the solid angle acceptance of the trigger conditions. The events which pass through the middle of the detector had a higher acceptance rate compared to the events passing through the edge of the detectors.

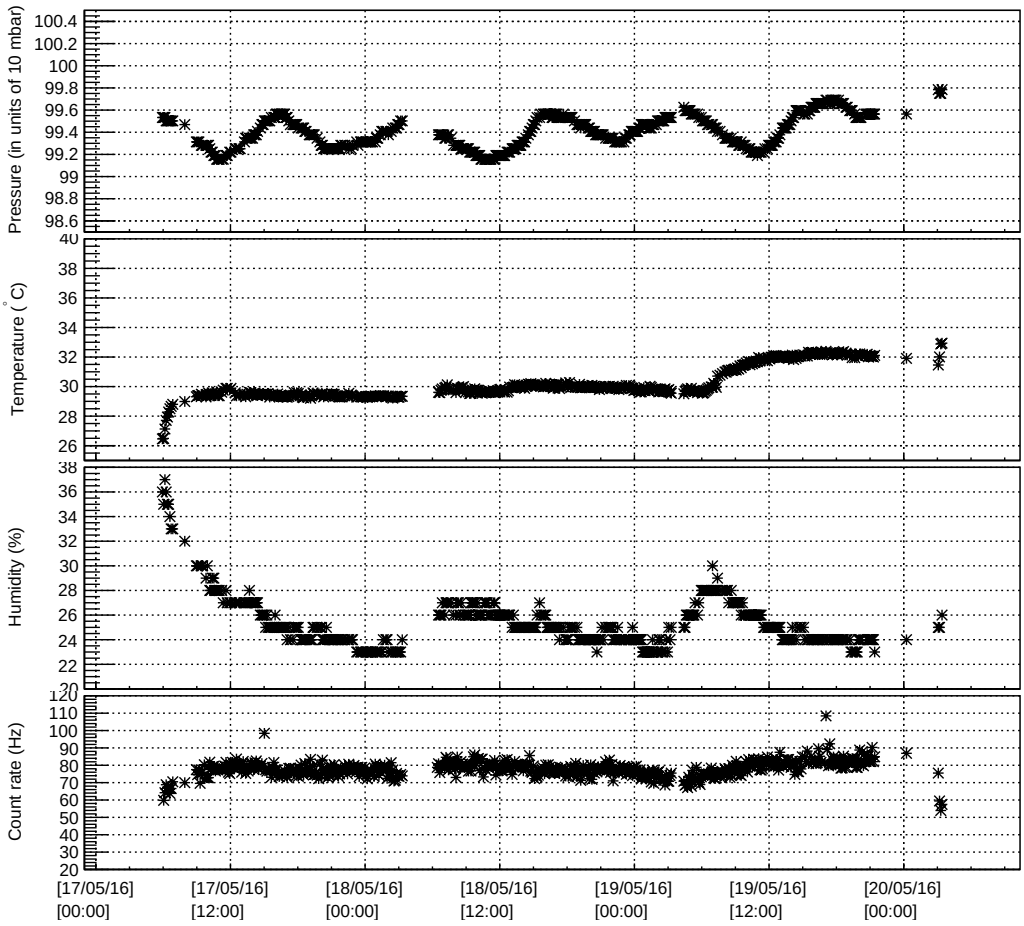

Figure 4.12: The variation in the ambient pressure, temperature, relative humidity and count rate for the RPC over 3 days.

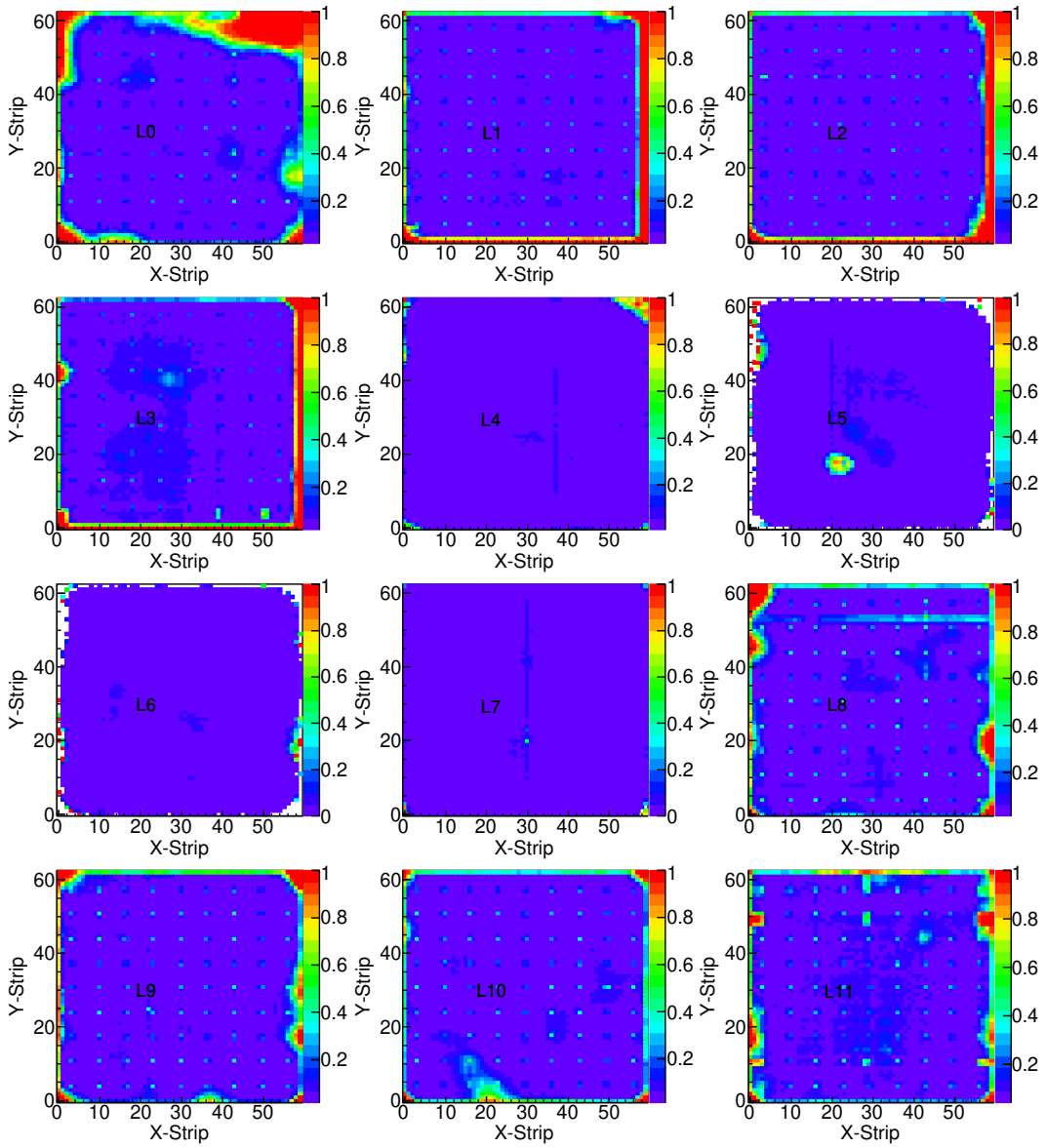

Figure 4.13: Correlated inefficiency map for all 12 layers.

4.4.1 Efficiencies

The efficiency of the RPC detector is calculated using muon data. The fitted events with hits in at least 4 layers and fitted χ^2/ndf less than 2 are considered for the efficiency calculation. The hit inefficiencies and trigger efficiencies are calculated for each 3 cm $\times$ 3 cm pixel, to match with strip width. The algorithm to calculate the pixel-wise hit inefficiencies and trigger efficiencies is as follows. The extrapolation error (ϵ) on the hit points in a layer is estimated. The deviation (δ) of a fit point

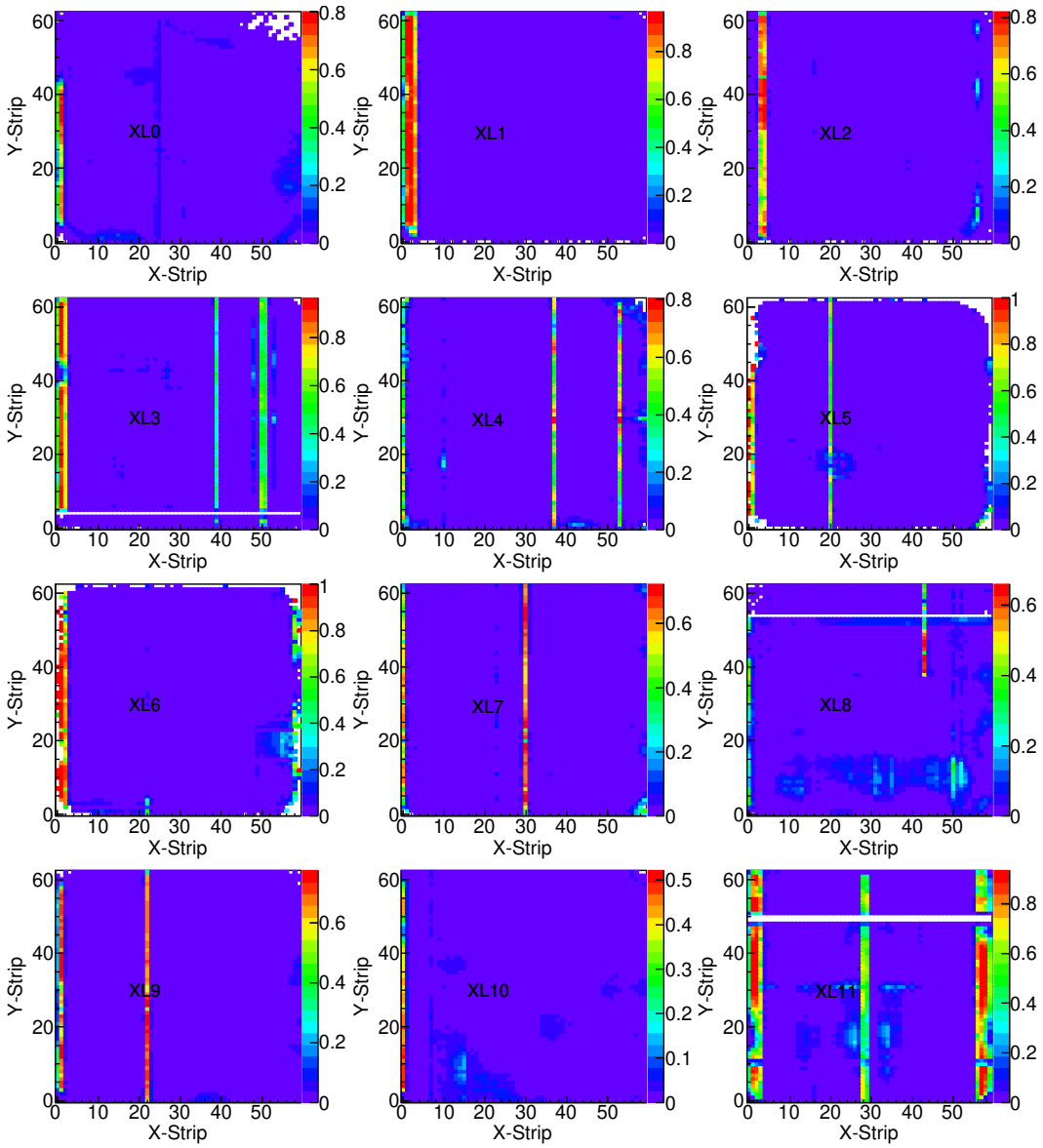

Figure 4.14: Uncorrelated inefficiency map for all 12 layers for the X-plane.

from the midpoint of a strip is also calculated. The trajectories, where $|\delta| + \epsilon$ is within a strip pitch only are considered for the efficiency measurement. The total number of events passing through a pixel is calculated using the extrapolated position in that pixel. The correlated inefficiencies are estimated using the ratio of events when a fitted muon passes through a pixel, but there is no hit in that position in both the X- and Y-plane of the detector within 3 cm of the extrapolated point, to the total number of events. The correlated inefficiencies for all RPCs are shown in Fig. 4.13. The problem related to gain variation due to the non-uniform

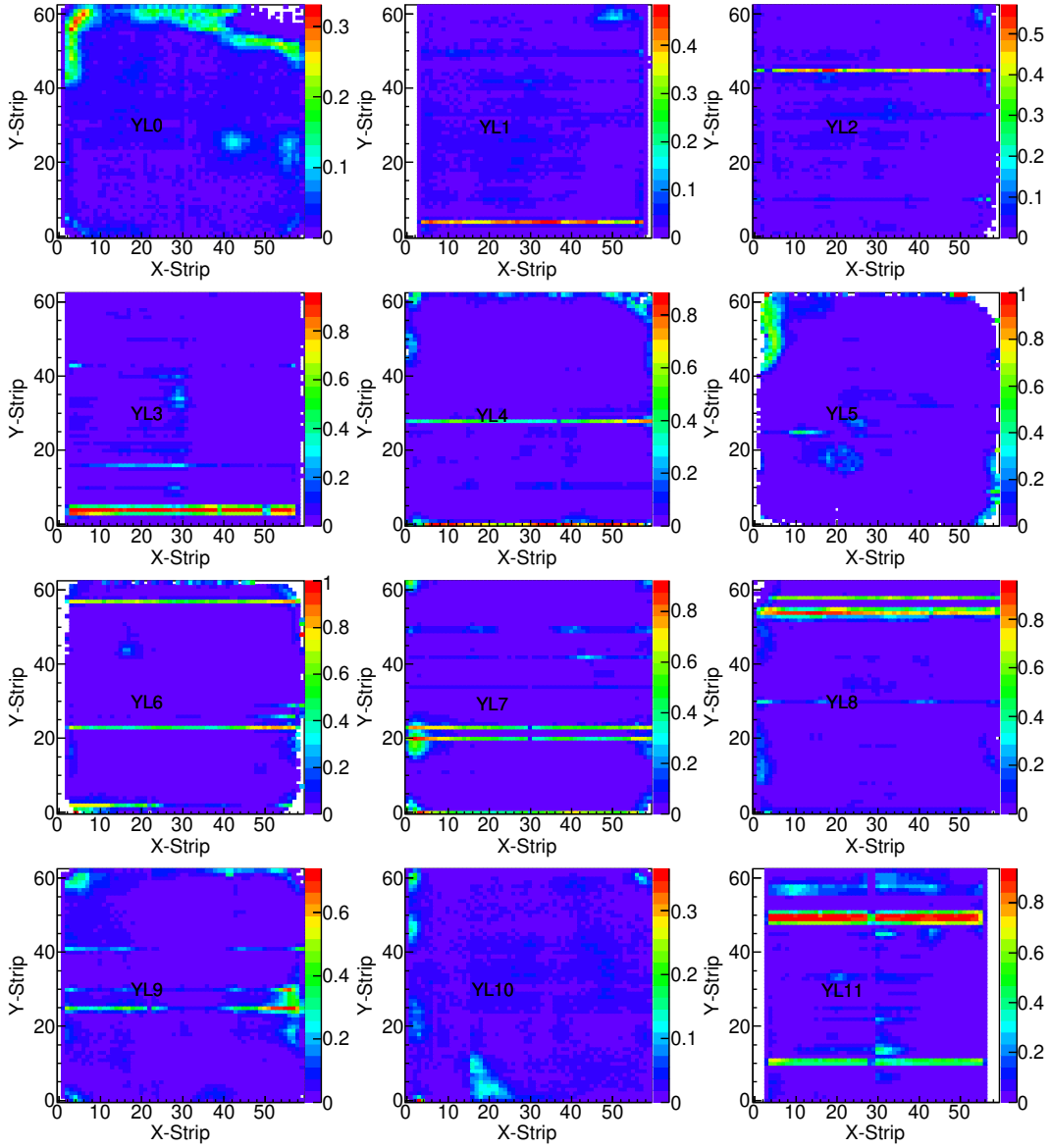

Figure 4.15: Uncorrelated inefficiency map for all 12 layers for the Y-plane.

gap and the presence of a button spacer between the glass plates affects the signal production, which can be observed in the correlated inefficiency map.

The inefficiency due to dead strips, less efficient strips and plane dependent problems related to signal pickup will be observed independently in the X- and Y-plane using uncorrelated inefficiency map. The uncorrelated inefficiencies on each layer in X-plane are calculated by taking the ratio of number of events in X-plane that do not have any hit within one strip of extrapolated position, but the Y-plane has a hit within one strip of extrapolated position, to the total number of

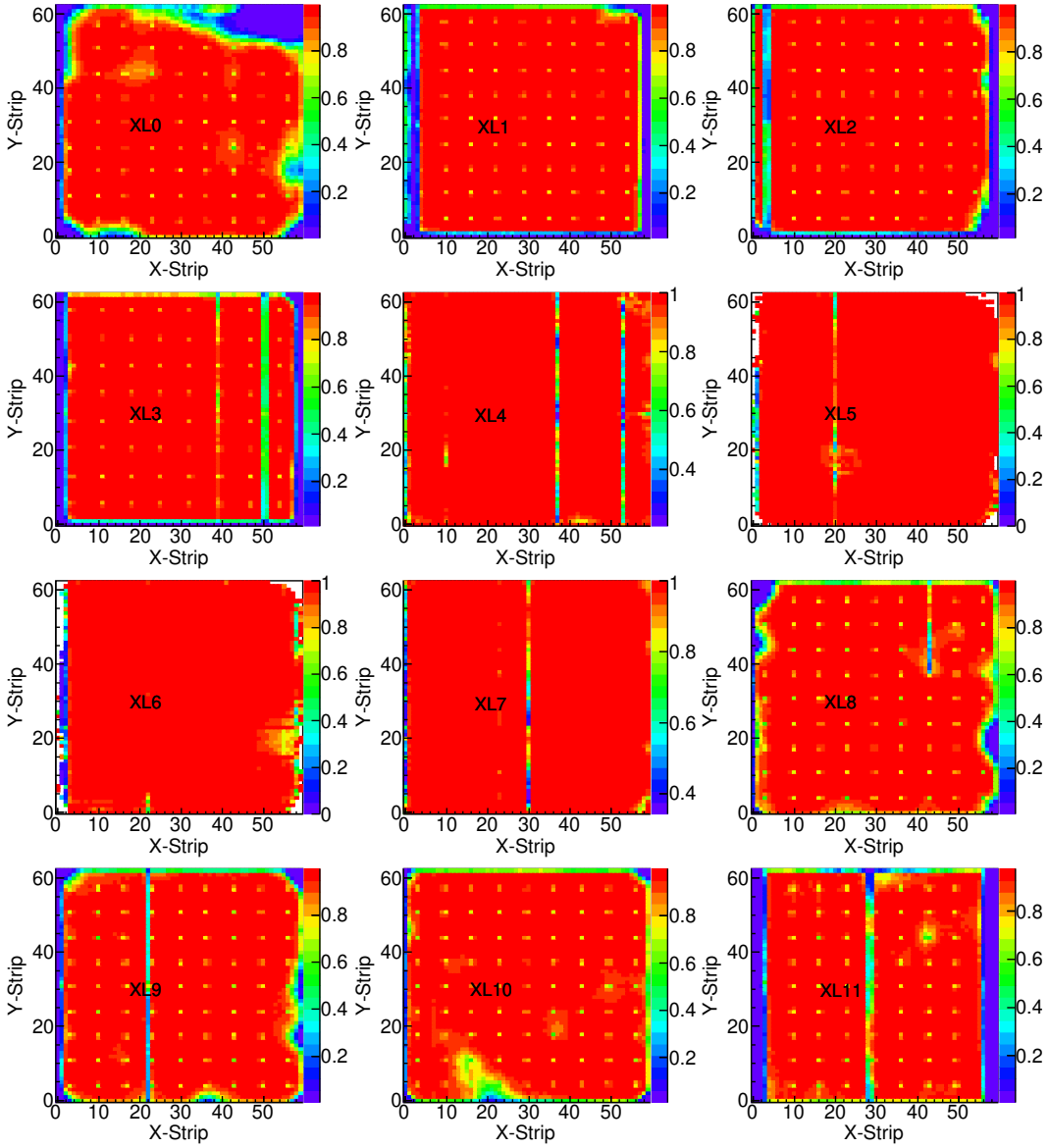

Figure 4.16: Trigger efficiency map for all 12 layers for the X-plane.

events in that pixel. Similarly, the uncorrelated inefficiencies on the Y-plane are also calculated. The uncorrelated inefficiencies for the X- and Y-plane in all RPCs are shown in Figs. 4.14 and 4.15 respectively.

Other than inefficiency map the efficiency maps are also estimated for all 12 RPCs. The efficiency map is generated by looking at the response of each pixel with little relaxed criteria. The observed strip hit may be more than a strip away from the extrapolated muon track due to the inefficiency of the strip where muon passes through. The trigger efficiency is calculated by taking the ratio of the number

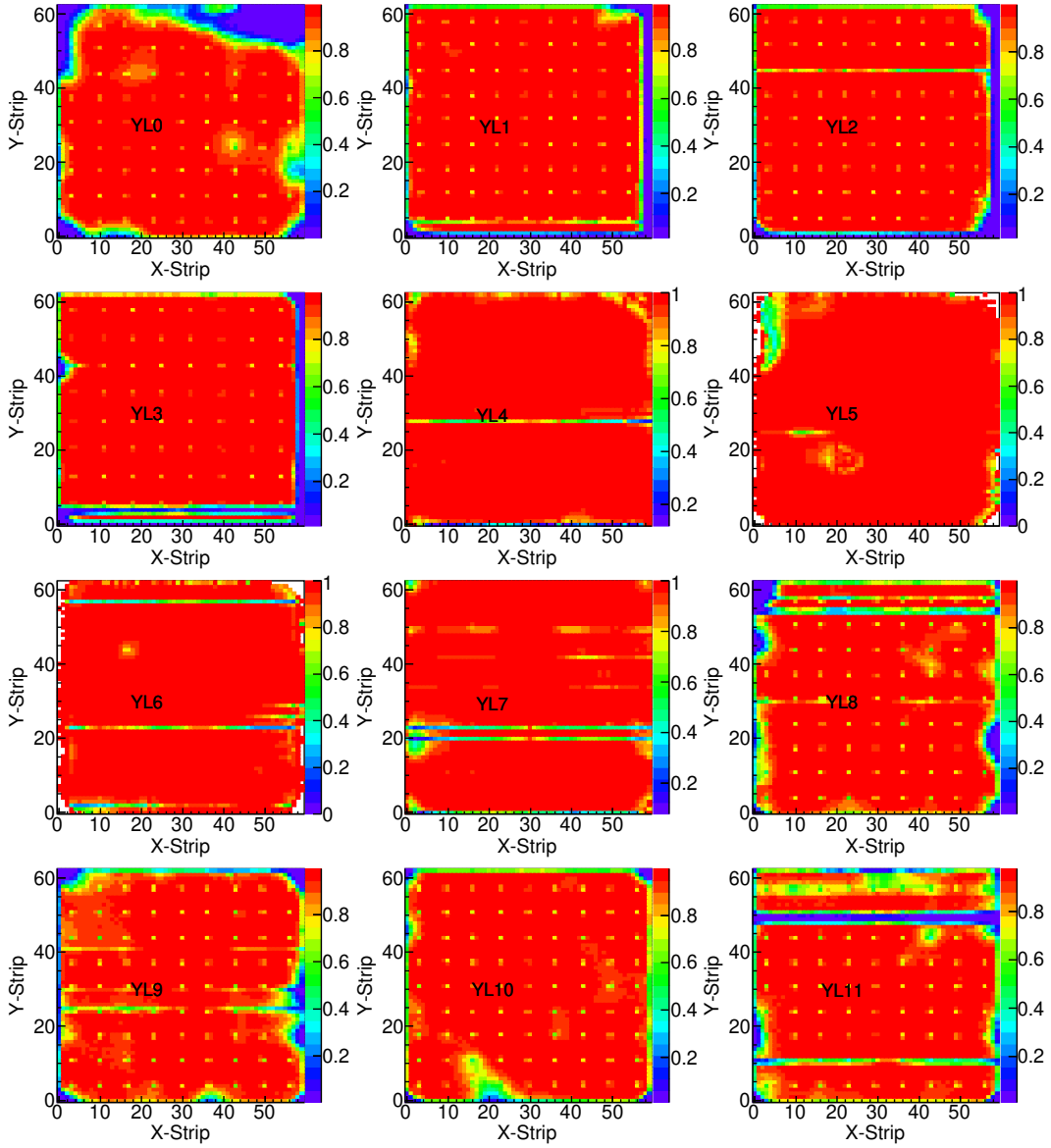

Figure 4.17: Trigger efficiency map for all 12 layers for the Y-plane.

of events having any hit in the layer when a muon has passed through it to the total number of events. The trigger efficiencies observed in the 12 RPCs are shown in Figs. 4.16 and 4.17. The inefficient spots in every 6 strips are due to button spacers, which are placed between two glass electrodes to maintain the uniform gap. The events were triggered by four-fold coincidence of L4, L5, L6 and L7, thus button position is not visible in those layers.

4.5 Monte-Carlo simulation

The MC generation consists of two steps, (*i*) generation of the secondary particles at the observation level using extensive air shower simulation framework called CORSIKA [90] and (*ii*) particle propagation in the GEANT4 [91] and the digitisation of the simulated event.

4.5.1 CORSIKA simulation

To generate the CORSIKA simulated events, the CORSIKA simulation is performed using the following input parameters to the CORSIKA, (*i*) flat geometry is given as a input detector type in the CORSIKA, (*ii*) the magnetic field coordinates of the experimental site (B_X=40.431 μT and B_Z=4.705 μT), (*iii*) the altitude of the experimental site from mean sea level, (*iv*) the rigidity cut off in different (θ,ϕ) bins, which are calculated using back tracing method with a IGRF-12 model[1]. These rigidity cut off used to reject the propagation of primaries having momentum less than the rigidity cut off, (*v*) the primary proton and Helium with a relative fraction of 90:10 % are generated in the input energy range from 10 GeV to 1 PeV (with a spectral index -2.7), (*vi*) input range of zenith and azimuth angle of primaries are 0 to 85 degrees and -180 to $+180$ degrees and (*vii*) the minimum energy of the secondaries to be stored in the observation level (for muons and hadrons $\geq$100 MeV).

The selected atmosphere model plays a dominant role in the spectrum of cosmic ray particles in sea level. In CORSIKA simulation, U.S standard is given as default atmosphere model (ATMOD1). The atmospheric model adapted in CORSIKA consists of N_2, O_2 and Ar with a volume fraction of 78.1 %, 21.0 % and 0.9 % respectively. The density profile as a function of altitude is modeled by 5 different layers. Where the first four layers follow an exponential behaviour in the density

[1]The rigidity cut off table for experimental site was generated by Dr. P. K. Mohanty and Mr. Hariharan, GRAPES-3 experiment, TIFR

variation, the top layer has linear dependency on altitude. The relation between mass over burden ($T(h)$ of the atmosphere and height(h) for lower four layers is given as Eqn. 4.13.

$$T(h) = a_i + b_i.e^{-h/c_i} \qquad i = 1, 2, 3, 4. \tag{4.13}$$

and for fifth layer, the relation follows,

$$T(h) = a_i - b_i h/c_i \qquad i = 5. \tag{4.14}$$

Where the parameters, a_i, b_i and c_i are parameterized by J. Linsley [90]. The position information of the particles at the observation levels are digitised into squares with an area of $\sim 2\,\mathrm{m} \times 2\,\mathrm{m}$. The global position of the particle is translated into a local position with respect to the centre of the square. All other pieces of information about the particle at the experimental site are stored in the root-tuple. In CORSIKA simulation, SIBYLL and GHEISHA interaction models are used for high and low energy hadrons respectively. Since the fluxes are dominated by the low energy contributions, the comparison with different low energy hadron models is also performed.

4.5.2 GEANT4 Simulation

To account for the passage of the particles through the materials of the detector, a detector simulation package has been developed using the GEANT4 simulation framework. The experimental hall along with nearby buildings and the 12 layer RPC stack inside the experimental hall are included in the geometry for the simulation. Here, the secondary particles are generated above the roof of the building. The various detector parameters like uncorrelated and correlated inefficiencies, trigger inefficiencies and strip multiplicity, which are estimated using the data sample,

are incorporated during the digitization process of simulation. The steps followed in the MC event generation are,

1. A position (x, y) and momentum component (P_x, P_y and P_z) of the secondaries extracted from the output of CORSIKA is used to generate the particles on the topmost trigger layer (i.e., layer 7). The generated particle position is extrapolated to the bottom trigger layer to test the acceptance condition. The event generation vertex on top of the roof is calculated for the set of (x, y, P_x, P_y, P_z) and given as input to the event generation vertex of the GEANT4.

2. The particle passage through the detector medium and other materials are carried out by GEANT4. After interaction of the particle with detector volume, the hit position and timestamp at each layer is given by GEANT4 and the hit positions in each layer are translated to strip hit pattern.

3. Once the strip hit information in each layer is extracted, the detector related effects on the hit position in both X- and Y-plane are incorporated. The pixel-wise correlated inefficiency map calculated from the data is used to accept the hit position in X- and Y-plane simultaneously. If the hit position in a layer is not satisfying the correlated inefficiency, the further digitization process of that layer is not performed.

4. The hit position within the strip is calculated for the accepted hits after the correlated inefficiency map. In the observed data, the avalanche produced inside the gas gap can induce multiple strips. The strip multiplicity of each layer depends on the position at which muon passes through from the middle of the strip. The probability of different strip multiplicity depends on the location in a strip where the particle passed through is estimated from the data and incorporated in the MC.

5. The uncorrelated inefficiency calculated from the data is used to accept the strips after incorporating the strip multiplicity.

6. Other than the muon hits, there will be random noise hits from the electronics and multi-particle shower. The noise hits are estimated and incorporated in the digitization process.

7. The estimated trigger efficiency from the data is incorporated in the trigger layers (namely layers 4, 5, 6 and 7) in the X- or Y-plane to accept the event for further analysis.

4.5.3 Comparison of Data and MC

The simulated MC events are analysed using the same reconstruction algorithm used for data. The comparison of χ^2/ndf and the number of layers hit on both X- and Y- planes is shown in Fig. 4.18. The comparison shows that χ^2/ndf and number of layers from the MC is comparable with data. The number of layer upto three are mostly from the shower events and electronics correlated noise. The physics study is performed using the events with number of layers more than 5, where data and MC shows better match. The comparison of the occupancy and strip multiplicity in data and MC for X-plane and Y-plane are shown in Figs. 4.19, 4.20, 4.21 and 4.22 respectively. From the comparison it can be inferred that occupancy and multiplicity from MC has a reasonably good match with data. Similar match has been observed in Y-plane also. The occupancy and multiplicity for the MC have very good match with data. The correlated inefficiency maps for all layers for MC are shown in Fig. 4.23. The button spacer (less efficient spots in every 6 strips) and lower efficiency regions observed in data are well reproduced in MC. The uncorrelated inefficiency and trigger efficiency maps for X-plane for MC are given in Figs. 4.24 and 4.25. The inefficiency and efficiency maps shown for X-plane from MC is a good match with data. Y-plane efficiencies also have similar

match between data and MC.

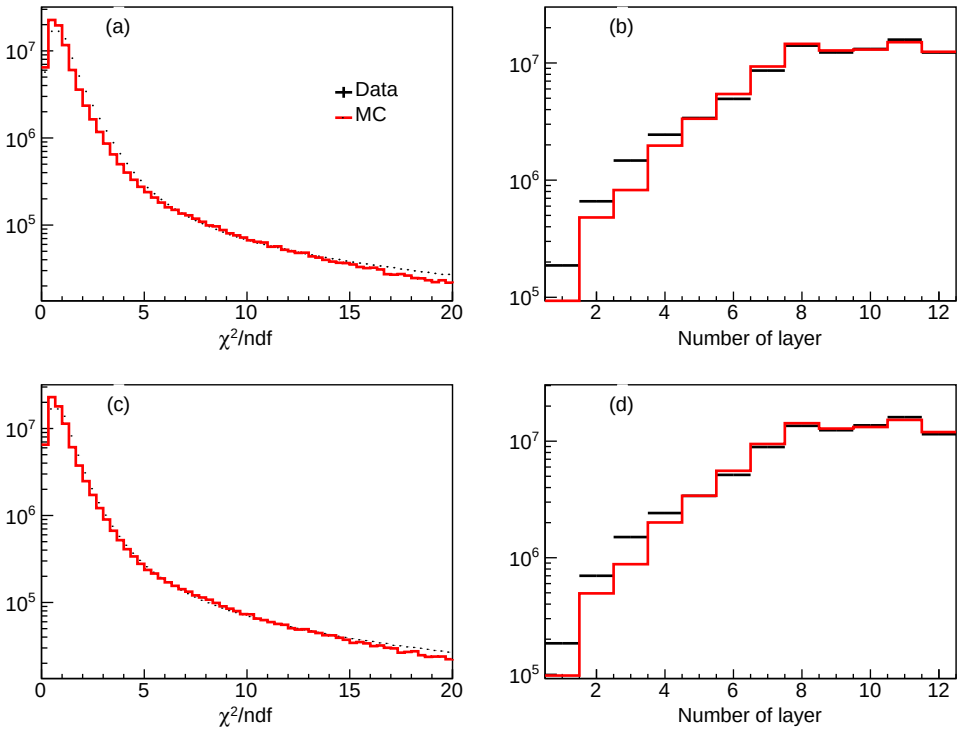

Figure 4.18: (a,c) χ^2/ndf for Data and MC in X- and Y-plane. (b,d) Number of layers in Data and MC for X- and Y-plane.

Correlated inefficiency, uncorrelated inefficiency and trigger efficiency maps obtained from MC events have a very good match with data (discussed in Section 4.4). All the button spacers, inefficiency regions and dead strips are visible in both data and MC.

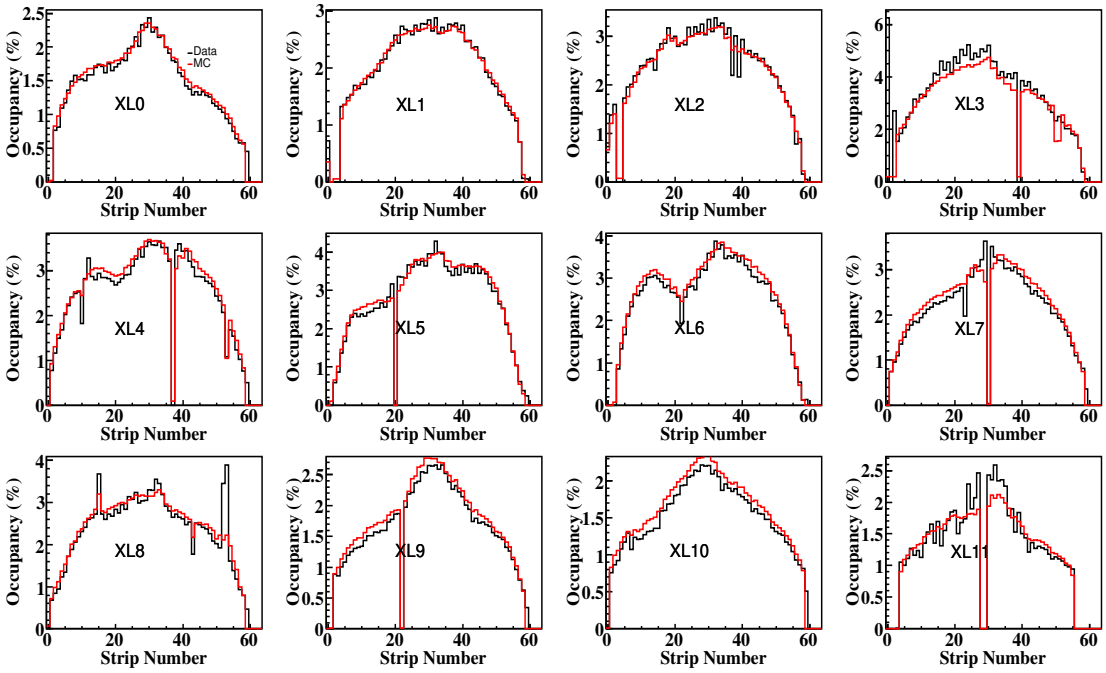

Figure 4.19: Occupancy for data (black lines) and MC (red lines) simulated events for all the layers (X-plane).

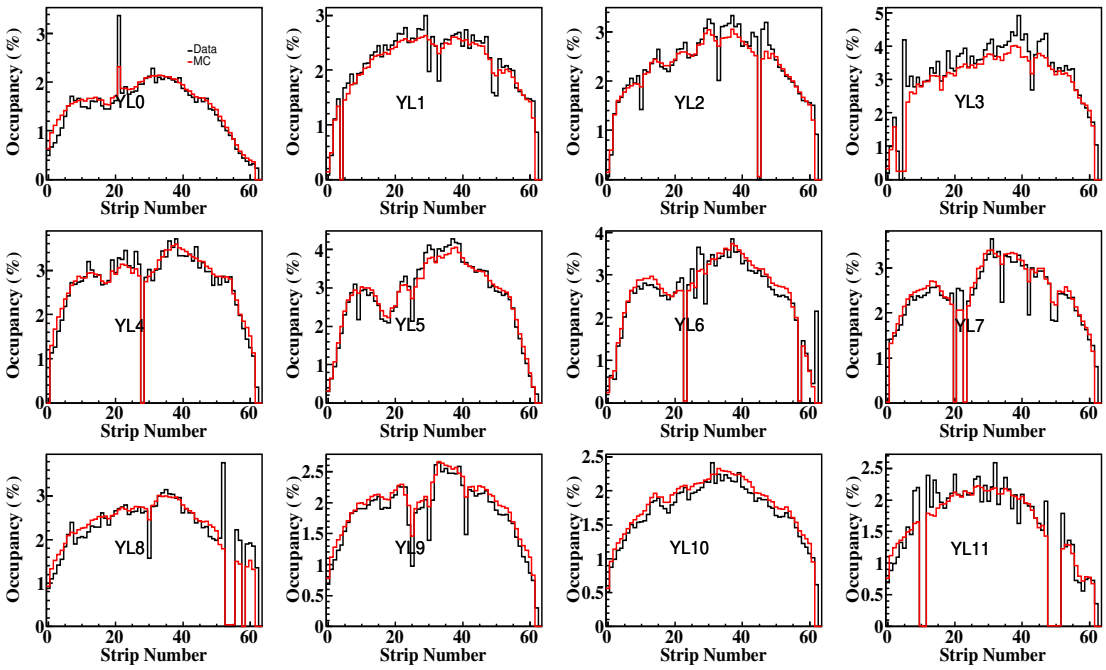

Figure 4.20: As in Fig. 4.19 for the Y-plane.

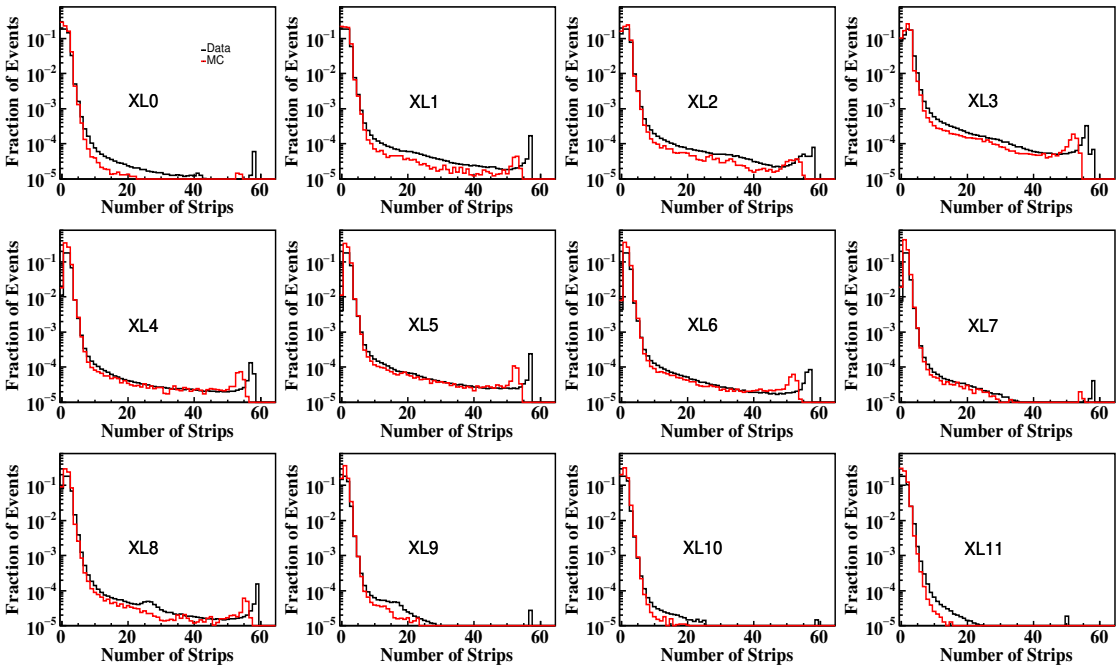

Figure 4.21: Multiplicity for data(black) and MC(red) simulated events for all the layers (X-plane).

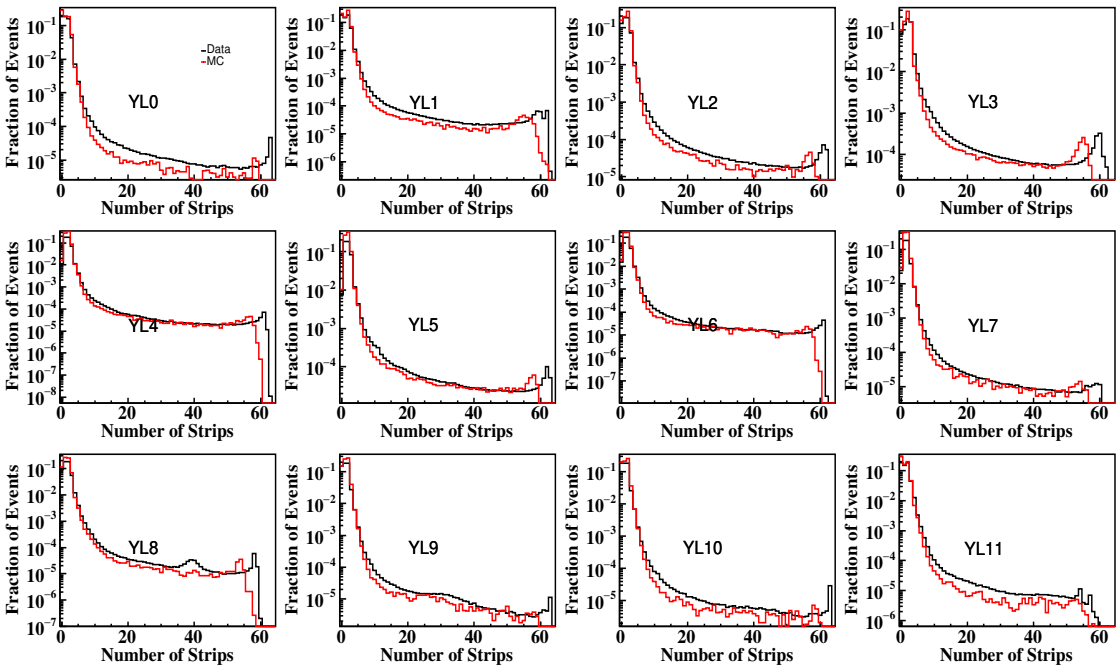

Figure 4.22: As in Fig. 4.21 for the Y-plane.

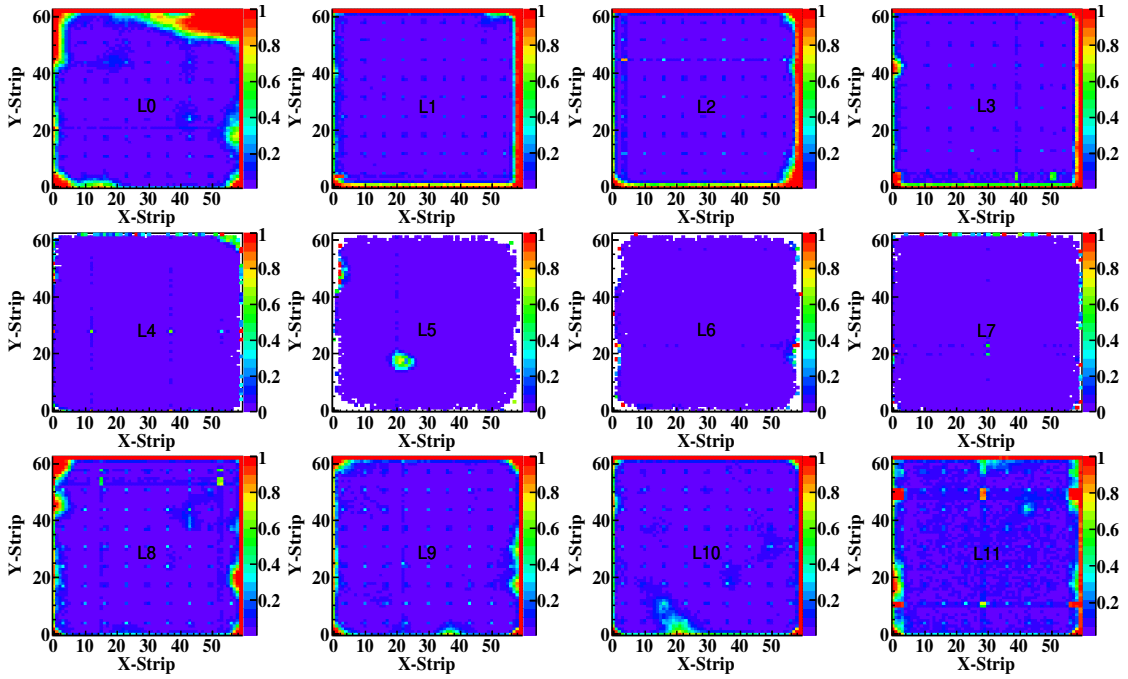

Figure 4.23: Correlated inefficiency in MC for all the layers.

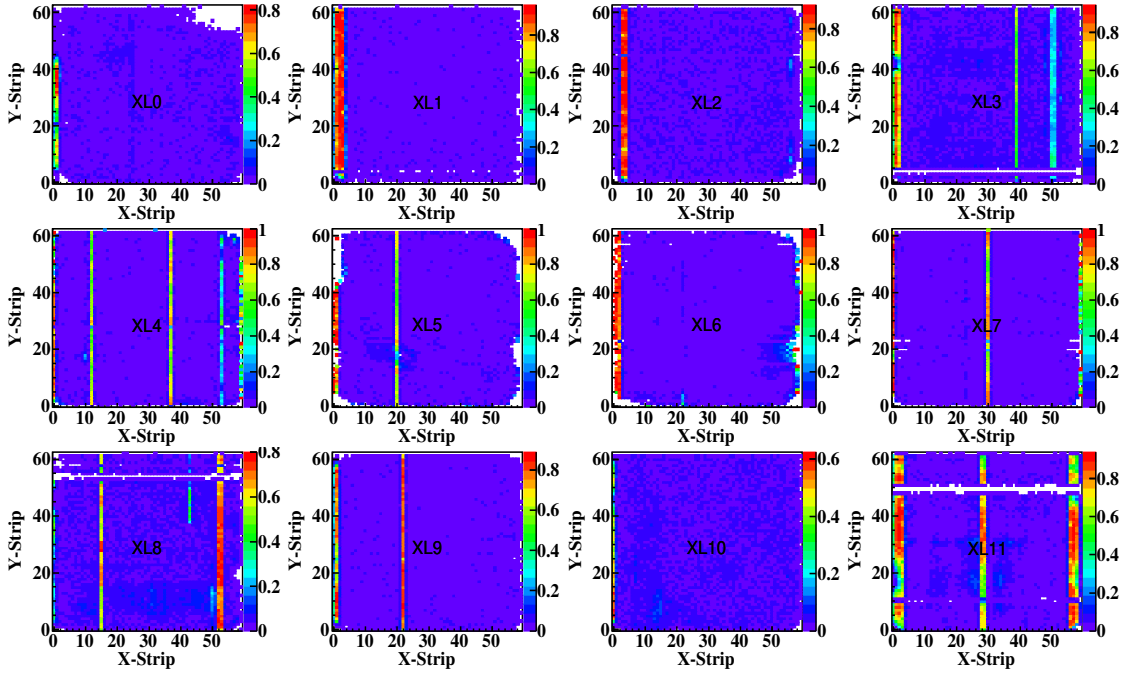

Figure 4.24: Uncorrelated inefficiency in MC for all the layers in X-plane.

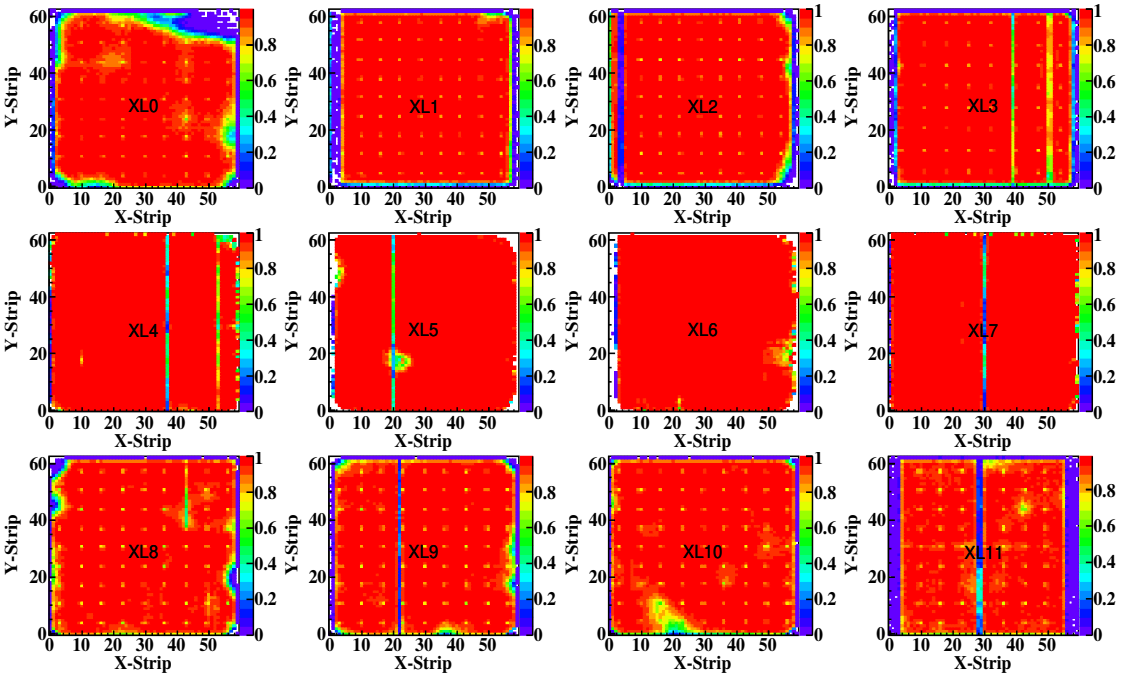

Figure 4.25: Trigger efficiency in MC for all the layers in X-plane.

Chapter 5

Results of the Experiment

5.1 MC study for Geometrical Aperture of the Detector

Before studying the cosmic muon spectrum using RPC only stack, the calculation of aperture of the RPC stack as function of zenith, azimuth angle and input momentum is vital. The simulation is performed to study the detailed aperture variation with θ, ϕ and P_μ. For this purpose simulation is performed without inheriting the shape of cosmic muon flux in GEANT4 simulation (GEANT4 simulation is explained in Chapter 4 (subection 4.5.2)). To generate the position, momentum, zenith and azimuth of the muon randomly in the X- and Y-planes, random numbers are generated in the topmost hardware trigger layer (i.e, layer 7). The X- and Y-positions are generated 20% larger than detector size. The zenith angle of the muons are generated uniformly over solid angle in the range of 0 to 75 °[1], the azimuthal angle is generated uniformly between -180 to $+180°$ and the momentum of the muon is generated uniformly.

The simulated MC events are analysed using the same reconstruction algorithm used for data. The reconstructed muons are filled in 3D histogram as a function of

[1]Due to solid angle coverage of the trigger layers, there is no muon with $\theta \geq 75°$.

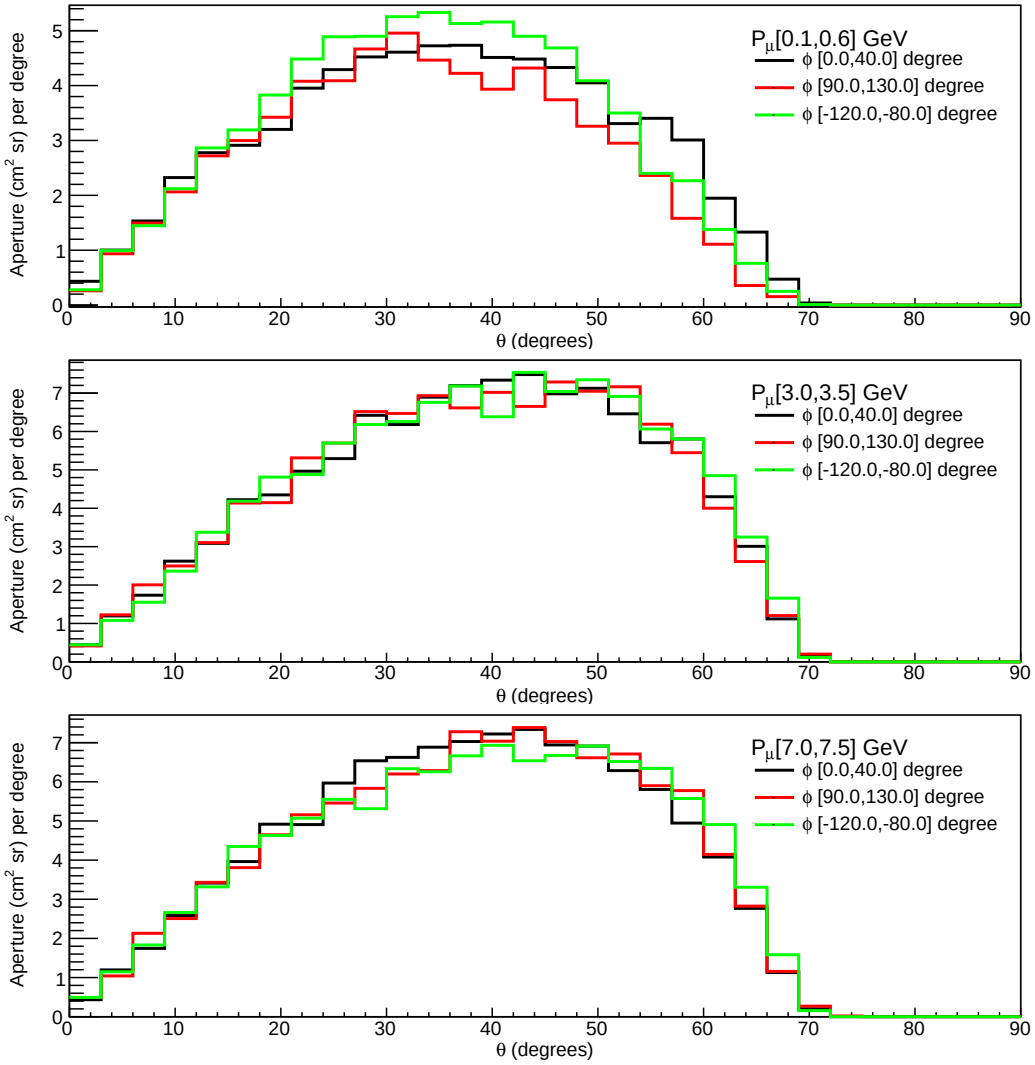

Figure 5.1: (a), (b) and (c) are the variation of detector aperture as a function of θ with a different ϕ for P_μ[0.1,0.6] GeV, P_μ[3.0,3.5] GeV and P_μ[7.0,7.5] GeV respectively.

θ, ϕ and input momentum (P_μ). Proper normalisation λ (shown Eqn. 5.1) of this distribution gives a aperture in the units of cm^2sr.

$$\lambda = \frac{AN^{reco}}{N^{gen}} \int_{0^\circ}^{75^\circ} \sin\theta d\theta \int_{0^\circ}^{360^\circ} d\phi \quad cm^2\ sr\ , \tag{5.1}$$

where A is the area of the detector, N^{reco} and N^{gen} are number of events reconstructed and generated respectively. The aperture as a function of the θ for different values of ϕ and P_μ is shown in Fig. 5.1. The shape of distribution shows there are no events at θ=0 due to the solid angle ($\sin\theta$) factor of the detector. The

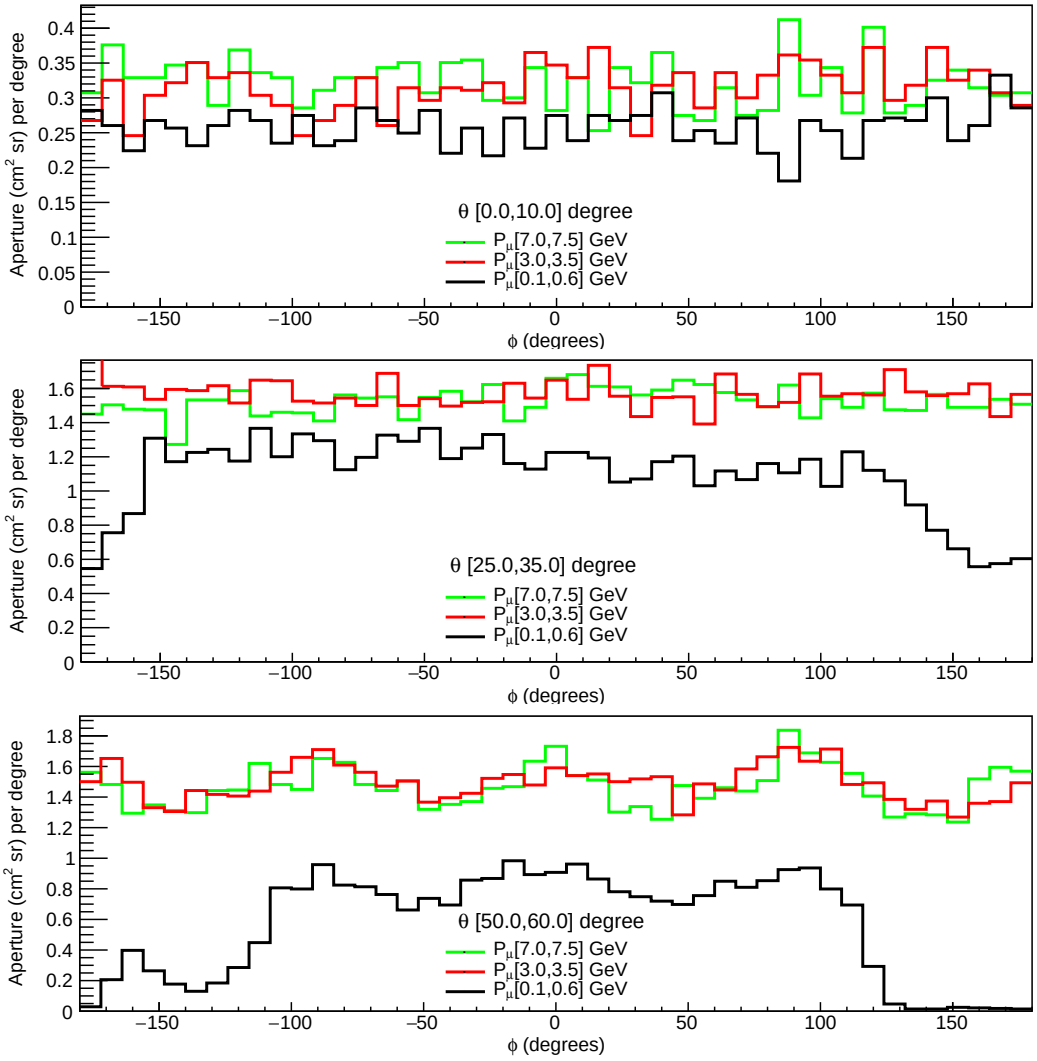

Figure 5.2: (a), (b) and (c) are the variation of detector aperture as a function of ϕ with a different P_μ for θ[0,10] degree, θ[25,35] degree and θ[50,60] degree respectively.

dependence of the calculated aperture for fixed values of P_μ and different values of ϕ shows there is no change in shape of the distribution with different ϕ values. The aperture as a function of θ with P_μ in the range [0.1,0.6] GeV shows different shape than the distribution with P_μ in the range [3.0,3.5] GeV and P_μ from [7.0,7.5] GeV. The muons coming from larger θ will experience more material thickness. The momentum cut-off due to the materials present in the stack and around the experimental hall will increase with θ, which will cause decrease in aperture for the low energy muons coming from larger θ.

The comparison of aperture as a function of azimuthal angle (ϕ=0 is defined to

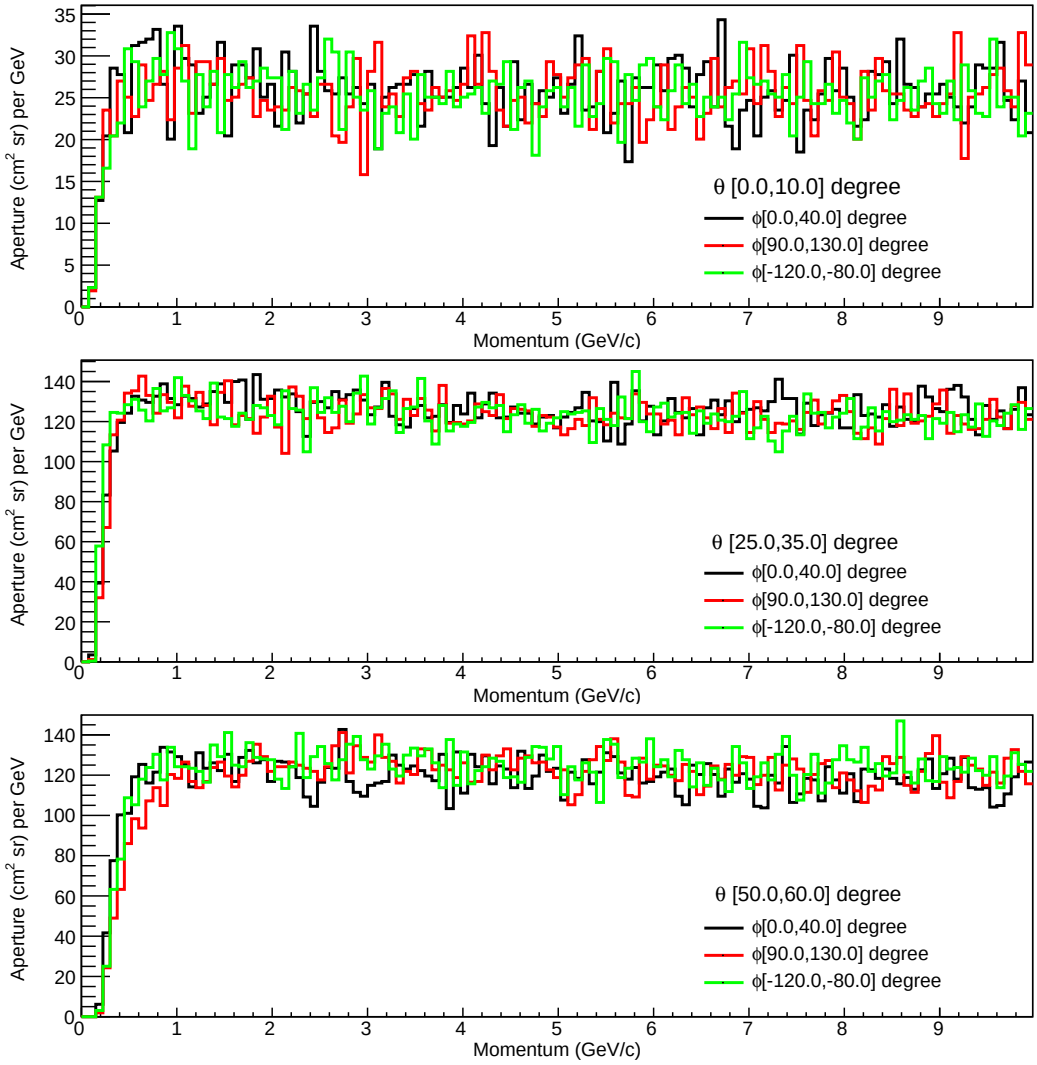

Figure 5.3: (a), (b) and (c) are the variation of detector aperture as a function of P_μ with a different ϕ for θ[0,10] degree, θ[25,35] degree and θ[50,60] degree respectively.

be the geographical south.) at different momentum for three different fixed zenith angle is shown in Fig. 5.2. Since the RPC-Only stack doesn't have magnetic field, thus the ϕ dependence in aperture is not expected. The shape of the aperture as a function of ϕ is uniform for the lower θ-bins. The distribution for θ[50,60] degree shows four distinct peaks which is caused by the square shape of the detector. The aperture at ϕ values of -90, 0, 90, 180 degree are larger in comparison with other ϕ values. The decrease in the aperture between 110 to 180 degree and -180 to -110 degree (θ[50,60] degree, P_μ[0.1,0.6] GeV) is caused by a three-storey building present outside of the experimental hall. The shape of the aperture distribution is

more or less uniform between −100 (West) to 100 (East) degrees.

The variation of aperture as a function of input muon momentum for same θ and different ϕ is shown in Fig. 5.3. As expected, the shape of the aperture as a function of momentum doesn't show much dependence with different ϕ. Aperture distribution is more or less uniform beyond 0.6 GeV, which suggests the aperture is almost independent of input energy.

5.2 Estimation of muon flux at different (θ, ϕ) bins

The standard way of calculating muon flux (Φ_μ) follows,

$$\Phi_\mu = \frac{N_\mu}{S.\Omega.T} \ , \tag{5.2}$$

where N_μ, S (cm^2), Ω (sr) and T (s) are observed number of muons, area of the detecor, open angle of detector and observation time respectively. The aperture ($S.\Omega$ (θ, ϕ, P_μ) is estimated from the simulation framework. Considering the observed number of muons ($N^{\pm}(\theta, \phi, P_\mu)$) as a function of θ, ϕ and P_μ, the integrated flux can be written as,

$$\Phi_\mu^{int}(\theta, \phi) = \sum_{\pm} \int \frac{N^{\pm}(\theta, \phi, P_\mu)}{S.\Omega(\theta, \phi, P_\mu).T} dP_\mu \ . \tag{5.3}$$

The azimuthal variation of flux is measured in ten different θ bins. The width of θ-bin varies with cosθ (dcosθ = 0.05) and width of each ϕ-bin is taken to be 30°. The RPC only stack was used to study the muon flux, where the muon momentum cannot be measured using the detector. Then Eqn. 5.3 can be rewritten as,

$$\Phi_\mu^{int}(\theta, \phi) = \frac{N'(\theta, \phi)}{S.\Omega'(\theta, \phi).T} \ , \tag{5.4}$$

where $N'_{(\theta,\phi)}$ (energy integrated) are the number of events reconstructed in each (θ, ϕ) bin which have χ^2/ndf less than 8 and having hits in more than five layers in both X- and Y-plane; these are used to estimate the intensity of muons at various (θ, ϕ) bin. $S\Omega'(\theta, \phi)$ is energy integrated aperture as a function of θ and ϕ. The aperture $S\Omega'(\theta, \phi)$ differ from the geometrical aperture.

Since the cosmic ray flux has $\cos^2\theta$ dependence and is also not uniform in ϕ, we need to calculate the modified aperture, where the aperture is calculated after inheriting the shape of cosmic muon flux in simulation. The GEANT4 simulation is performed, where the input information of the particles in the GEANT4 is extracted from CORSIKA simulation explained in Chapter 4, section 4.5 (where the θ and ϕ of secondaries are not uniform).

The solid angle aperture ($S\Omega'(\theta, \phi)$) in each (θ, ϕ) is written as,

$$S\Omega'(\theta,\phi) = \frac{AN_G^{accep}(\theta,\phi)}{N_G^{gen}(\theta,\phi)} \frac{N_D^{reco}(\theta,\phi)}{N_D^{accep}(\theta,\phi)} \int_{\theta_i}^{\theta_f} \cos^2\theta \sin\theta d\theta \int_{\phi_i}^{\phi_f} d\phi \;\; (cm^2 sr) \;, \quad (5.5)$$

where A is the area of the detector, $N_D^{reco}(\theta, \phi)$, $N_D^{accep}(\theta, \phi)$ ($N_G^{accep}(\theta, \phi)$) and $N_G^{gen}(\theta, \phi)$ are number of reconstructed, accepted and generated muons in each (θ, ϕ) bin.

The factor $N_G^{accep}(\theta, \phi)/N_G^{gen}(\theta, \phi)$ is a geometry dependent.
The factor $N_D^{reco}(\theta, \phi)/N_D^{accep}(\theta, \phi)$ is mainly affected by the detector parameters such as pixel-wise inefficiency, trigger efficiency, strip multiplicity and input spectrum to GEANT4 simulation. The estimated values of $N_G^{accep}(\theta, \phi)/N_G^{gen}(\theta, \phi)$ and $N_D^{reco}(\theta, \phi)/N_D^{accep}(\theta, \phi)$ are shown in Figs. 5.4 (a) and (b) respectively. The modified aperture calculated from Eqn. 5.5 is given in Fig. 5.5.

The total time taken to record data incldues the dead time due to data acquisition system (dead time of DAQ is 500 μs/event). The corrected live time of the experiment can be written as, $T = T_{total}\, \epsilon_{daq}$ in seconds. Here ϵ_{daq} is the DAQ efficiency (which is found to be 89%), fraction of the time in a second the DAQ is

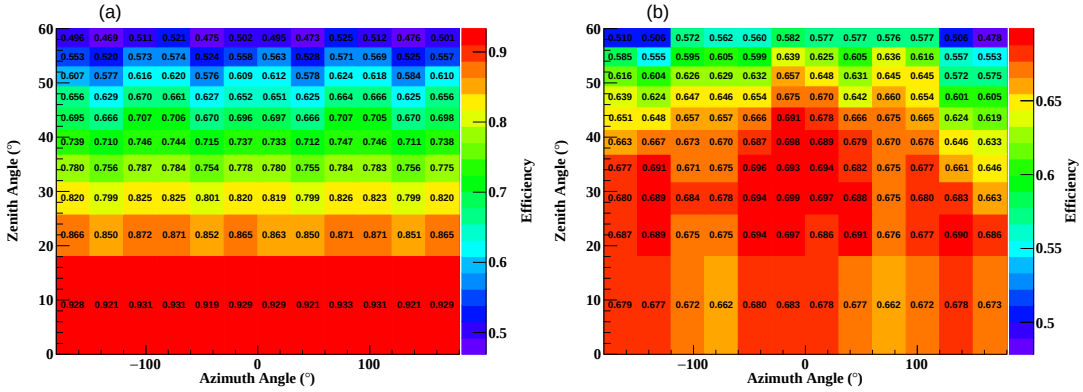

Figure 5.4: (a) and (b) are $N_G^{accep}(\theta,\phi)/N_G^{gen}(\theta,\phi)$ and $N_D^{reco}(\theta,\phi)/N_D^{accep}(\theta,\phi)$ respectively.

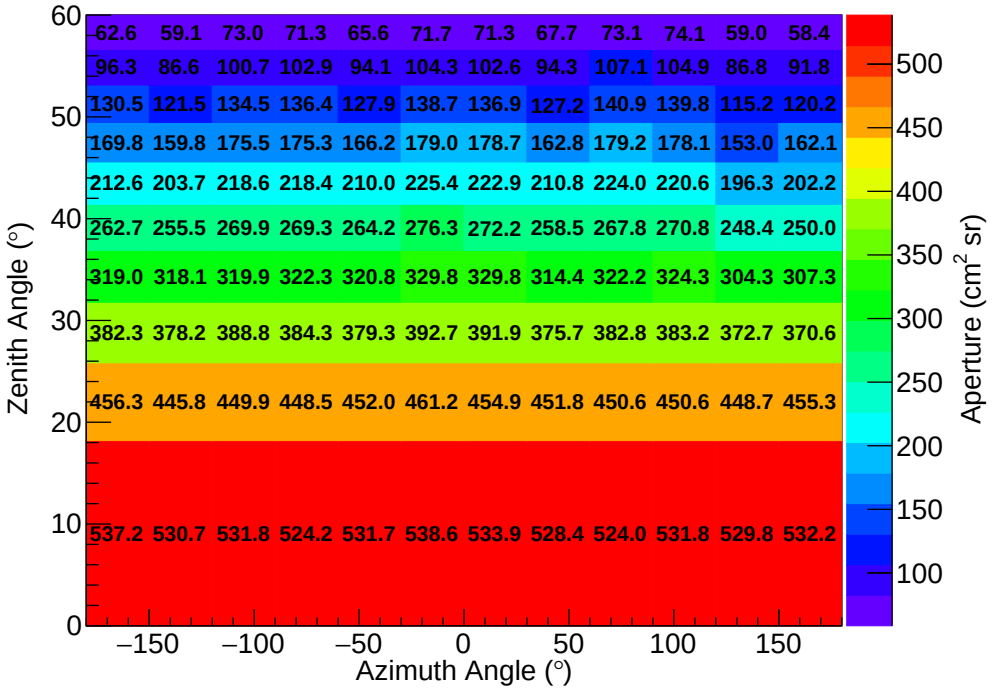

Figure 5.5: The Modified aperture at each (θ,ϕ) bins after incorporating shape of cosmic muon spectrum in MC. The bin width in θ various as dcosθ = 0.05 and bin width of ϕ is 30 degrees.

ready to accept the muon trigger. The total time (T_{total}) taken to record the data is 415047 seconds.

5.3 Systematic studies

Before we go on to compare the data with MC to obtain the azimuthal dependence of the flux, we examine the systematic uncertainties. The observed muon flux with specific input parameters is not sufficient, hence we need to study the effect on observed flux due to the uncertainties associated with those input parameters. To study the systematic variation of the muon flux at different (θ, ϕ), a detailed systematic study is performed by changing the parameters related to the input spectrum of the secondary particle, detector related uncertainties and the uncertainty in the geometry description in GEANT4. The parameters varied to estimate the systematic errors are described below.

1. The input muon spectrum to GEANT4 is extracted from the CORSIKA, where the SIBYLL high energy hadronic interaction model is used at high energies, but the true momentum spectrum at the experimental site may differ from the simulation. To study the variation in the muon flux by changing the interaction model was changed to HDPM, EPOS-LHC and QGSJETTII. The momentum spectrum of the particles extracted from the new interaction model is used in the GEANT4 simulation and the muon flux is estimated for different (θ,ϕ) bins.

2. The estimated detector inefficiency for all the RPCs are incorporated during the digitisation of the MC generated events. The uncertainty in the inefficiency may cause the wrong estimation of the muon flux. To account for the variation on the muon flux due to uncertainty in the inefficiency, the inefficiency of the each 3 cm×3 cm pixel is increased and decreased by 1σ during the digitisation.

3. Similar to the inefficiency of the detector, the trigger efficiency used in the trigger layers to accept the event for the analysis also has uncertainty. The variation of the muon flux at different (θ,ϕ) bins, the estimated trigger efficiencies are increased and decreased by 1σ during the digitisation.

4. The random noise and the noise due to the multiparticle shower is extracted and incorporated in the digitisation process. The variation in the random noise is not the same throughout the data acquisition period. It is observed that the noise is varying up to 10 %. To account for the variation in the muon flux due to variation in noise, the average noise is increased and decreased by 10 %. The muon flux in different (θ,ϕ) bins is calculated using the generated MC.

5. The material description defined in GEANT4 geometry is based on the conventional material density and thickness used in the roof and walls of the buildings. But the used value may not be the true material description. The incorrect modelling of the material description will affect the momentum cut off at low energies. To study the variation of the muon flux at different (θ,ϕ) bins, the roof and wall thickness of the building is changed by 10 %.

6. The low energy particles are more prone to undergo multiple scattering when it is passing through the matter. The RPC detector assembly is kept in an aluminium honeycomb tray, which may cause the multiple scattering of the muons; this results in the smearing of the incident direction of the muons. To account for the uncertainty in the density of the aluminium tray, the density of the tray is changed by 10 %.

7. The reduced-χ^2 from data and MC are expected to be the same after incorporating all the detector parameters in the simulation. But MC may not exactly reproduce the data, so the difference in the reduced-χ^2 in data and

MC are also considered as systematics. To account for this, the events in MC are selected with scaled χ^2/ndf.

8. To estimate the muon flux in different (θ,ϕ) bins, the events are with criteria that it must have hits in a minimum of 5 layers in both X- and Y-plane. The minimum layer is chosen to have enough statistics, track length and the larger angular acceptance. But there is no attempt to find the optimised minimum layer hits. This criterion can cause uncertainties in the estimated muon flux. To account for those, the flux is estimated using the events that have hits in a minimum of 4 layers in both X- and Y-plane.

9. To study the consistency in the calculated muon flux in different (θ,ϕ) bins throughout the data taking period, the data sample is split into two sets as odd-numbered and even-numbered events. The flux is calculated for these two data samples separately.

   The percentage change in the muon flux for all these systematics are shown in Fig. 5.6. The errors are less than about 2 % in all cases.

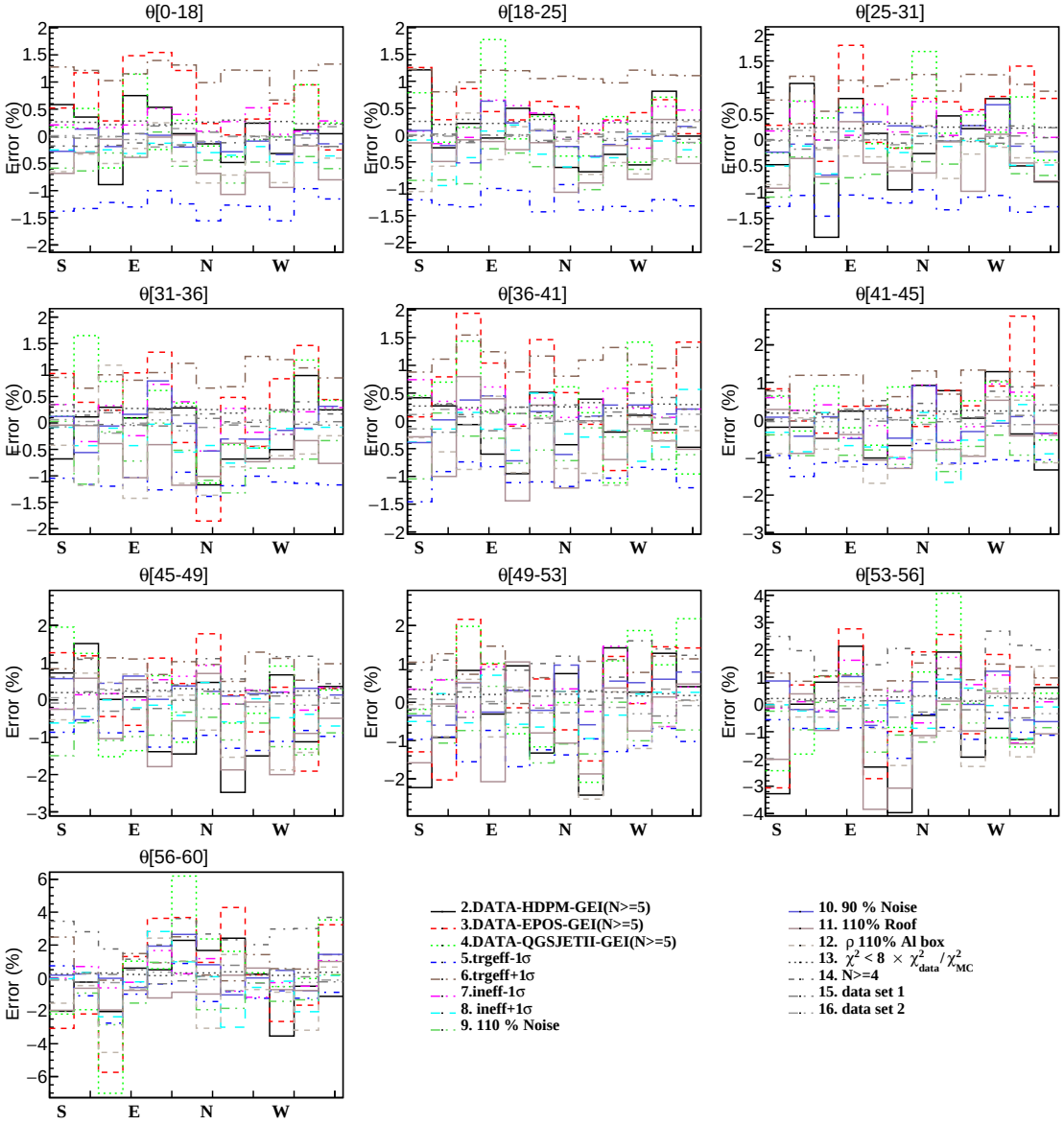

Figure 5.6: Systematic errors in the estimation of muon flux for various (θ, ϕ) bins.

5.4 Comparison of observed flux with CORSIKA and HONDA prediction

The observed muon flux in different (θ,ϕ) bins are compared with different predictions. The predictions from CORSIKA are generated using different input models. A set of events are generated by fixing the high energy interaction model and changing the low energy interaction models (namely SIBYLL-GHEISHA (SG), VENUS-GHEISHA (VG), HDPM-GHEISHA (HG), EPOS-GHEISHA (EG), and

QGSJETTII-GHEISHA (QG)). Another set of events are generated by fixing the low energy interaction models and different high energy input models (namely SIBYLL-FLUKA (SB) and SIBYLL-urQMD (SU)). The shape of the azimuthal muon flux from CORSIKA using different high energy models do not differ much, so CORSIKA events are not generated for FLUKA and urQMD with different high energy models other than SIBYLL.

The primaries below the energy of 100 GeV are prone to be affected by the earth's magnetic field. The primaries with much larger energy will be minimally affected due to the geomagnetic field. In the CORSIKA simulation, primaries with energies below 80 GeV are handled by low energy interaction models. Above that energy, high energy interaction models will be incorporated. Fig. 5.7 shows the comparison of the observed muon flux with CORSIKA and HONDA predictions along with the following fit function,

$$f(\phi) = P_0(1 + A\sin(-\phi + \phi_0)) \ , \tag{5.6}$$

where the parameters P_0, A and ϕ_0 are average muon flux from the observed flux, asymmetry and phase of the distribution. The fitted asymmetry parameters, A and ϕ_0 are shown in Figs. 5.8(a) and 5.8(b) respectively. To compare the shape of the MC predictions and data, the MC predictions are scaled using the observed flux. The comparison of P_0 for the data and MC are not discussed in the present work.

The comparison of the measured result with the predictions are quantified using,

$$\chi^2_{cos\,\theta} = \sum_{\phi_i=1}^{\phi_i=12} \frac{(I^{data}_{\phi_i} - I^{MC}_{\phi_i})^2}{\sigma^2_{\phi_i}}, \tag{5.7}$$

where $I^{data}_{\phi_I}$, $I^{MC}_{\phi_i}$ and $\sigma^2_{\phi_i}$ are the observed muon flux, the MC prediction of flux in various azimuthal bins and total error respectively. The list of the calculated $\chi^2_{cos\theta}$ (for 12 bins) using Eq. 5.7 is shown in Table 5.1. Also to compare the model with

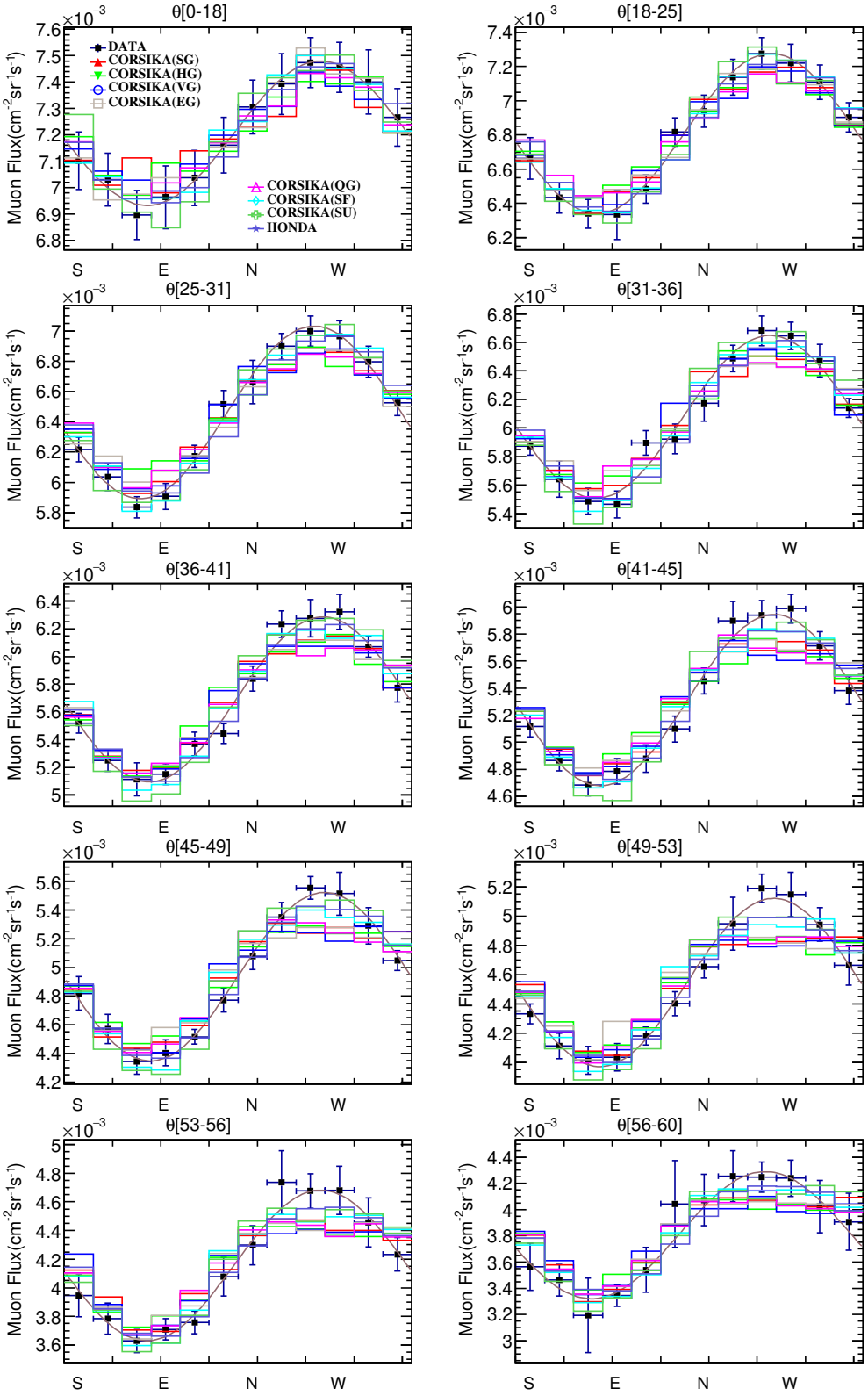

Figure 5.7: Comparison of the azimuthal muon flux with CORSIKA and HONDA predictions (Error in each bin is a quadratic sum of all systematic uncertainties and statistical error).

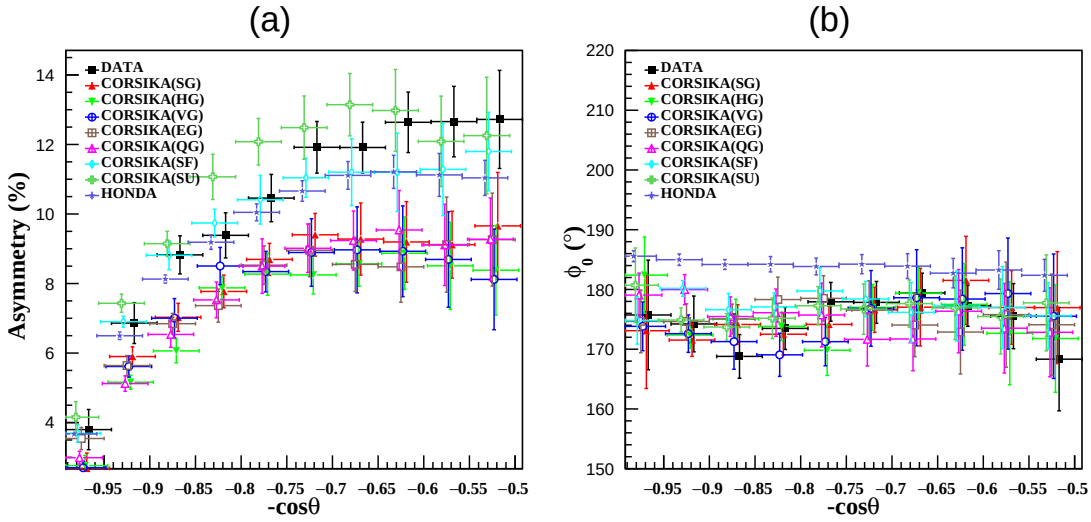

Figure 5.8: (a) Asymmetry parameter for data, CORSIKA and HONDA, (b) ϕ_0 parameter for data, CORSIKA and HONDA. (X-coordinates are shifted in different sets by different value for better visualisation)

data including all θ-ϕ bins, the overall χ^2_{total} is calculated using Eqn. 5.8.

$$\chi^2_{total} = \sum_{i=1}^{i=10} \sum_{j=1}^{j=12} \frac{(I^{data}_{i,j} - I^{MC}_{i,j})^2}{\sigma^2_{i,j}}, \tag{5.8}$$

where index i and j represents the θ and ϕ bins respectively. From the χ^2 value in the table, we see that HONDA and CORSIKA with FLUKA low energy hadronic model has better agreement with the data in comparison with other input models of CORSIKA, while there is not much variation with different high energy hadronic models. The events generated using GHEISHA as a low energy interaction model does not reproduce the data. The values of χ^2_{total} (for 120 bins) for different model are 194 (SG), 236 (HG), 240 (VG), 214 (EG), 208 (QG), 121 (SF), 161 (SU) and 105 (HONDA). From the overall comparison, the HONDA has better match with data in comparison with any of the CORSIKA models.

From the observed shape of the azimuthal spectrum, the east-west asymmetry of the cosmic ray increases with increase in zenith angle. The reason for the specific behaviour is the difference in the cut off rigidity for the primaries entering from west and east in higher zenith angle. From the predictions, it is observed that the east-

cosθ	χ^2_{SG}	χ^2_{HG}	χ^2_{VG}	χ^2_{EG}	χ^2_{QG}	χ^2_{SF}	χ^2_{SU}	χ^2_{HONDA}
1 - 0.95	9.14	5	4.54	3	2.36	1.72	5.2	1.78
0.95 - 0.9	4.67	9.91	6.8	9.12	10.1	4.91	4.69	6.96
0.9 - 0.85	14.3	33	15.2	19.1	23.5	5.75	6.62	19.9
0.85 - 0.8	17.3	16.5	14.4	27.6	24.7	10.8	29.3	17.6
0.8 - 0.75	21.6	34.8	31.1	22.2	22.2	19.4	26.1	11.5
0.75 - 0.7	22.2	31.7	36.9	29.6	27.7	13.5	22.6	13.5
0.7 - 0.65	36.8	28.6	46.7	34	28.8	22.4	21.1	6.91
0.65 - 0.6	39.4	38.1	48.5	39.8	38.6	25	26.4	13.8
0.6 - 0.55	19	23.5	22.5	19.9	21.6	13.8	12.1	7.4
0.55 - 0.5	9.5	14.6	13	9.34	8.07	3.61	6.55	5.17

Table 5.1: The comparison of $\chi^2_{DATA-MC}$ (for 12 ϕ bins) for data with different MC predictions in different $\cos\theta$ bins.

west asymmetry of the secondary cosmic rays is not affected by changing the high energy interaction models. But the low energy interaction models predominantly affect the east-west asymmetry. The measured east-west asymmetry at different zenith angle is having a better match with CORSIKA using FLUKA and urQMD as a low energy physics models. GHEISHA is showing a larger deviation from the observed east-west asymmetry. The phase (ϕ_0) of the distribution from CORSIKA with all models are comparable with data. As discussed earlier, the east-west asymmetry depends on geomagnetic latitude. The present experiment is located near the equator, it is expected to have larger asymmetry than other location on the earth. For example, the primaries with zenith angle of 60° entering from the west (east) will experience the cut off of 12 GeV (38 GeV). This larger difference in the cut off leads to huge asymmetry in the observed primary cosmic rays.

5.5 Measurement of exponent (n) and (I_0)

The previous section showed the detailed polar and azimuthal (θ, ϕ) dependence of the cosmic muon flux at the experimental site. For completeness, we include here the older results on the dependence on the polar angle alone, along with the extraction of the vertical muon intensity. The data recorded from phase-1 of

the experiment was used to estimate the shape of cosmic muon zenith angular distribution (exponent n) and integral intensity of vertical muons (I_0). These parameters depends on the location of the experiment as well as the minimum momentum the detector can measure (E_{min}). Due to the trigger criteria (namely, layer 1, 2, 9 and 10), the solid angle coverage of the phase-1 is smaller than the phase-2 (where trigger layers are 4, 5, 6 and 7). Also the middle 5 layers are having readout electronics for 32 strips in X- and Y-plane.

The vertical muon flux is the most important quantity at low energy, which depends on the geomagnetic latitude, longitude, altitude and momentum cut off. The zenith angular distribution of the cosmic ray muons has been extensively studied by many experimental groups. The zenith angular flux of muons for a wide ranges of angle was studied by Crookes and Rastin (1972) [92]. There are many other experiments that have measured the differential momentum spectrum, zenith angle dependency and integral muon flux at different locations on the earth [59, 93–99]. The experimental zenith angle spectrum of muons has the following dependence:

$$I(\theta, E_{min}) = I_0 \cos^n(\theta) \ , \tag{5.9}$$

where n is an exponent which is a function of the momentum and I_0 is the vertical integral flux of muons. The present section discusses an results of the measured zenith angular spectrum of muons and the vertical muon flux near the equator. The details about experimental setup, data analysis, simulation and physics results along with systematic studies are explained in Ref. [100].

5.5.1 Calculation of Exponent (n)

The value of the exponent (n) is estimated from the experimentally observed θ distribution ($N_{Obs}^{\theta_i}$) and the acceptance of the muons in the θ_i using MC. A χ^2 minimisation procedure used to get the best fit value of the exponent (n) is defined

as,

$$\chi^2 = \Sigma_{\theta_i} \frac{(N_{Obs}^{\theta_i} - P_0 \sin\theta_i \cos^n \theta_i w(\theta_i))^2}{N_{Obs}^{\theta_i} + (P_0 \sin\theta_i \cos^2 \theta_i \sigma_{w_i})^2} \tag{5.10}$$

where, $w(\theta_i)$, σ_{w_i}, P_0 and n are $\frac{N_{reconstructed}}{N_{generated}}$ in each θ-bin, the error on $w(\theta_i)$, normalization constant and exponent respectively.

The best fit value of the exponent for the events with a selection criteria of $\chi^2/\text{ndf} < 8$ and number of layer ≥ 7 is found to be,

$$n = 2.00 \pm 0.04\,(stat)\ . \tag{5.11}$$

5.5.2 Calculation of Integrated Vertical Flux

The integral intensity of the vertical muons (I_0) can be estimated from the observed θ distribution which can be given as,

$$I_0 = \frac{I_{data}}{\epsilon_{triggered} \times \epsilon_{selec} \times \epsilon_{daq} \times T_{tot} \times \omega}\ , \tag{5.12}$$

where, I_{data} is the integral of the observed θ distribution, $\epsilon_{triggered}$ is the trigger efficiency, ϵ_{selec} ($=N_{reconstructed}/N_{triggered}$) is the event selection efficiency in data. The cut-flow table listing the ϵ_{selec} for different selection criteria is given in Tab. 5.2. The estimated ϵ_{selec} for different χ^2/ndf does not vary much but there is decline in ϵ_{selec} as cut on number of layers increases. This decline is happing due to the middle five layers, where only 32 strips are populated with electronics.

Sel. Crit. (both X- and Y-plane)	$\chi^2/\text{ndf} < 7$	$\chi^2/\text{ndf} < 8$	$\chi^2/\text{ndf} < 9$
$N \geq 4$	62.4 %	62.8 %	63.1 %
$N \geq 5$	59.5 %	59.8 %	60.1 %
$N \geq 6$	50.1 %	50.4 %	50.6 %
$N \geq 7$	32.0 %	32.2 %	32.3 %
$N \geq 8$	15.5 %	15.6 %	15.7 %
$N \geq 9$	8.9 %	9.0 %	9.0 %

Table 5.2: The estimated selection efficiency for different selection criteria.

The parameter ϵ_{daq} is the efficiency accounting for dead time in the data acquisition system, T_{tot} is the total time taken to record the data (in seconds). ϵ_{daq} is defined as $(1 - Rate_{\mu} \times T_{dead})$, where $Rate_{\mu}$ (which is ~ 60 Hz) is the average trigger rate and T_{dead} (4 ms/event) dead time of DAQ after every event. The parameter ω is the accepted solid angle times the surface area, which is further defined as,

$$\omega(\theta) = \frac{AN}{N'} \cos^2\theta \sin\theta d\theta \times 2\,\pi \ , \tag{5.13}$$

where, A is the surface area of the RPC on top triggered layer, N is the number of events accepted when the generated position on the top and bottom trigger layer are inside the detector, N' is the Number of events generated on top trigger layer. The integral intensity of the vertical muons (I_0) with the selection criteria of $\chi^2/\mathrm{ndf} < 8$ and number of layer ≥ 7 is found to be,

$I_0 = (7.0069 \pm 0.0018(\mathrm{stat})) \times 10^{-3}$ cm^{-2} s^{-1} sr^{-1}. For more details Ref. [100].

5.5.3 Comparison of results with other experiments

Authors	Geomag. Lat. (°N)	Geomag. P_c(GV)	Altitude (m)	Muon. Mom (GeV/c)	Integral flux ($\times 10^{-3}$ cm^{-2} s^{-1} sr^{-1})
Crookes and Rastin [92]	53	2.2	40	$\geq$0.35	9.13 $\pm$ 0.12
Greisen [93, 94]	54	1.5	259	$\geq$ 0.33	8.2 $\pm$ 0.1
Fukui et al. [99]	24	12.6	S.L	$\geq$ 0.34	7.35 $\pm$ 0.2
Karmakar et al [98]	16	15.0	122	$\geq$0.353	8.99 $\pm$ 0.05
Sinha and Basu [101]	12	16.5	30	$\geq$ 0.27	7.3 $\pm$ 0.2
S.Pal [102]	10.61	16	S.L	$\geq$ 0.280	6.217 $\pm$ 0.005
Allkofer et al. [96]	9	14.1	S.L	$\geq$ 0.32	7.25 $\pm$ 0.1
Present data	1.44	17.6	160	$\geq$ 0.11	7.007 $\pm$ 0.002(stat) $\pm$ 0.526(syst)

Table 5.3: Comparison of vertical muon flux with other experiments.

The measurement of the angular distribution and integrated vertical flux of the cosmic ray muons have been extensively studied at different locations on the Earth by many experiments [92, 93, 96, 98, 99, 101, 102]. The present measurement

Authors	Geomag. Lat. (°N)	Geomag. P_c(GV)	Altitude (m)	Muon. Mom (GeV/c)	n value
Crookes and Rastin [92]	53	2.2	40	$\geq$0.35	2.16 ± 0.01
Greisen [93, 94]	54	1.5	259	$\geq$ 0.33	2.1
Judge and Nash [95]	53	–	S.L	$\geq$ 0.7	1.96 ± 0.22
Karmakar et al [98]	16	15.0	122	$\geq$0.353	2.2
S.Pal [102]	10.61	16	S.L	$\geq$ 0.280	2.15 ± 0.01
Present data	1.44	17.6	160	$\geq$ 0.11	2.00 ± 0.04(stat) ± 0.16(syst)

Table 5.4: Comparison of exponent (n) with other experiments.

adds one more data point in the flux table at a unique location on the earth. The present experiment is located near the geomagnetic equator. The location is significant because of the high vertical rigidity for the primary entering in the earth's magnetosphere. The flux of the muons varies with the different location on the earth depending on the geomagnetic latitude, longitude and the altitude. The measurement from [93, 96, 99, 101] shows that the muon flux decreases with increasing geomagnetic latitude as well as a decrease in the vertical rigidity cut off. The vertical rigidity cut off is more at the places close to the geomagnetic equator and less in the higher geomagnetic latitude.

The present result agrees with the above-observed phenomena on the dependency of muon flux in different geomagnetic latitude and rigidity cut off. The estimated vertical flux is lower than in comparison with [93, 96, 99, 101] because of the high vertical rigidity at the present site. The estimated exponent (n) from the present experiment is comparable with all other experiments. The comparison of the I_0 and n are given in Tables 5.3 and 5.4. Integral intensity of vertical muons extracted from HONDA prediction is $6.77 \times 10^{-3}\, cm^{-2}\, sr^{-1}\, s^{-1}$. The I_0 value from HONDA is comparable with observed result.

Largest possible uncertainties on the efficiencies, material description and input momentum considered for the systematic studies, which results in large systematic error in n and I_0. But in reality, these errors can be reduced a lot with better known

detector efficiencies, material budget and input spectrum to GEANT4 simulation.

Chapter 6

Summary of the thesis

The scope of the present thesis has five major chapters. The first chapter contains a brief introduction to neutrino physics, neutrino oscillations, measurement of cosmic ray fluxes, and its importance for the proposed India-based Neutrino Observatory (INO), which forms the motivation for this thesis. The second chapter describes the two different experimental details and the component parts of the ICAL prototype stack with 12 layers of RPC detectors that was used for the data collection. The third chapter gives details of the data collection including location and dates. The fourth chapter presents an analysis of this data and comparison with Monte Carlo simulations. The fifth chapter, which contains the results, mainly focusses on the determination of the azimuth angular spectrum of the cosmic flux, especially the east-west asymmetry of the cosmic muons, and a comparison with available theoretical estimates for the same. It also includes a summary of earlier results on the zenith angle spectrum of cosmic muons and their integral vertical intensity.

The various sources of neutrinos produce neutrinos at different energies starting from 10^6 eV to 10^{20} eV. The major sources neutrinos like the Sun and cosmic rays, nuclear reactors and geoneutrinos from th core are explained in brief. The general formalism on neutrino oscillation in vacuum and also the extension of the formalism to the oscillation in matter are also discussed. In addition, a short note on cosmic

muons as well as the design and properties of the ICAL experiment to ravel the mass ordering through earth matter effect is given. The final part of the chapter is completed with a discussion on the motivation and the scope of the present thesis.

The second chapter discussed the detector details. The stand alone RPC stack was constructed using 12 layers of $\sim 2m \times 2m$ RPC detectors. A brief description of the construction and operation of the RPCs and associated electronics is provided here.

Chapter 3 provides details on the data that was used for the analysis in this thesis. Chapter 4 presents details on the data analysis. The detector parameters such as the count rate of the RPCs and the variation in the behaviour of the RPCs in different ambient conditions were well studied. The detailed study of the RPCs like, pixel-wise efficiency, position resolution, time resolution and other detector related parameters are studied in detail and discussed in this chapter.

The muon data was collected using the trigger generated by four fixed layers. The collected data contains (i) strip hit pattern and (ii) muon arrival time in each layer. The strip hit data from the both plane were fitted using a straight line and the incident angle of the muon with respect to the Z-axis was calculated. A Monte-Carlo simulation was found to agree well with the measured efficiencies.

Chapter 5 contains the main results of the thesis. The Monte-Carlo code was used to generate cosmic ray fluxes from different theoretical predictions including CORSIKA [90] and Honda fluxes[1]. Both the high and low energy interaction models were varied and the azimuthal dependence of the muon fluxes so obtained were compared to the measured data. It was found that the Honda predictions and the CORSIKA estimates with the FLUKA low energy hadronic model best fitted the data, which were essentially insensitive to the high energy models. In particular, events generated using GEISHA as a low energy interaction model did not reproduce the data.

[1]Private Communication

The uncertainty in the estimation of the neutrinos on the surface is driven by the fluctuation in the pion productions during the primary interaction with atmosphere. In order to tune the interaction model in the simulation, the measurement of the muon flux at different locations on the earth is essential. The muon flux at a given location on the earth depends on the latitude, longitude, altitude and vertical rigidity cut off. The present experiment is located very near to the geomagnetic equator. The vertical rigidity at the present location is around 17.6 GeV. The observed results are compared with a muon flux measured at the different places on the earth. The comparison is given in this chapter suggests that, the muon flux is increasing with increase in the latitude and decreasing in the vertical rigidity cut off. The observed result from the present work satisfies the above mentioned phenomenon. As a very high rigidity cut off, the observed muon flux at the experimental site is smaller than other measurements.

Recently, a mini-ICAL prototype has been constructed at the same site, where the RPCs are interspersed in layers of magnetised iron. The primary aim of the ICAL-prototype is to study the long-term performance of the RPC detectors and final electronics for the ICAL experiment manufactured in the Indian industry. The prototype will help to optimise the design parameters for the RPC detectors and electronics and data acquisition system. No physics results were obtained by me with this mini-ICAL prototype set-up. However, I was involved in the trouble shooting during installation of the mini-ICAL detector; some details of my contribution are presented in Appendix A.

The key result of the thesis is that a change in the low energy physics models changes the shape of the azimuthal cosmic muon spectrum predominantly. From this work, it is concluded that the FLUKA and urQMD as a input low energy interaction model in CORSIKA reproduces the observed data. The shape of the azimuthal spectrum from HONDA predictions has a better match with data in comparison with CORSIKA models. The prototype detector stack used for this

analysis was built without a magnet. It is clear that improved results will be obtained in future due to better control on the momentum dependence of the fluxes when the mini-ICAL with associated magnet is used to study the angular dependence of the cosmic ray muons.

Appendix-A

Trouble shooting the mini-ICAL detector

The few major problems faced in the detector stack after commissioning are discussed in the present section.

MFC failure

Mass Flow Controllers (MFCs) are the heart of the gas system, which will allow the individual gas with proper fraction to the mixing cylinder. During the operation, it was found that the gain of the detector is decreased, which can be observed from the noise rate, dark current, occupancy, multiplicity and the efficiency of the RPCs. The efficiency map for RPCs shown in Fig. 6.1 suggests that the gain of the RPCs is much less than expected. It was not clear whether the problem is due to the electronics, or gas composition. The detector along with front-end boards are located more than a meter inside the iron plate, which cannot be easily accessed without taking the RPC tray outside. The variation in the detector parameters are quite unusual and unlikely to be due to any ambient issues. The only possibility is that there is a change in the gas composition.

The flow rate of each gas is measured using the water displacement method. It was found that the flow of SF_6 (around 1 %) is more than the set value (0.3 %). The particular gas composition was chosen to avoid the streamer evolution. The purpose of the small fraction of SF_6 is to quench the electrons at the same time

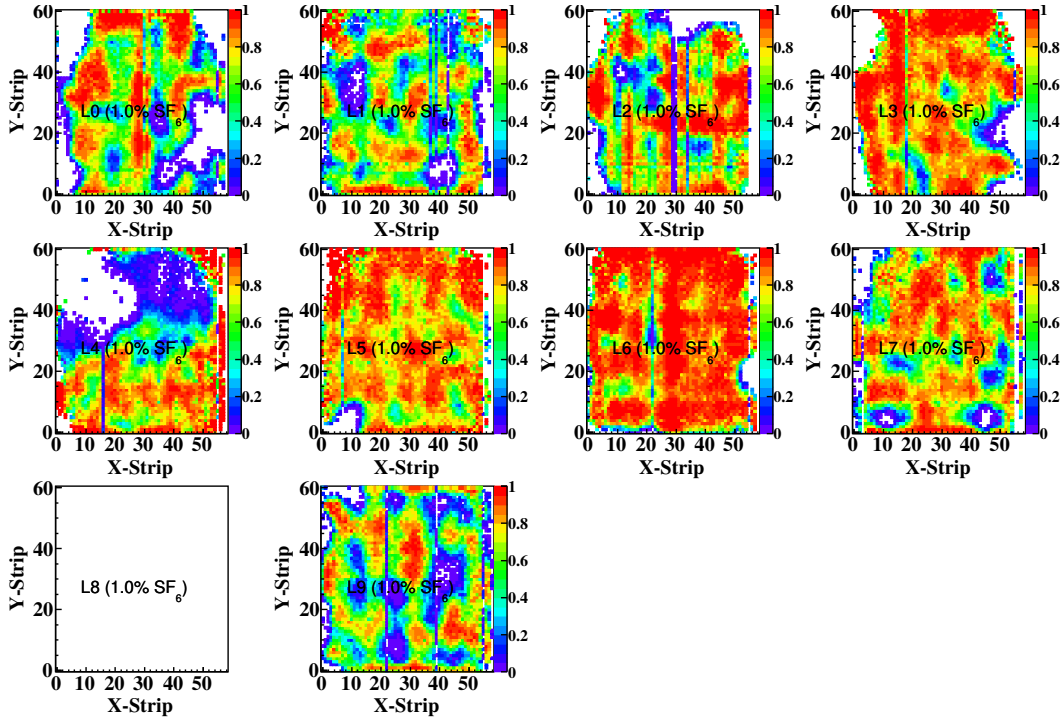

Figure 6.1: The efficiency map for all the RPCs in the mini-ICAL before replacing the MFC. Efficiency histograms for Layer-8 shows empty because it was not participating in the data taking.

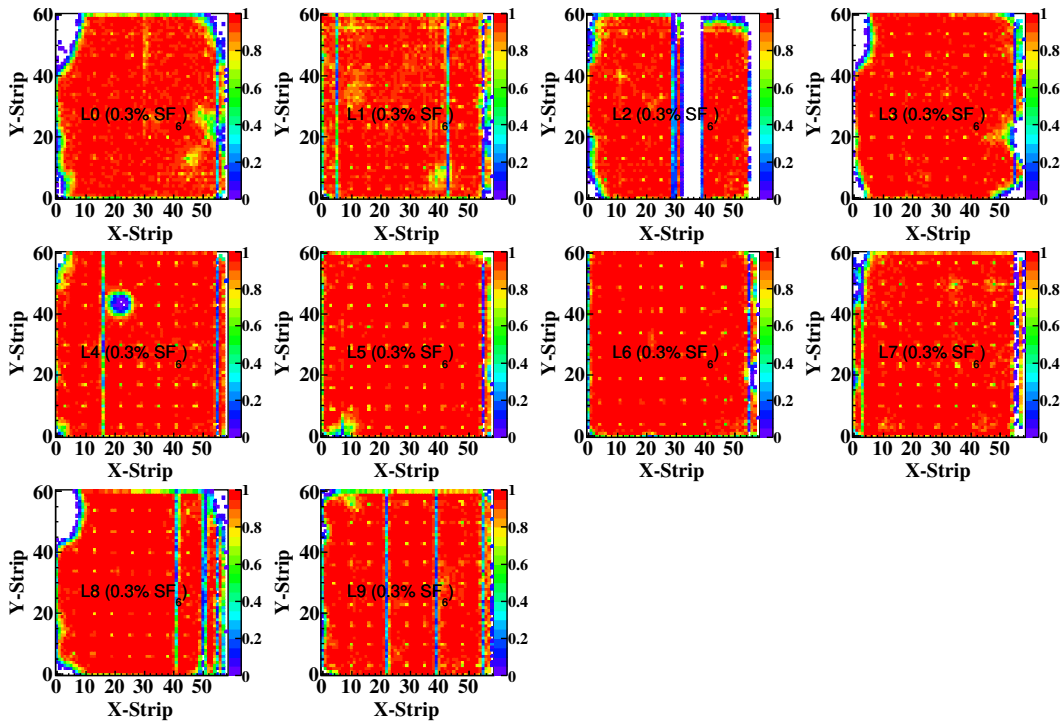

Figure 6.2: The efficiency map for all the RPCs in the mini-ICAL after replacing the MFC.

to allow the avalanche to grow to a reasonable size. The excess of SF_6 may cause the less growth of the avalanche, leading to a low gain. The voltage read out from the MFCs are tested by multimeter and it read maximum volts. This is a clear indication that the magnetic valve in the MFC which controls the gas flow is not working properly. The reason for the failure is unknown. The problematic MFC was replaced with a new MFC and the detector parameters became normal. The efficiency of the RPCs after replacing the MFC are shown in Fig. 6.2.

Shifting of the time spectrum

During the troubleshooting after commissioning, there is a problem in the data taking, where the data taking software is interrupted, when there is a sudden burst of EMI from the electrical switches. This problem was never observed in the previous stack discussed in Chapter 2. Finally, it was found that the problem is due to limitation in the array size of the TDC data.

Multi-hit HPTDC chips are used to record the time of arrival in each layer. In the NIOS processor the array size of four is defined. When the EMI occurs, all the strips give signal together, and the DAQ is not able to record beyond 4 hits in each channel, and this results in interrupt in the system.

While solving the above mentioned issue, each and every part of the detector setup was tested, including the analog front-end, digital front-end (RPCDAQ), signal router boards, trigger module. The data is analysed after solving the issue. It was observed that the time spectrum of all the layers are shifted by approximately 100 ns and very small fraction of the events is present in the time as expected. Initially, checks were carried out on the gas system, front-end boards, LVDS output of analog front-end board. The problem was not understood from the testing of the front-end hardware.

The second approach was to see if the effect was due to any change in the software. The shift in the main peak of time spectrum from the expected time

and presence of very small second peak in the expected time was a puzzle to understand. In the second phase of the solving process, the effect on the time spectrum by varying the pre-trigger width in the RPCDAQ board was observed. The pre-trigger width in the RPCDAQ was changed to multiple values such as 60 ns, 120 ns, 140 ns, 160 ns and 180 ns. The time spectrum for the different pre-trigger widths were compared and it was found that there is a change in the time difference between the first and second peak, the time gap is equivalent to the width of the pre-trigger signals (shown in Fig. 6.3), but position of second small peak remains in the same position.

After the software was tested in the front-end side, the back-end software was tested by keeping the trigger independently only in the X-plane or Y-plane. There was no change in the spectrum other than the improvement in the width of the time spectrum by fixing one plane trigger.

The third phase of the troubleshooting was to check the back-end hardware including the signal router boards and trigger logic boards. The motivation to check the trigger system is if there is a problem in the trigger generation. Eventually, it was found that the Global Trigger connector from the Global trigger board to the Calibration and Auxiliary Unit was inverted. The inversion in the connector causes a swap in the leading and trailing edge of the trigger signal. On the arrival of the inverted trigger signal to the RPCDAQ, the timing data was recorded due to trailing part of the trigger signal instead of leading edge. This leads to the shift in the main peak of the time spectrum. Hence the time difference between the first and second peak was varying with coincidence width.

Correlation between strips

The simultaneous signals from different strips are mostly due to the larger strip multiplicity due to larger signal due to muon passing through and the correlated electronics noise. Here the correlated electronics noise happens rarely. Other than

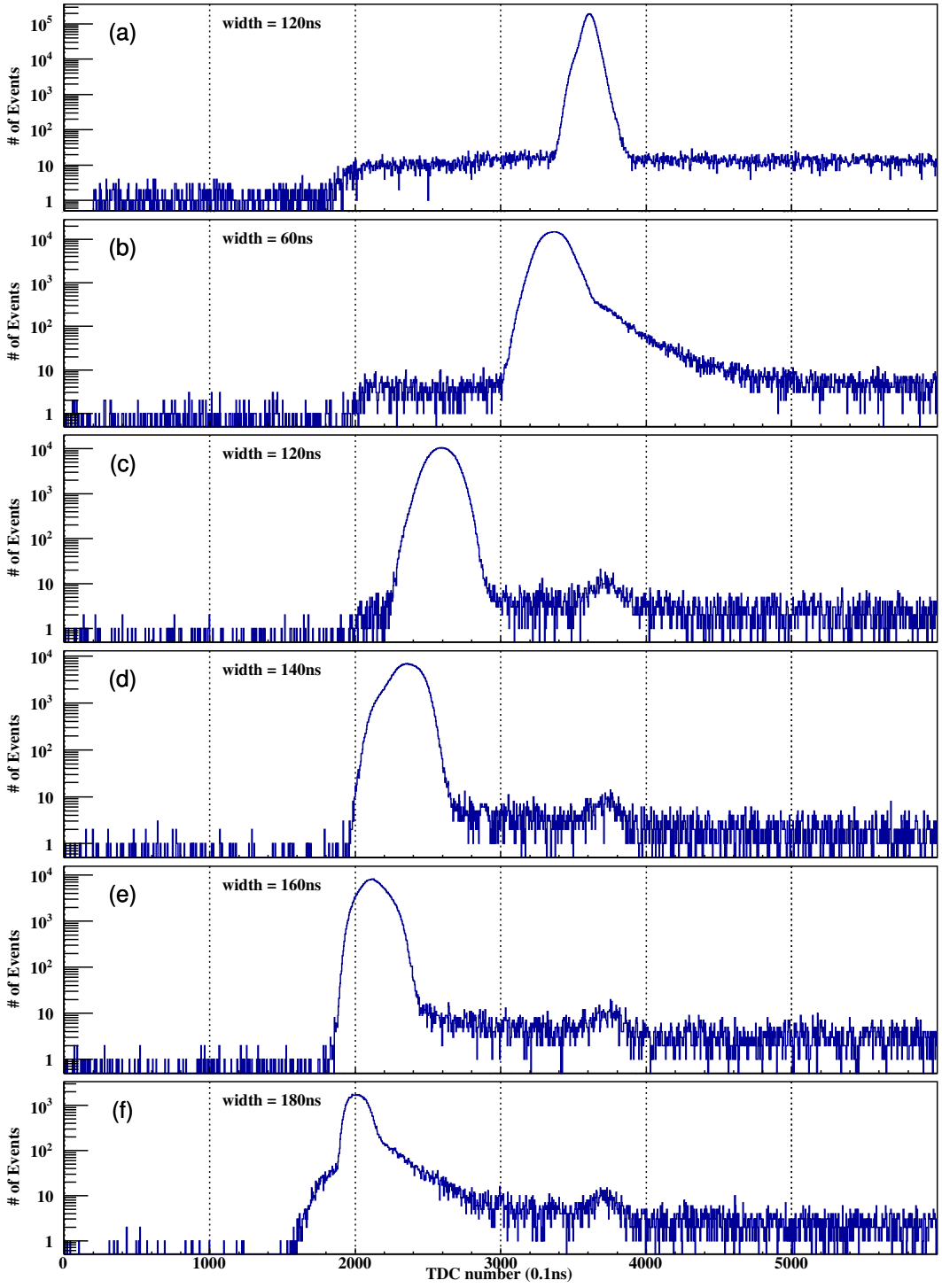

Figure 6.3: (a) The time spectrum when trigger cable connected properly. (b), (c), (d), (e) and (f) are time spectrum of layer-0 when trigger signal is inverted.

the above mentioned reasons, there are other possibilities like the physical connection between nearby strips due to the small piece of metal trapped in between the copper strips in pick-up panel. Fig. 6.5 shows the fraction of events when a strip

is correlated with other strips. The strip numbers 42 and 43 in layer 8 show the maximum fraction of events. When strip 42 has a signal, at the same time strip 43 also has a signal and other way about as well. Similarly, layer 6 also has the same issue between strip numbers 25 and 26. The strip correlation due to avalanche size was not the reason for the layer-8 problem. The connectivity between the two strips were tested by multimeter, which confirmed the short between the strips. These problems occurred while commissioning the stack. It would be difficult to remove the small piece of metal after the RPCs are in the stack without disassembling the RPCs.

The location of the short along the length of the strip was not known. To find the precise location of the short, the timing data was used. The raw time difference between strips 42 and 43 versus the position in the strip along the length is shown in Fig. 6.4 and clearly indicates the location of the short. The layer-8 shows the short which is almost in the middle of the detector while layer-6 has the short at the end of the detector.

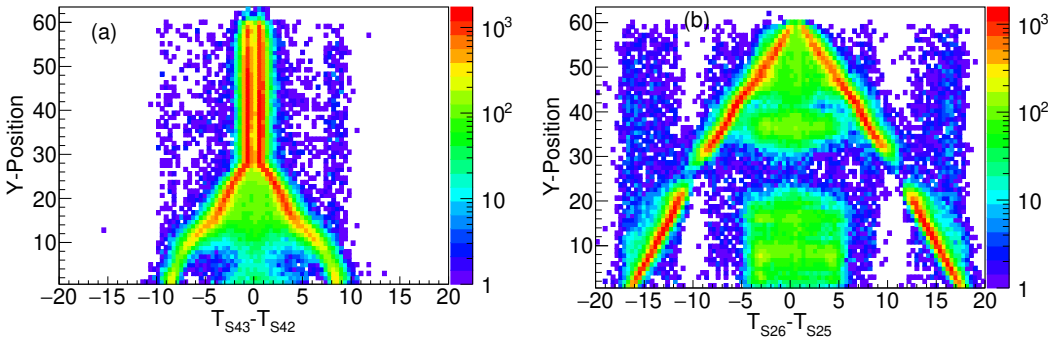

Figure 6.4: (a) The electronic short in between two strips in layer-8 in the middle of the strips, (b) The short between two strips at the end of the strips in layer-6.

There are other kind of correlation between the channels in the front-end boards. These problems are occurring due to the poor connection of ground wire in the pre-amplifier input side. The improper connection leads to the pickup noise in other strips. One such problem is present in the layer-7 in strip number 8 and 12. The strip number 12 gets a signal whenever a muon passes through strip number 8

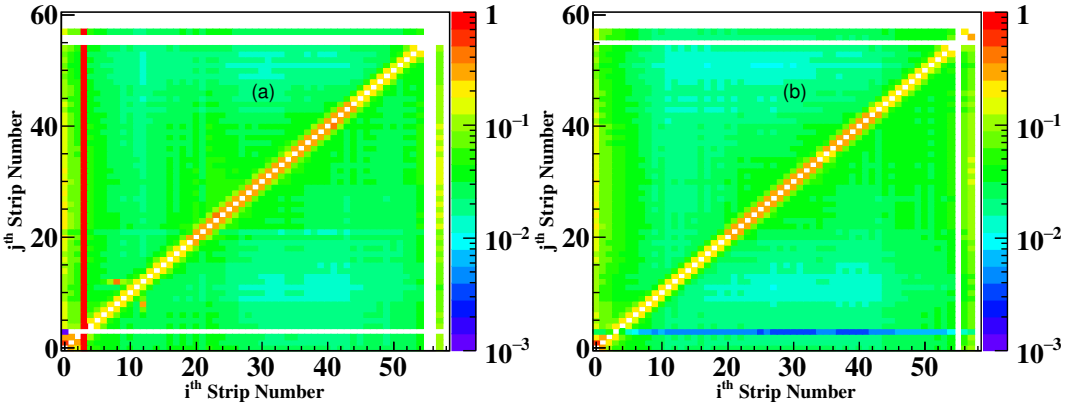

Figure 6.5: (a) The correlation among the strips 8 and 12 in layer-7 (X-plane), is due to the ground wire being broken in the NINO front-end. (b) The correlation in the strips after solving the problem.

(shown in Fig. 6.5(a)). It was found that the ground wire in the NINO input of strip number 12 was broken. The strips with broken ground wire are prone to pick up noise from other strips. The problem disappears after proper soldering the ground wire (as shown in Fig. 6.5(b)).

Bibliography

[1] Pauli W. Letter to the participants of workshop at tübingen, germany. 1930.

[2] W. pauli, 2000.

[3] E. Fermi. Tentativo di una teoria dei raggi β (in italian). *La Ricerca Scientifica*, 2:12, 1933.

[4] E. Fermi. Versuch einer theorie der beta-strahlen (in german). *Z. Phys.*, 88:161, 1934.

[5] E. Fermi. Tentativo di una teoria dei raggi β (in italian). *Nuovo Cimento*, 11:1–19, 1934.

[6] C. L. Cowan, F. Reines, F. B. Harrison, H. W. Kruse, and A. D. McGuire. Detection of the free neutrino: a confirmation. *Science*, 124(3212):103–104, 1956.

[7] F. Reines and C. L. Cowan. The neutrino. *Nature*, 178:446–449, 1956.

[8] G. Danby, J-M. Gaillard, K. Goulianos, et al. Observation of high-energy neutrino reactions and the existence of two kinds of neutrinos. *Phys. Rev. Lett.*, 9:36–44, Jul 1962.

[9] K. Kodama, N. Ushida, C. Andreopoulos, et al. Observation of tau neutrino interactions. *Physics Letters B*, 504(3):218 – 224, 2001.

[10] Abdus Salam. Weak and Electromagnetic Interactions. *Conf. Proc.*, C680519:367–377, 1968.

[11] Steven Weinberg. A model of leptons. *Phys. Rev. Lett.*, 19:1264–1266, Nov 1967.

[12] Sheldon L. Glashow. Partial-symmetries of weak interactions. *Nuclear Physics*, 22(4):579 – 588, 1961.

[13] F.J. Hasert, H. Faissner, W. Krenz, et al. Search for elastic muon-neutrino electron scattering. *Physics Letters B*, 46(1):121 – 124, 1973.

[14] F.J. Hasert, S. Kabe, W. Krenz, et al. Observation of neutrino-like interactions without muon or electron in the gargamelle neutrino experiment. *Nuclear Physics B*, 73(1):1 – 22, 1974.

[15] F.J. Hasert, S. Kabe, W. Krenz, et al. Observation of neutrino-like interactions without muon or electron in the gargamelle neutrino experiment. *Physics Letters B*, 46(1):138 – 140, 1973.

[16] A. Benvenuti, D. C. Cheng, D. Cline, et al. Observation of muonless neutrino-induced inelastic interactions. *Phys. Rev. Lett.*, 32:800–803, Apr 1974.

[17] S. Chatrchyan, V. Khachatryan, A.M. Sirunyan, et al. Observation of a new boson at a mass of 125 gev with the cms experiment at the lhc. *Physics Letters B*, 716(1):30 – 61, 2012.

[18] G. Aad, T. Abajyan, B. Abbott, et al. Observation of a new particle in the search for the standard model higgs boson with the atlas detector at the lhc. *Physics Letters B*, 716(1):1 – 29, 2012.

[19] D. DeCamp, B. Deschizeaux, J.-P. Lees, et al. Determination of the number of light neutrino species. *Physics Letters B*, 231(4):519 – 529, 1989.

[20] M.Z. Akrawy, G. Alexander, J. Allison, et al. Measurement of the z0 mass and width with the opal detector at lep. *Physics Letters B*, 231(4):530 – 538, 1989.

[21] P. Aarnio, P. Abreu, W. Adam, et al. Measurement of the mass and width of the z0-particle from multihadronic final states produced in $e^+ e^-$ annihilations. *Physics Letters B*, 231(4):539 – 547, 1989.

[22] B. Adeva, O. Adriani, M. Aguilar-Benitez, et al. A determination of the properties of the neutral intermediate vector boson z0. *Physics Letters B*,

231(4):509 – 518, 1989.

[23] Kai Zuber. *Neutrino Physics*. CRC Press.

[24] Christian Spiering. Towards High-Energy Neutrino Astronomy. A Historical Review. *Eur. Phys. J. H*, 37:515–565, 2012.

[25] John N. Bahcall. Solar neutrinos. i. theoretical. *Phys. Rev. Lett.*, 12:300–302, Mar 1964.

[26] Raymond Davis. Solar neutrinos. ii. experimental. *Phys. Rev. Lett.*, 12:303–305, Mar 1964.

[27] Y. Fukuda et al. The Super-Kamiokande detector. *Nucl. Instrum. Meth.*, A501:418–462, 2003.

[28] J. Hosaka, K. Ishihara, J. Kameda, et al. Solar neutrino measurements in super-kamiokande-i. *Phys. Rev. D*, 73:112001, Jun 2006.

[29] The Super-Kamiokande Collaboration, :, and B. S. Yang. Solar neutrino measurement at sk-iii, 2009.

[30] B. Aharmim, S. N. Ahmed, A. E. Anthony, et al. Combined analysis of all three phases of solar neutrino data from the sudbury neutrino observatory. *Phys. Rev. C*, 88:025501, Aug 2013.

[31] *Proton-Proton chain reaction (Wikipedia).*

[32] *CNO cycle (Wikipedia).*

[33] Y. Fukuda, T. Hayakawa, E. Ichihara, et al. Evidence for oscillation of atmospheric neutrinos. *Phys. Rev. Lett.*, 81:1562–1567, Aug 1998.

[34] A. Gando et al. Reactor On-Off Antineutrino Measurement with KamLAND. *Phys. Rev.*, D88(3):033001, 2013.

[35] M. Agostini et al. Spectroscopy of geoneutrinos from 2056 days of Borexino data. *Phys. Rev.*, D92(3):031101, 2015.

[36] S. Abe, T. Ebihara, S. Enomoto, et al. Precision measurement of neutrino oscillation parameters with kamland. *Phys. Rev. Lett.*, 100:221803, Jun 2008.

[37] T. Araki, K. Eguchi, S. Enomoto, et al. Measurement of neutrino oscillation

with kamland: Evidence of spectral distortion. *Phys. Rev. Lett.*, 94:081801, Mar 2005.

[38] M Apollonio, A Baldini, C Bemporad, et al. Initial results from the chooz long baseline reactor neutrino oscillation experiment. *Physics Letters B*, 420(3):397 – 404, 1998.

[39] M. Apollonio, A. Baldini, C. Bemporad, et al. Limits on neutrino oscillations from the chooz experiment. *Physics Letters B*, 466(2):415 – 430, 1999.

[40] Jun Cao and Kam-Biu Luk. An overview of the daya bay reactor neutrino experiment. *Nuclear Physics B*, 908:62 – 73, 2016. Neutrino Oscillations: Celebrating the Nobel Prize in Physics 2015.

[41] J. K. Ahn, S. Chebotaryov, J. H. Choi, et al. Observation of reactor electron antineutrinos disappearance in the reno experiment. *Phys. Rev. Lett.*, 108:191802, May 2012.

[42] K. Abe, R. Akutsu, A. Ali, et al. Search for *cp* violation in neutrino and antineutrino oscillations by the t2k experiment with 2.2×10^{21} protons on target. *Phys. Rev. Lett.*, 121:171802, Oct 2018.

[43] M. A. Acero, P. Adamson, L. Aliaga, et al. First measurement of neutrino oscillation parameters using neutrinos and antineutrinos by nova. *Phys. Rev. Lett.*, 123:151803, Oct 2019.

[44] K. Hirata, T. Kajita, M. Koshiba, et al. Observation of a neutrino burst from the supernova sn1987a. *Phys. Rev. Lett.*, 58:1490–1493, Apr 1987.

[45] R. M. Bionta, G. Blewitt, C. B. Bratton, et al. Observation of a neutrino burst in coincidence with supernova 1987a in the large magellanic cloud. *Phys. Rev. Lett.*, 58:1494–1496, Apr 1987.

[46] M. G. Aartsen, R. Abbasi, Y. Abdou, et al. First observation of pev-energy neutrinos with icecube. *Phys. Rev. Lett.*, 111:021103, Jul 2013.

[47] IceCube Collaboration. Evidence for high-energy extraterrestrial neutrinos at the icecube detector. *Science*, 342(6161), 2013.

[48] M. G. Aartsen, M. Ackermann, J. Adams, et al. Observation of high-energy astrophysical neutrinos in three years of icecube data. *Phys. Rev. Lett.*, 113:101101, Sep 2014.

[49] A. de gouvea, on determining the neutrino mass hierarchy, fnal theory seminar(2006).

[50] Ivan Esteban, M. C. Gonzalez-Garcia, Michele Maltoni, Thomas Schwetz, and Albert Zhou. The fate of hints: updated global analysis ofthree- avor neutrino oscillations. *Journal of High Energy Physics*, 178(2020), Sept 2020.

[51] *NuFIT webpage.*

[52] L. Wolfenstein. Neutrino oscillations in matter. *Phys. Rev. D*, 17:2369–2374, May 1978.

[53] S. P. Mikheyev and A. Yu. Smirnov. Resonance Amplification of Oscillations in Matter and Spectroscopy of Solar Neutrinos. *Sov. J. Nucl. Phys.*, 42:913–917, 1985. [,305(1986)].

[54] A. Kumar, A. M. Vinod Kumar, Abhik Jash, et al. Invited review: Physics potential of the ical detector at the india-based neutrino observatory (ino). *Pramana*, 88(5):79, Apr 2017.

[55] Lakshmi S. Mohan and D. Indumathi. Pinning down neutrino oscillation parameters in the 2–3 sector with a magnetised atmospheric neutrino detector: a new study. *Eur. Phys. J. C*, 77(1):54, 2017.

[56] DUNE Collaboration, B. Abi, R. Acciarri, et al. The dune far detector interim design report volume 1: Physics, technology and strategies, 2018.

[57] Francisco Barradas-Solas. Giving new life to old equipment. *Physics Education*, 42(1):9–11, dec 2006.

[58] P. K. F. Grieder. *Cosmic rays at earth: Researcher's reference, manual and data book.* Elsevier, Amsterdam, 2001.

[59] J. Kremer et al. Measurements of ground-level muons at two geomagnetic locations. *Phys. Rev. Lett.*, 83:4241–4244, 1999.

[60] M. Aguilar et al. Precision Measurement of the Proton Flux in Primary Cosmic Rays from Rigidity 1 GV to 1.8 TV with the Alpha Magnetic Spectrometer on the International Space Station. *Phys. Rev. Lett.*, 114:171103, 2015.

[61] M. Aguilar et al. Precision Measurement of the Helium Flux in Primary Cosmic Rays of Rigidities 1.9 GV to 3 TV with the Alpha Magnetic Spectrometer on the International Space Station. *Phys. Rev. Lett.*, 115(21):211101, 2015.

[62] O. Adriani et al. PAMELA Measurements of Cosmic-ray Proton and Helium Spectra. *Science*, 332:69–72, 2011.

[63] K. Abe et al. Measurements of cosmic-ray proton and helium spectra from the BESS-Polar long-duration balloon flights over Antarctica. *Astrophys. J.*, 822(2):65, 2016.

[64] Bing-Bing Wang, Xiao-Jun Bi, Kung Fang, Su-Jie Lin, and Peng-Fei Yin. Time dependent solar modulation of cosmic rays from solar minimum to solar maximum. *Phys. Rev. D*, 100(6):063006, 2019.

[65] R. A. Alpher. Theoretical geomagnetic effects in cosmic radiation. *Journal of Geophysical Research (1896-1977)*, 55(4):437–471, 1950.

[66] https://ntrs.nasa.gov/citations/19770009539.

[67] M. Honda, M. Sajjad Athar, T. Kajita, K. Kasahara, and S. Midorikawa. Reduction of the uncertainty in the atmospheric neutrino flux prediction below 1 gev using accurately measured atmospheric muon flux. *Phys. Rev. D*, 100:123022, Dec 2019.

[68] C.V. Achar, M.G.K. Menon, V.S. Narasimham, et al. Observation of a non-elastic cosmic ray neutrino interaction. *Physics Letters*, 19(1):78 – 80, 1965.

[69] C.V. Achar, M.G.K. Menon, V.S. Narasimham, et al. Detection of muons produced by cosmic ray neutrinos deep underground. *Physics Letters*, 18(2):196 – 199, 1965.

[70] K. Raveendrababu, P. K. Behera, and B. Satyanarayana. Effect of electrical

properties of glass electrodes on the performance of RPC detectors for the INO-ICAL experiment. *JINST*, 11(08):P08024, 2016.

[71] Morihiro Honda, T. Kajita, K. Kasahara, S. Midorikawa, and T. Sanuki. Calculation of atmospheric neutrino flux using the interaction model calibrated with atmospheric muon data. *Phys. Rev.*, D75:043006, 2007.

[72] Bheesette Satyanarayana. *Design and Characterisation Studies of Resistive Plate Chambers*. PhD thesis, Indian Institute of Technology Bombay, 2012.

[73] Apoorva Dipak Bhatt. *Measuement of Atmospheric Muons at IICHEP in Madurai, for better estimation of Neutrino Fluxes at INO Site in Theni*. PhD thesis, Homi Bhabha National Institute, 2019.

[74] Apache Software Foundation. Magnet, 2008.

[75] N. Panchal, G. Majumder, and V.M. Datar. Simulation of muon-induced neutral particle background for a shallow depth iron calorimeter detector. *JINST*, 14(02):P02032, feb 2019.

[76] R. Santonico and R. Cardarelli. Development of resistive plate counters. *Nuclear Instruments and Methods in Physics Research*, 187:377–380, 1981.

[77] M. Bhuyan, V.B. Chandratre, S. Dasgupta, et al. Vme-based data acquisition system for the india-based neutrino observatory prototype detector. *Nuclear Instruments and Methods in Physics Research Section A: Accelerators, Spectrometers, Detectors and Associated Equipment*, 661, Supplement 1:S73 – S76, 2012. X. Workshop on Resistive Plate Chambers and Related Detectors (RPC 2010).

[78] Sumanta Pal. *Development of the INO-ICAL detector and its physics potential*. PhD thesis, Homi Bhabha National Institute, 2014.

[79] F. Anghinolfi, P. Jarron, F. Krummenacher, E. Usenko, and M. C. S. Williams. NINO: An ultrafast low-power front-end amplifier discriminator for the time-of-flight detector in the ALICE experiment. *IEEE Trans. Nucl. Sci.*, 51:1974–1978, 2004.

[80] F. Anghinolfi, P. Jarron, A. N. Martemyanov, et al. NINO: An ultra-fast and low-power front-end amplifier/discriminator ASIC designed for the multigap resistive plate chamber. *Nucl. Instrum. Meth.*, A533:183–187, 2004.

[81] Puneet Kanwar Kaur, Pathaleswar, M. N. Saraf, B. Satyanarayana, and R. R. Shinde. Development of Fast, Low Power 8-Channel Amplifier-Discriminator Board for the RPCs. *Springer Proc. Phys.*, 203:571–574, 2018.

[82] V. B. Chandratre, Menka Sukhwani, Hari Prasad Kolla, et al. ANUSPARSH-II frontend ASIC for avalanche mode of RPC detector using regulated cascode trans-impedance amplifier. 60:928–929, 2015.

[83] M. N. Saraf, U. Gokhale, A. Lokapure, et al. Soft-Core Processor Based Data Acquisition Module for ICAL RPCs with Network Interface. *Springer Proc. Phys.*, 174:565–570, 2016.

[84] J Christiansen. HPTDC High Performance Time to Digital Converter. Technical report, CERN, Geneva, 2004. Version 2.2 for HPTDC version 1.3.

[85] Suryanarayan Mondal, V.M. Datar, Gobinda Majumder, et al. Study of Particle Multiplicity of Cosmic Ray Events using 2m×2m Resistive Plate Chamber Stack at IICHEP-Madurai. 8 2019.

[86] S. Achrekar, S. Aniruddhan, N. Ayyagiri, et al. Electronics, trigger and data acquisition systems for the ino ical experiment. In Zhen-An Liu, editor, *Proceedings of International Conference on Technology and Instrumentation in Particle Physics 2017*, pages 291–295, Singapore, 2018. Springer Singapore.

[87] World magnetic model-2020,https://www.ngdc.noaa.gov/geomag/wmm/image.shtml.

[88] Omniweb, https://omniweb.gsfc.nasa.gov/.

[89] Louis Lyons. *Statistics for Nuclear and Particle Physicists*. Cambridge University Press, 1986.

[90] D. Heck, J. Knapp, J. N. Capdevielle, G. Schatz, and T. Thouw. CORSIKA: A Monte Carlo code to simulate extensive air showers. 1998.

[91] S. Agostinelli et al. GEANT4: A Simulation toolkit. *Nucl. Instrum. Meth.*,

A506:250–303, 2003.

[92] J. N. Crookes and B. C. Rastin. An investigation of the absolute intensity of muons at sea-level. *Nucl. Phys.*, B39:493–508, 1972.

[93] Kenneth Greisen. The intensities of the hard and soft components of cosmic rays as functions of altitude and zenith angle. *Phys. Rev.*, 61:212–221, Mar 1942.

[94] Bruno Rossi. Interpretation of Cosmic-Ray Phenomena. *Rev. Mod. Phys.*, 20(3):537–583, 1948.

[95] R. J. R. Judge and W. F. Nash. Measurements on the muon flux at various zenith angles. *Il Nuovo Cimento (1955-1965)*, 35(4):999–1024, 1965.

[96] O. C. Allkofer, R. D. Andresen, and W. D. Dau. The muon spectra near the geomagnetic equator. *Canadian Journal of Physics*, 46(10):S301–S305, 1968.

[97] O. C. Allkofer, K. Carstensen, and D. W. Dau. The absolute cosmic ray muon spectrum at sea level. *Phys. Lett.*, 36B:425–427, 1971.

[98] N. L. Karmakar, A. Paul, and N. Chaudhuri. Measurements of absolute intensities of cosmic-ray muons in the vertical and greatly inclined directions at geomagnetic latitudes 16 degrees n. *Nuovo Cim.*, B17:173–186, 1973.

[99] Shuji Fukui, Takashi Kitamura, and Yojiro Murata. On the range spectrum of μ-mesons at sea-level at geomagnetic latitude 24°n. *Journal of the Physical Society of Japan*, 12(8):854–863, 1957.

[100] S. Pethuraj, V.M. Datar, G. Majumder, et al. Measurement of cosmic muon angular distribution and vertical integrated flux by 2 m $\times$ 2 m RPC stack at IICHEP-madurai. *Journal of Cosmology and Astroparticle Physics*, 2017(09):021–021, sep 2017.

[101] M.S. Sinha and N. Basu. Low energy spectrum of the sea level electrons and muons at 12°N. *Indian J. Phys.*, 33, 1959.

[102] S. Pal, B. S. Acharya, G. Majumder, et al. Measurement of integrated flux of cosmic ray muons at sea level using the INO-ICAL prototype detector.

JCAP, 1207:033, 2012.